EFFECTS OF SUBSTRATE ON 2D MATERIALS, GRAPHENE, MOS$_2$, WS$_2$, AND BLACK PHOSPHORUS, INVESTIGATED BY HIGH TEMPERATURE AND SPATIALLY RESOLVED RAMAN SCATTERING AND PHOTOLUMINESCENCE

by

Liqin Su

A dissertation submitted to the faculty of
The University of North Carolina at Charlotte
in partial fulfillment of the requirements
for the degree of Doctor of Philosophy in
Electrical Engineering

Charlotte

2015

Approved by:

_____
Dr. Yong Zhang

_____
Dr. Raphael Tsu

_____
Dr. Michael Fiddy

_____
Dr. Qiuming Wei

ABSTRACT

LIQIN SU. Effects of substrate on 2D materials, Graphene, MoS$_2$, WS$_2$, and Black phosphorus, investigated by high temperature and spatially resolved Raman scattering and photoluminescence. (Under the direction of DR. YONG ZHANG)

The exploration of a group of new 2D materials, such as graphene and transition metal dichalcogenides, has become the hottest research of interest in recent years. With the dependable techniques of producing 2D materials, particularly mechanical exfoliation and chemical vapor deposition, we are able to study all kinds of their unique properties in mechanical, electrical and optical fields. In this dissertation, we examine the vibrational and thermal properties of four 2D materials – graphene, MoS$_2$, WS$_2$ and black phosphorus – as well as their interaction with the supporting substrates, by using temperature-dependent Raman spectroscopy. Regarding the increasing interests of studying on the fabrication and applications of 2D materials, the role of 2D-material/substrate interaction has seldom been taken into consideration which would significantly affects the quality of the grown films and the performance of the devices. To the best of our knowledge, we are the first to systematically investigate on this issue.

At first, we performed temperature-dependent Raman spectroscopy on two graphene samples prepared by CVD and ME up to 400 °C, as well as graphite as a reference. The temperature dependence of both graphene samples shows very non-linear behavior for G and 2D bands, but with the CVD-grown graphene more nonlinear. Comparing to the Raman spectra collected before the measurements, the spectra after the measurements exhibit not only a shift of peak position but also a huge broadening of linewidth, especially for CVD-grown graphene. This study implies that the polymeric residues from either scotch tape or PMMA during transfer process are converted to amorphous carbon after annealed at high temperature, which may significantly change the optical and electrical properties of graphene.

With the same temperature-dependent Raman technique as graphene, we examine on monolayer MoS_2 and WS_2, and thin-film black phosphorus and demonstrate that the film morphology and the substrate play very important roles in modifying the properties of the materials. For the films transferred onto SiO_2/Si substrates, the E_{2g}^1 mode is only weakly affected by the substrate, whereas the A_{1g} mode is strongly perturbed, showing a highly nonlinear temperature dependence in Raman peak shift and linewidth. In contrast, for the films epitaxially grown on sapphire substrate, E_{2g}^1 is tuned more significantly by the substrate by showing a much smaller temperature coefficient than the bulk, while A_{1g} is less. A two-round temperature dependent Raman measurements on a transferred MoS_2 on SiO_2 sample confirm these findings. These experiments suggest that the film-substrate coupling depends sensitively on the preparation method, and in particular on the film morphology for the transferred film. Additionally, temperature-dependent PL spectroscopy of monolayer WS_2 shows a 0.2 eV activation energy for CVD-grown films on SiO_2/Si substrate.

Besides temperature dependent Raman spectroscopy, we also perform PL and Raman mappings on monolayer WS_2 triangles prepared by both chemical vapor deposition and transfer, and find both Raman and PL are very sensitive to strain and doping effects. The non-uniform strain distribution over one single triangle is determined both qualitatively and quantitatively through the shift of E_{2g}^1 mode and PL peak energy. In transferred WS_2 monolayer, comparing to suspended WS_2 film a very strong PL quench in WS_2 film supported by SiO_2/Si substrate is observed, which is attributed to charge transfer between the film and the substrate.

Finally, the thermal conductivity of thin-film black phosphorus is determined by its temperature and laser power dependent Raman spectroscopy. An average thermal conductivity of a suspended black phosphorus film has been determined to be 15.8 K/(m·W).

ACKNOWLEDGEMENTS

First of all, I would like to express my deepest gratitude to my advisor, Prof. Yong Zhang, for his great guidance and support during these years of studying in UNC at Charlotte (UNCC) as a ph.D student. I would also like to thank my advisory committee members, Profs. Raphael Tsu, Michael Fiddy, and Qiuming Wei, for their constructive criticism and useful suggestions.

Many thanks to the following people for their kind helps in my experimental works: First, I would like to thank Prof. Linyou Cao's group from North Carolina State University (NCSU) for the collaboration on the research of TMDs and providing the materials grown by CVD. In UNCC where I have been studying, I would like to thank Dr. Lou Deguzman, John Hudak, and Robert Hudgins for their helps in cleanroom experiments and instrument training. I am also grateful to the labmates, Dr. Naili Yue, Henan Liu, Jason Marmon, Qiong Chen, and others who worked in the lab together, for their enlightening discussions and selfless helps on my research.

Finally, I wish to express my heartful gratitude to my family for their support and love in my life, particularly during the period of my ph.D study.

DEDICATION

To my family, with love

TABLE OF CONTENTS

LIST OF FIGURES

LIST OF TABLES

LIST OF ABBREVIATIONS

2D	two-dimensional
3D	three-dimensional
AFM	Atomic force microscope
BN	Boron Nitride
BP	Black Phosphorus
CBM	Conduction band maximum
CCD	Charge-coupled device
CVD	Chemical vapor deposition
DFT	Density functional theory
DR	Double resonance
FWHM	Full width at half maximum
h-BN	Hexagonal boron nitride
HOPG	Highly Ordered Pyrolytic Graphite
LPE	Liquid phase epitaxy
MBE	Molecular beam epitaxy
ME	Mechanical exfoliation/mechanically exfoliated
MLG	Multi-layer Graphene
MOCVD	Metalorganic chemical vapor deposition
MoO_3	Molybdenum trioxide
MoS_2	Molybdenum disulfide
$MoSe_2$	Molybdenum diselenide
N_2	Nitrogen
PECVD	Plasma-enhanced chemical vapor deposition
PL	Photoluminescence
PMMA	Polymethyl methacrylate
PMT	Photomultiplier tube

PS	Polystyrene
RT	Room temperature
SEM	Scanning electron microscope
SiO_2	Silicon dioxide
SLG	Single-layer graphene
STEM	Scanning transmission electron microscopy
TEC	Field electric transistor
TEC	Thermal expansion coefficient
TEM	Tunneling electron microscope
TMDs	Transition Metal Dichalcogenides
VBM	Valence band maximum
vdW	van der Waals
VPE	Vapor phase epitaxy
WO_3	Tungsten trioxide
WS_2	Tungsten disulfide
WSe_2	Tungsten diselenide

CHAPTER 1: INTRODUCTION

1.1   Introduction

"There is plenty of room at the bottom," prophesized the future of nanotechnology by the American physicist Richard Feynman in 1959. Feynman had described a process to manipulate individual atoms and molecules, where surface tension and van der Waals attraction would become more significant [1]. In the past decades, quite a few new detection techniques were invented, including atomic force microscope (AFM) [2], scanning electron microscope (SEM) [3, 4], and tunneling electron microscope (TEM). With the assistance of these tools, more new materials, such as buckminsterfullerene (or bucky-ball, C_{60}) [5], and new structures, such as heterostructures and superlattices [6–8], were able to be discovered and investigated. The scale of materials was minimized from millimeter to nanometer. For years people have been asking this question: "How small can materials be?"

After a great amount of theoretical studies had been carried out on two-dimensional (2D) materials [9], the revolution took place in 2004 when graphene – atomically thin layers of graphite – was experimentally obtained by using Scotch tape, which brought the investigations of solid state materials into a new era – two-dimensional scale [10, 11]. For the first time, it is possible to produce single 2D atomic layers of atoms in the lab. Following graphene came other new layered materials such as boron nitride (BN) [12, 13], transition metal dichalcogenides (TMDs) [14–16], and black phosphorus (BP) [17, 18]. The discovery of these materials has answered the question that we can actually produce thinnest objects imaginable – atomically thick.

With these new materials came new opportunities to examine old problems that have been studied in bulk or three-dimensional (3D) materials, as well as to find new

ones specifically belonging to 2D structures. To study a new material, its physical and chemical properties are the first concerns. For example, as an electronic material, the covalent sp^2 C-C bond in graphene leaves one of carbon's four electrons free on surface giving the film a remarkably higher mobility than graphite [10, 11]. The new properties arising from the downscale of materials set up a new path for future applications. However, these findings also have suggested that the atomically thin layers are susceptible to perturbation within the film itself and from substrates to hold the film, which is in accord with Feynman's predication of the importance of surface tension and van der Waals force. These influences from the film and substrates can change the properties of the film to a significant extent so that thorough research needs to be carried out.

1.2   Outline

This dissertation presents systematic experiments on temperature-dependent high temperature Raman scattering of four 2D materials – graphene, molybdenum disulfide (MoS_2), tungsten disulfide (WS_2) and BP – to investigate their vibrational properties and the interaction between 2D materials and their substrates. For WS_2, temperature-dependent high temperature photoluminescence (PL) were also performed. Spatially resolved Raman and PL mapping was used as well for selected materials. Chapters 1-2 include an overview of the basic concepts and literature work relevant to the experiments and results presented in Chapter 3-6. The experimental section begins in Chapter 3 where we carry out temperature-dependent high temperature Raman scattering on graphene. We find that the hydrocarbonization of polymeric residues leads to the broadening of D and G bands, and the temperature dependence is significantly affected by the substrate due to the difference in thermal expansion of graphene with respect to the substrate. Temperature-dependent Raman scattering results on two typical TMDs – MoS_2 and WS_2 – are presented in Chapter 4 and 5, respectively, where we analyze the temperature-dependent behavior of Ra-

man and PL. A modified form of the work on temperature-dependent Raman results in Chapter 4 has been published in Nanoscale 6, 4920 (2014), and the rest is under preparation. One part of Chapter 5 has appeared in Nano Research (2015), and the rest will be published separately. Chapter 6 extends this work on few-layer thin BP films to investigate the temperature coefficients of BP phonons as well as the thermal conductivity, where substrate effect on the properties of BP films is also discussed. The major content of this chapter has been published in Applied Physics Letters 107, 071905 (2015).

1.3   Structures and Properties of Layered 2D Materials

1.3.1   Graphene

Single-layer graphene (SLG) is the building block of graphite, whose lattice structure is shown Figure 1.1(a). The covalent C-C bonds of graphene are formed by sp^2-hybridized orbitals through σ bond, giving rise to its extraordinary in-plane mechanical strength; whereas the remaining p-electron per atom can bind covalently with neighboring carbons to form a π band that is fully filled but with zero bandgap with the anti-bonding π^* band. Any perturbation that changes the occupation condition of the π or π^* band can lead to the change of electric conductivity [19, 20]. The unit cell of graphene comprises two atoms, denoted as A and B depicted in blue and red, respectively. The distance between nearest-neighbor carbons is 1.42 Å. In reciprocal space, the first Brillouin zone also has a hexagonal shape. With a tight-bonding approach, the band structure is shown in Figure 1.1(b) where valence band maximum (VBM) and conduction band minimum (CBM) touch at K and K' points at the corner of the first Brillouin zone. Within a small energy range near K points, a linear dispersion of electronic excitations is observed, which are called massless Dirac electrons [11]. This linear dispersion relation was first reported by P. R. Wallace in 1946 who showed the band structure of graphene as well as the unusual semimetallic behavior of graphite [9].
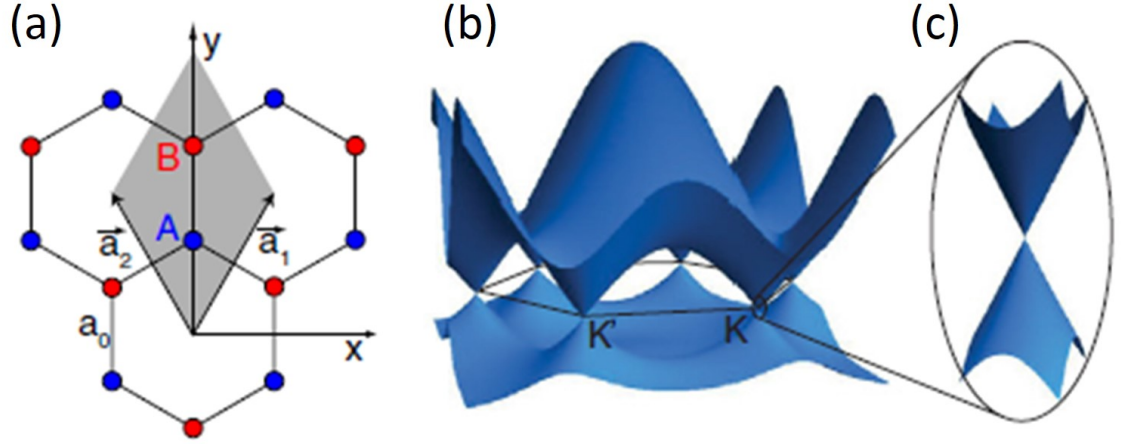
Figure 1.1: Lattice and band structures of graphene. (a) Lattice structure of graphene. a_0 is the nearest-neighbor distance. The unit cell is depicted in gray, together with the primitive lattice vectors a $\vec{a}_{1,2}$. (b)Band structure of graphene. (c) The dispersion relation close to the K-point for small energies. Reproduced from F. Molitor et al. [20].

Multi-layer Graphene (MLG) or even bulk graphite consists of stacked graphene layers which are held together by weak van der Waals (vdW) forces. The stacking order usually is Bernal stacking, i.e. ABA stacking. The distance between layers is 3.35 Å. For bilayer graphene, there are four energy bands if taking into account one $2p_z$ orbital on each of the four atomic sites in the unit cell: a pair of conduction bands and a pair of valence bands. Each pair has a splitting of ∼0.4 eV over most of the Brillouin zone. Near the K points, one CBM and one VBM are split away from zero energy, whereas the other two bands touch at zero energy. Therefore, this region is relevant to electronic properties of bilayer graphene. For MLG, the band structure, though more bands exist, has two bands touching at K points, leading to its electronic properties near K points similar to SLG [21].

SLG has quite a few promising and unique properties: negative thermal expansion coefficient (TEC) [22], unconventional integer quantum Hall effect [23], ultrahigh mobility [24], valley polarization [25], etc. Unfortunately, graphene is a zero-gap material, which means it is not suitable or designable for use in electronic and op-

toelectronic devices. Bandgap engineering has been applied to open a bandgap in SLG, but the gap is only about a few hundred meV which is still too small [26–28]. Additionally, SLG, as an atomic layer, is susceptible to the influence of surrounding environment such as substrates and adsorbents. The non-uniform morphology of SLG like ripples and wrinkles can change its electronic structure and thus modify the thermal, mechanical and electrical behaviors of SLG. Instead, MLG, which is less susceptible to the external environment, was found to show similar behaviors as SLG, contributing to the diversities of graphene's applications. Though graphene has zero gap which limits it to be used in field electric transistor (FET) applications, the extraordinary electrical, mechanical, thermal, and other multitudinous properties of graphene launch the potential applications such as flexible display screens, electrical circuits, and energy storage, as well as various medical, chemical and industrial processes with the use of new graphene materials [29,30].

1.3.2 Transition Metal Dichalcogenides (TMDs)

As the first experimentally-discovered 2D material graphene has a zero bandgap, people started to search for other potential layered materials possessing direct bandgaps. Boron nitride has a graphene-like structure with a direct bandgap of $\sim$5-6 eV which is too large to be used in regular electronic and optoelectronic applications [31]. Following BN, transition metal dichalcogenides (TMDs), another family of layered materials, such as MoS_2, $MoSe_2$, WS_2 and WSe_2, have merged into the family of 2D materials. The bandgap of bulk TMDs is usually indirect, while it transits to direct bandgap when the layer number goes to monolayer [16]. Thus, the most advantageous property of monolayer TMDs comes from their intrinsic bandgaps ranging from $\sim$0.4 to $\sim$2.3 eV [32–36], which covers near infrared and most visible spectral range where most optoelectronic applications happen. For this reason, TMDs have been attracting tremendous interest of research in not only their fundamental nature such as optical and electrical properties but the applications of monolayer or few-layer

TMDs based electronic and optoelectronic devices. In this work, we are only focusing on two TMDs: MoS_2 and WS_2.

1.3.2.1 Molybdenum Disulfide (MoS_2)

The crystal structure of MoS_2 has been studied for more than five decades [37]. As a layered structure similar to graphite, individual MoS_2 layers are stacking upon each to form the bulk through weak vdW force between layers. Each MoS_2 monolayer consists of a plane of molybdenum atoms sandwiched by two planes of sulfur atoms, and all the three plane are hexagonally arranged with the covalently bonded S-Mo-S atoms in a trigonal prismatic arrangement forming a hexagonal crystal structure, as shown in Figure 1.2. The thickness of each MoS_2 monolayer is about 0.65 nm. There are two commonly found crystal structures of MoS_2: hexagonal ($2H-MoS_2$) and octahedral ($1T-MoS_2$) structures [38]. The former is semiconducting, while the latter is metallic. Theoretically, the former is more stable than the latter, out of which has been used to produce monolayer MoS_2 and intensively studied.

Bulk MoS_2 has an indirect bandgap of 1.29 eV (Figure 1.3a) [15]. As the layer number decreases, the CBM moves upward, increasing the overall bandgap [41, 42]. The states at K point in conduction band are mainly due to the d-orbitals of the molybdenum atoms which are barely affected by interlayer interactions, while the states at Γ point hybridization between p_z-orbitals of sulfur atom and the d-orbitals of molybdenum atoms that are affected drastically by interlayer interactions [43, 44]. Therefore, the bands at Γ point are more sensitive to the decrease of layer number. Eventually in the monolayer, the indirect transition becomes larger than the direct transition at K point with a bandgap of ∼1.9 eV [44], as shown in Figure 1.3b. The direct transition of monolayer MoS_2 makes it a promising material that can be applied in FETs to achieve improved performance compared with graphene FETs, or can be used as a promising candidate for lower power electronics, such as photodetectors, due to their bandgaps in visible spectral range, shown in Figure 1.4. Top gated
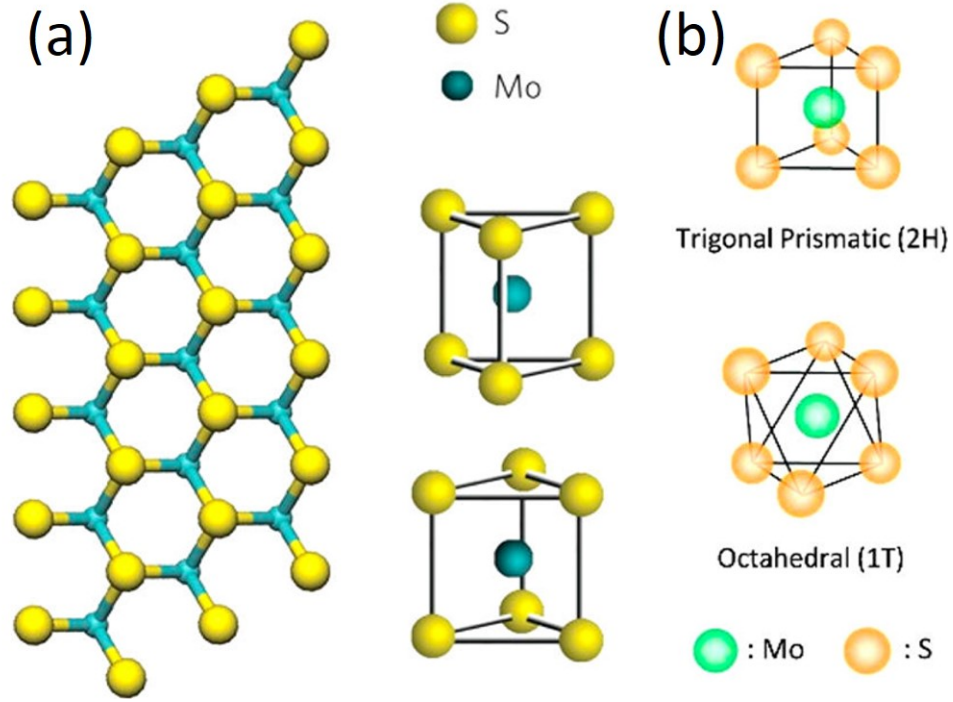
Figure 1.2: Crystal structure of MoS_2. (a) Top view of monolayer hexagonal crystal structure of MoS_2. (b) Two type of unit cell structures of MoS_2: Trigonal prismatic (2H) and Octahedral (1T). Panel (a) reproduced from H. Zeng et al. [39]. Panel (b) reproduced from G. Eda et al. [40].

monolayer MoS_2 FETs showed an excellent on/off current ratio up to 10^8, a mobility of at least 200 $cm^2V^{-1}s^{-1}$ at room temperature, and ultralow standby power dissipation (Figure 1.4a-c) [32]. Ultrasensitive photodetectors based on monolayer MoS_2 exhibited an external photoresponsivity of 880 A/W at a wavelength of 561 nm and a photoresponse in the range of 400-680 nm (Figure 1.3d-e) [45]. These results indicate great potential for applications in MoS_2-based integrated optoelectronic circuits, light sensing, biomedical imaging, video recording and spectroscopy.

Bulk MoS_2 belongs to the space group of D_{6h}, while monolayer MoS_2 belongs to D_{3h} space group. D_{6h} possesses inversion symmetry, while D_{3h} lacks [46]. In monolayer MoS_2, the lack of inversion symmetry combining with spin-orbit interaction breaks the spin degeneracy of the valence and conduction bands along the Γ–K line, results in a band splitting of 148 meV at K point [47]. Thus, at K point of the Brillouin zone
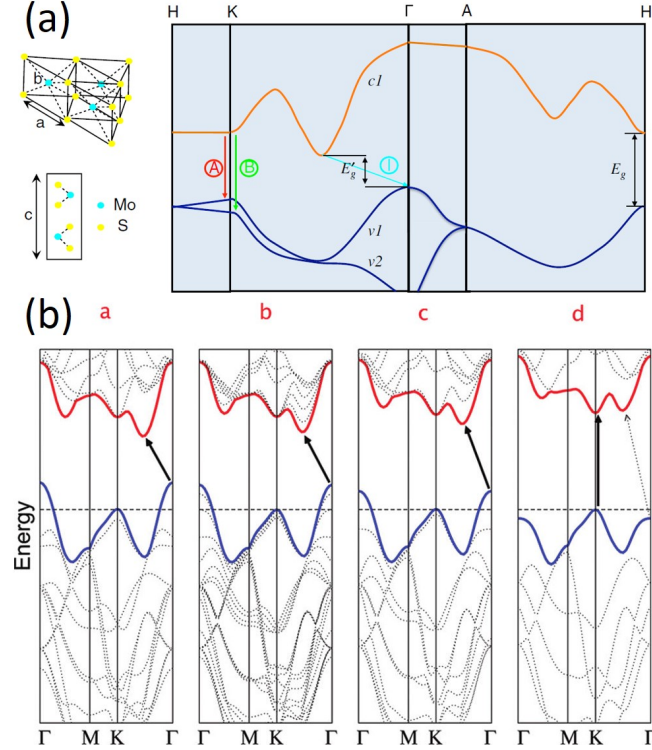
Figure 1.3: Band structure of bulk MoS$_2$. (a) The direct and indirect band gap, as well as the A and B excitons. (b)Transition of the band structure from indirect to direct band gap when the thikness of MoS$_2$ decreases (a d). Panel (a) reproduced from Mak K. F. et al. [15]. Panel (b) reproduced from Splendiani A. et al. [44].

there are two direct transitions between conduction band and valence band, which are known as A and B excitons, respectively (Figure 1.5a) [48, 49]. The energies corresponding to the two excitons are 1.85 eV (A exciton) and 2.00 eV (B exciton). The photoluminescence spectrum of monolayer MoS$_2$ is shown in Figure 1.5c, exhibiting two pronounced emissions at the A and B excitonic transitions [44].

On the other hand, MoS$_2$ possesses very high mechanical strength, showing a higher Young's modulus than that of steel. Its in-plane stiffness is $\sim$180 N/m, corresponding to an effective Young's modulus of 270 GPa [51], compared to 2.4 TPa for graphene [52]. Though it might be argued that its mechanical property is not as exceptional as graphene, monolayer MoS$_2$ is still competent in the applications of flexible electronics and optoelectronics that requires a bandgap.
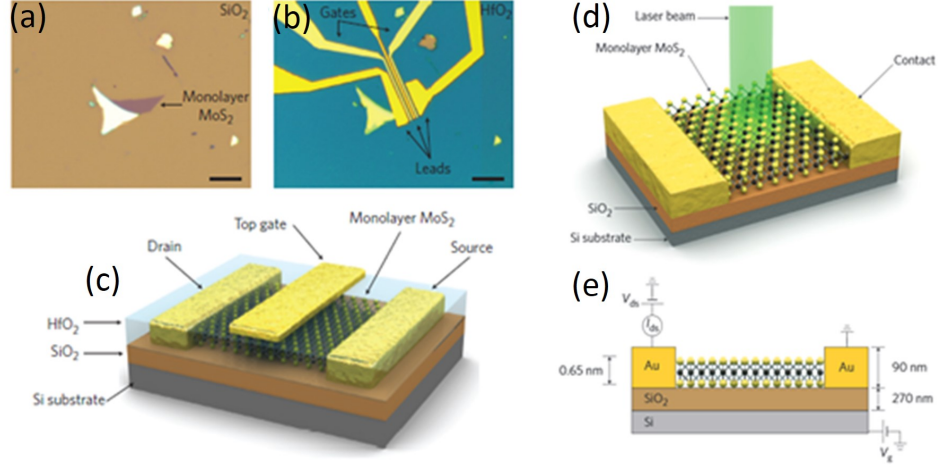
Figure 1.4: Single-layer MoS_2 devices: transistor and photodector. (a) Optical image of a single layer of MoS_2 on SiO_2/Si substrate. (b) Optical image of a transistor based on the flake shown in a. (c) Three-dimensional schematic view of the transistor shown in b. (d)-(e) The schematic view of single-layer MoS_2 based photodetector. Panels a-c reproduced from Radisavljevic B. et al. [32]. Panels d and e reproduced from Lopez-Sanchez O. et al. [45].

1.3.2.2 Tungsten Disulfide (WS_2)

Bulk WS_2 is another representative of the family of TMD semiconductors, which has the same crystal structure as bulk MoS_2 that is belonging to D_{6h} space group. Whereas, monolayer WS_2 belongs to D_{3h} space group. According to optical measurements, monolayer WS_2 exhibits a strong photoluminescence at the direct bandgap transition of $\sim$2 eV, known as A excitonic transition (Figure 1.5d). Due to the strong spin-orbit coupling induced band splitting, another direct transition at K point has also been observed at the energy of $\sim$2.4 eV (i.e. B exciton). The valence band splitting for monolayer WS_2 is theoretically calculated to be 426 meV (Figure 1.5b), which is almost three times of that for monolayer MoS_2 (148 meV).

Based on theoretical prediction, among the semiconducting 2D TMDs WS_2 should have the highest mobility due to the reduced effective mass [53]. FETs based on monolayer WS_2 has been investigated to have a room temperature mobility of $\sim$50 $cm^2V^{-1}s^{-1}$ with an on/off ratio of 106 [54]. With long *in situ* annealing to improve
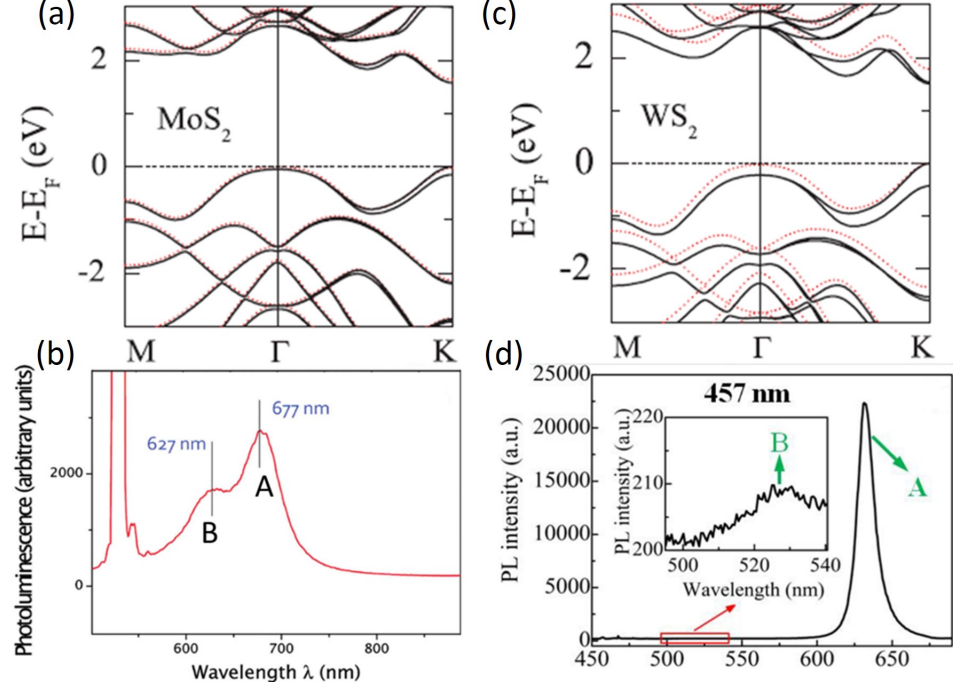
Figure 1.5: Electronic band structures and PL spectra of monolayer MoS_2 and WS_2. (a) and (c) The electronic band structures calculated for (a) MoS_2 and (c) WS_2 monolayer systems with (solid line) and without (dotted line) considering the spin-orbit interaction. (b) and (d) The PL spectra of monolayer (b) MoS_2 and (d) WS_2, showing both A and B excitons. Panels a and c reproduced from Zhu Z.Y. et al. [47]. Panel b reproduced from Splendiani A. et al. [44]. Panel d reproduced from Cong C. et al. [50].

the contact transparency and remove adsorbates, the mobility saturates below 83 K at 140 $cm^2V^{-1}s^{-1}$ for monolayer WS_2 and above 300 $cm^2V^{-1}s^{-1}$ for bi-layer one. Besides, with ionic liquid gated FET structures, the light emission from both mono- and bilayers of WS_2 has become a reality, though the quantum efficiency is low at this stage [33].

1.3.3 Black Phosphorus/Phosphorene

BP or phosphorene has become a newer class of 2D layered materials, which is the most stable form among various phosphorus allotropies. Similar to graphite and TMDs, bulk BP consists of atomic monolayers, i.e., phosphorene, connected by weal interlayer bonding while within each individual layer the structure is covalently bond-ed. Each phosphorus atom is covalently bonded to three phosphorus neighbors with

one lone pair electrons left, forming a puckered honeycomb structure as shown in Figure 1.6a-b [55]. The space group of bulk BP is D_{2h}; thus, BP or phosphorene has lower in-plane symmetry compared to graphite and TMDs, resulting in its unique in-plane anisotropic nature. Therefore, BP's optical, electrical, mechanical, thermoelectric, and other miscellaneous properties are expected to show angle dependence [55].
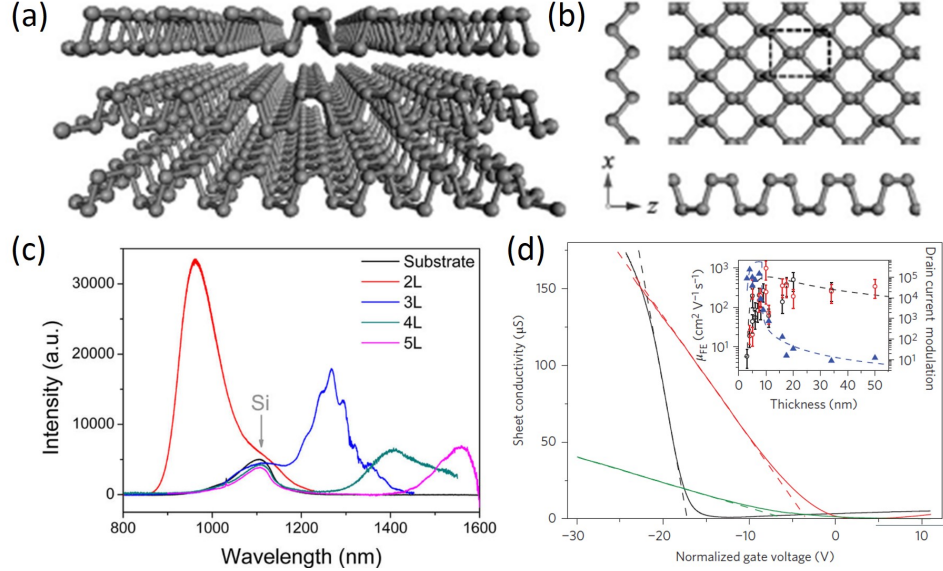
Figure 1.6: The lattice structure, PL spectra, and I-V characteristic of a few-layer phosphorene FET. (a) The puckered structure of a few-layer BP thin film. (b) Top view of monolayer BP. The zigzag and armchair directions are denoted as x and z axis, respectively. (c) PL spectra of two-, three-, four-, and five-layer phosphorenes. (d) Drain-source current Ids as a function of bias Vds at different gate voltages for a few-layer phosphorene FET on a SiO_2/Si substrate. Panels a and b reproduced from Wu J. et al. [55]. Panel c reproduced from Zhang S. et al. [56]. Panel d reproduced from Li L. et al. [18].

Unlike semiconducting TMDs having direct bandgap only in monolayer, BP possesses a layer-dependent direct bandgap ranging from 0.3 eV for the bulk to 1.5 eV for monolayer (Figure 1.6c), enabling the applications of BP for high-performance optoelectronic devices [56]. Few-layer BP based FETs has been shown to have reliable performance at room temperature with an on/off ration on the order of 105 and a hole mobility more than ~1,000 $cm^2V^{-1}s^{-1}$ (Figure 1.6d) [18]. Besides FET application, BP can also be used as photosensors and solar cells [57–60]. However,

few layer BP is not air stable [61].

1.4   Fabrication of Layered Materials

A key component in nanotechnology is the production of the materials from which electronic/optoelectronic devices are made. These materials are usually required to be high perfection and high purity. The earliest growth techniques involved in growing bulk crystal from using one of the bulk crystal growth techniques: Czochralski, Bridgman, or float zone. These methods are appropriate for the synthesis of large-volume crystals to produce high purity, near perfect single crystal, but has no flexibility to control alloy composition or grow heterostructures. Whereas, epitaxial growth techniques have been specially developed for the synthesis of high-quality semiconductor alloys and heterostructures with precise controls, and normally single-crystal thin films are deposited on a substrate. These techniques include liquid phase epitaxy (LPE), vapor phase epitaxy (VPE), molecular beam epitaxy (MBE) and metalorganic chemical vapor deposition (MOCVD). There are other thin-film deposition techniques that can be used for the deposition of polycrystalline semiconductors, including plasma-enhanced chemical vapor deposition (PECVD), vacuum evaporation, and sputtering [62,63].

For 2D materials their thicknesses are one or few atomic monolayers, which makes most of these growth techniques mentioned above infeasible to be used in the production of 2D materials. However, up to now, a large number of methods have been developed, which can be categorized into two major classes: bottom-up methods and top-down methods. The former involves the chemical reaction of molecules to form covalently linked 2D nanosheets, such as chemical vapor deposition (CVD). The latter depends on the exfoliation of bulk layered materials, such as mechanical exfoliation (ME). Both methods can yield high-quality monolayers with a small number of defects that is suitable for applications of electronic/optoelectronic devices. Here, we mainly discuss two widely used techniques, i.e. ME and CVD.

1.4.1 Mechanical Exfoliation

The birth of the first graphene is attributed to the mechanical exfoliation of HOPG (Highly Ordered Pyrolytic Graphite) in 2004. The general idea of this method is to exfoliate graphene layers from the bulk HOPG surface by applying normal and/or shear force with Scotch tape or tips of scanning probes [64–68]. The weak van der Waals attraction between graphene layers makes it possible to isolate single-layer graphene from the surface of the bulk. The procedure is shown in Figure 1.7. A small flake of graphite is placed on Scotch tape, and the tape is folded repeatedly over the graphite until it is coated with a relatively thin layer of graphite. Then the tape is pressed onto a silicon wafer coated with a 300-nm thick SiO_2 layer. In order to see the graphene optically, the thickness of SiO_2 layer is selected to be 90 nm or 285 nm to achieve the optimal optical contrast around 550 nm that results from interference effect. One may need to attempt numerous times of mechanical exfoliation, and on a good day, monolayer graphene with dimensions of tens of micrometers should be able to be obtained. This method has also been used to produce monolayer h-BN (hexagonal boron nitride), TMDs and BP by many researchers, including myself.

Though very high-quality and large-size 2D materials can be produced with this method, it is extremely labor-intensive and time-consuming, which makes it limited to laboratorial research and impossible for large-scale industrial production. For this reason, people developed other mechanical exfoliation methods, such as using sonication, ball milling, fluid dynamics, supercritical fluids, etc. [69].

1.4.2 Chemical Vapor Deposition (CVD)

Within the bottom-up concept, the most widely used growth technique to synthesize 2D materials is CVD. In this process, desired materials are deposited onto the substrate surface after the reaction and/or decomposition of gaseous precursors. With precisely control, it is possible to grow high-quality and large-scale 2D materials for the high demand toward the implementation of these materials in industrial
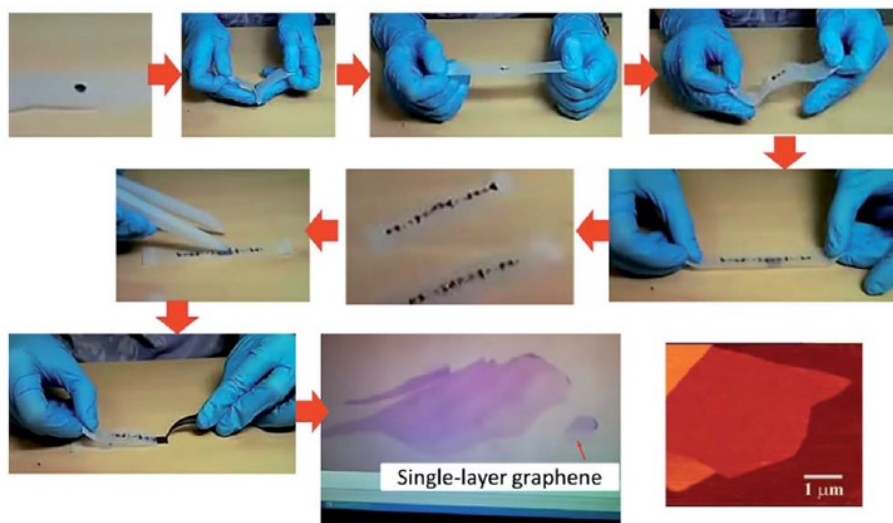
Figure 1.7: An illustration of the procedure of producing graphene from graphite by the technique of mechanical exfoliation with the scotch tape. Reproduced from Yi M. et al. [69].

applications.

For the synthesis of graphene, people tried a variety of metal substrates such as Ni, Cu, Ru, Ir, Pt, Co, Pd, and Re, showing different carbon solubility and catalytic effect. During the CVD growth process, gas species are fed into the reactor and pass through the hot zone, and then the gaseous precursors decompose, leaving carbon particles at the surface of metal substrate and forming monolayer and few-layers graphene (Figure 1.8a). Among all these candidates of metal substrates, Ni has relatively high carbon solubility at elevated temperatures; however, the percentage and size of monolayer graphene region are limited by the quality of Ni films. Whereas, graphene deposited on polycrystalline Cu, though Cu has ultralow carbon solubility, is uniform monolayer, which makes Cu a better substrate for monolayer graphene synthesis [68]. To facilitate graphene for electronic and photoelectronic applications, monolayer graphene on metal substrate needs to be transferred onto designated substrates. Figure 1.8b shows the schematic diagram of the transfer process by using a thin-layer of polymethyl methacrylate (PMMA) as the transfer medium. This technique has also been broadly used to transfer other CVD-grown 2D materials to

arbitrary substrates.
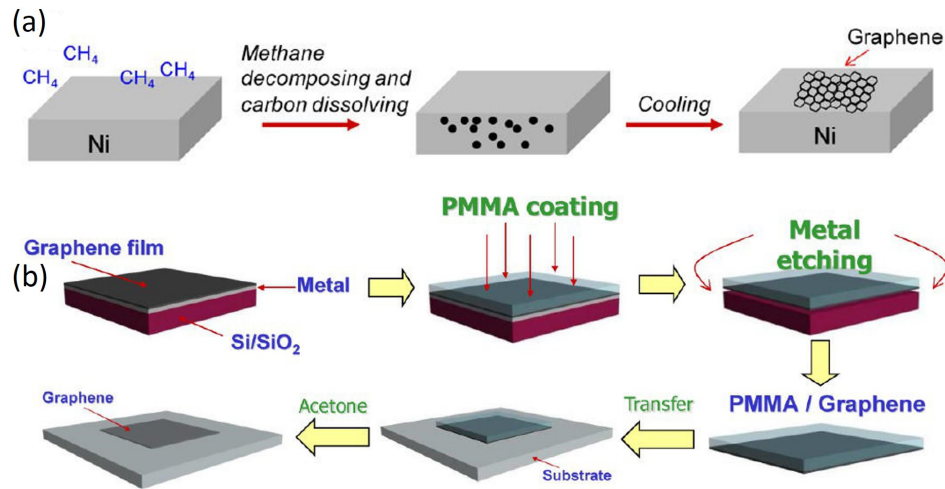
Figure 1.8: An illustration of the procedure of producing graphene from graphite by the technique of mechanical exfoliation with the scotch tape. Reproduced from Yi M. et al. [69].

The CVD growth process of TMDs is quite similar to that of graphene. Taking the growth of thin MoS_2 as an example, there are three ways corresponding to three precursors: ammonium thiomolybdate $[(NH_4)_2MoS_4]$ solution [70], a thin deposition of elemental molybdenum [71, 72], or molybdenum trioxide $[MoO_3]$ powder [73, 74], as shown in Figure 1.9. The substrates mostly used are SiO_2/Si and sapphire. In most cases, MoS_2 grown on sapphire substrates exhibited better quality and larger grains than those grown on SiO_2 [37]. In addition, scattered single-crystalline MoS_2 triangles are initially grown, and then the triangle grains expand to join neighboring MoS_2 grains at the boundaries as the growth time increases. Eventually, complete MoS_2 films are formed. The synthesis of WS_2 is very similar to that of MoS_2. Up to now no CVD synthesis of phosphorene has been reported yet. In all reported research on BP, the materials were obtained by the ME method.

1.5   Aims of Research

As Feynman predicted, materials of nanoscale must take into consideration of the surface tension and vdW force which would be significant to material properties.
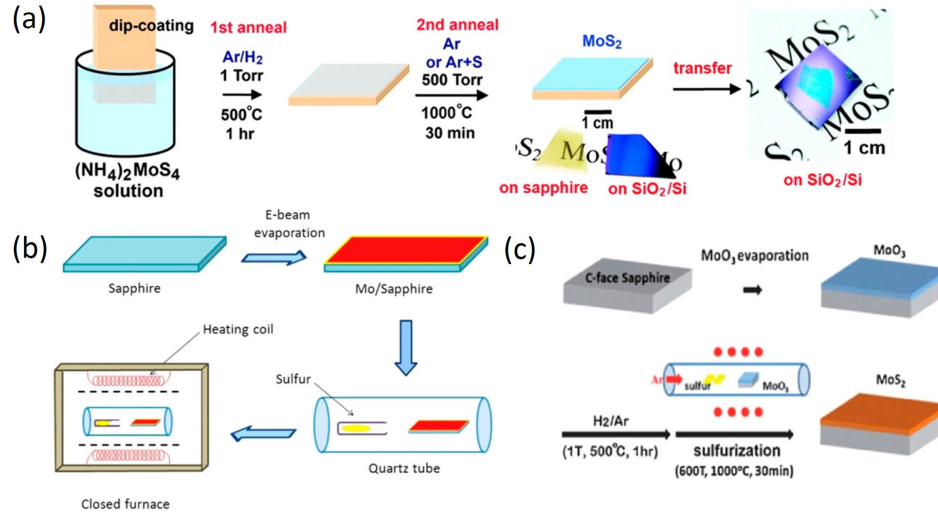
Figure 1.9: Growth techniques of MoS$_2$ monolayers. (a) MoS$_2$ growth on SiO$_2$/Si substrate using (NH$_4$)$_2$MoS$_4$. (b) Growth of MoS$_2$ directly from the sulfurization of elemental molybdenum. (c) Growth using MoO$_3$ as the precussors. Panel a reproduced from Liu K. et al. [70]. Panel b reproduced from Laskar M. R. et al. [72]. Panel c reproduced from Lin Y. et al. [74].

For 2D materials, they have a thickness of one or few atomic layers, less than 1 nm. Consequently, it is extremely susceptible for them to be influenced by surrounding environment, such as adsorbates at the surface and the interaction with substrates. In the preparation of 2D materials, the perturbations of fabrication process, such as temperature, precursor ratios, etc., can be the origination of the changes of material properties. For instance, mechanical exfoliation may introduce polymer residues to the film as well as non-planar morphology, while CVD-grown films could have strong chemical bonding with substrate, i.e. strong interaction between the substrate and the films. Meanwhile, possible defects introduced to the films during fabrication, which may significantly modify the optical and electrical properties, should be taken into account.

Actually, all these influences in 2D materials can be interpreted as two major factors: (1) strain effect, and (2) doping or charge exchange effect. For instance, the defects, polymer residues and charge transfer from substrate are likely to change the charged carrier concentration or doping level in the film; whereas the non-planar

morphology indicates non-uniform strain distribution over the film. As is well-known, Raman spectroscopy is a nondestructive technique, which has been widely used to characterize the structural and electronic properties of materials. It is very sensitive to the changes of strain and doping in the materials.

Therefore, the first aim of this research is to investigate the strain and doping effects of 2D materials as well as their interactions with substrate, and thus understand the intrinsic properties of the 2D material. In order to accomplish this, 2D films are prepared on different substrates by different fabrication techniques. By comparing the Raman results combining with PL spectroscopic results, we are able to distinguish the contributions of different effects in the changes of optical and electrical properties of 2D materials.

Besides, for any kind of material, the goal of studying is also application-oriented. Thus, it is also true for 2D materials that they can be applied in electronic/optoelectronic devices, particularly FETs. However, because of the internal resistance, significant heat will be generated with bias applied, which consequently can change the performance of the devices. With increasing temperature, the structural and electronic properties of the 2D materials used in devices can be modified. Since Raman spectroscopy can effectively determine the property changes, a temperature dependent Raman spectroscopy investigation on 2D materials can help us understand how self-heating changes the properties of materials and hence the performance of devices, which leads to the second aim of research that is to investigate the vibrational properties and electron-phonon coupling in 2D materials by using temperature dependent high temperature Raman spectroscopy. This study can further help us understand those effects mentioned in the first aim of research. Additionally, by combining temperature dependent Raman studies with laser power dependent Raman studies, we are able to extract thermal conductivity of 2D materials.

The final aim of this dissertation is to understand the electron-hole interaction

of 2D materials. For instance, MoS_2 has a direct bandgap that is revealed by strong PL quantum yield. The PL involves in the recombination of electrons and holes. The recombination in 2D material are more complex than the bulk because it is more easily to be perturbed (either enhanced or quenched) by any slight change in the film internally or externally. PL spectroscopy and temperature dependent PL studies enable us to investigate the radiative and the non-radiative recombination of photo-generated carriers in 2D materials.

CHAPTER 2: TEMPERATURE DEPENDENCE OF RAMAN SCATTERING AND PHOTOLUMINESCENCE

2.1 Temperature Dependence of Raman Scattering

In this dissertation, temperature dependent Raman spectroscopy is the most used technique for investigating the structural and electronic properties of 2D materials as well as their changes with temperature, in particular in the elevated temperature region from room temperature (RT) up to the decomposition temperature of the material of interest. Raman spectroscopy is a spectroscopic technique based on Raman scattering or Raman effect. Before we move on to discuss temperature dependence of Raman scattering, we should review Raman scattering first.

2.1.1 Raman Scattering

Raman scattering, in a word, is the inelastic scattering of a photon. The phenomenon was first discovered by C. V. Raman and K. S. Krishnan in liquids [75], and by G. Landsberg and L. Mandelstam in crystals [76], among whom C. V. Raman was granted Nobel Prize in 1930. Unlike Rayleigh scattering where scattered photon have the same energy as the incident photon, Raman scattering results in scattered photon having a frequency different from that of the incident photon. The frequency difference between the incident photon and the scattered phonon through Raman scattering, observed by Raman spectroscopy, provides a fingerprint to identify and analyze molecules in chemistry, making it recognized as a landmark tool in chemistry history for analyzing the composition of liquids, gases, and solids.

2.1.1.1 Raman Theory

According to classical treatment of Raman scattering [77, 78], the incident photons can be considered as an electromagnetic wave (usually laser beam) which is

expressed as:

$$\boldsymbol{E}(\boldsymbol{r},t) = \boldsymbol{E}_i(\boldsymbol{k}_i,\omega_i)\cos(\boldsymbol{k}_i \cdot \boldsymbol{r} - \omega_i t), \tag{2.1}$$

where $\boldsymbol{E}(\boldsymbol{r},t)$ is the electric field stength, $\boldsymbol{E}_i(\boldsymbol{k}_i,\omega_i)$ the amplitude, $\boldsymbol{k}_i$ the wavevector, and ω_i the frequency of the phonons. When the medium is irradiated by the wave/light, a sinusoidal polarization $\boldsymbol{P}(\boldsymbol{r},t)$ will be induced:

$$\boldsymbol{P}(\boldsymbol{r},t) = \boldsymbol{P}(\boldsymbol{k}_i,\omega_i)\cos(\boldsymbol{k}_i \cdot \boldsymbol{r} - \omega_i t) = \eta(\boldsymbol{k}_i,\omega_i)\boldsymbol{E}_i(\boldsymbol{k}_i,\omega_i)\cos(\boldsymbol{k}_i \cdot \boldsymbol{r} - \omega_i t). \tag{2.2}$$

where η is the electrical susceptibility of the medium. Its frequency and wavevector are the same as those of the incident photons. If the medium is vibrating with a frequency of ω_m, the atomic displacement $\boldsymbol{Q}(\boldsymbol{r},t)$ can be written as:

$$\boldsymbol{Q}(\boldsymbol{r},t) = \boldsymbol{Q}(\boldsymbol{q},\omega_m)\cos(\boldsymbol{q} \cdot \boldsymbol{r} - \omega_m t) \tag{2.3}$$

with wavevector $\boldsymbol{q}$. The normal modes of the molecule vibrations are called *phonons*. These atomic vibrations will modify η, and it can be expressed as a function of $\boldsymbol{Q}$ with a Taylor series:

$$\eta(\boldsymbol{k}_i,\omega_i,\boldsymbol{Q}) = \eta_0(\boldsymbol{k}_i,\omega_i) + (\partial\eta/\partial\boldsymbol{Q})_0\boldsymbol{Q}(\boldsymbol{r},t) + \cdots, \tag{2.4}$$

where η_0 denotes the electric susceptibility of the medium without fluctuations. The second and higher terms in Eq.(2.4) represents the oscillating susceptibilities induced by the lattice displacement $\boldsymbol{Q}(\boldsymbol{r},t)$. Substituting Eq.(2.4) into Eq.(2.2), the polarization $\boldsymbol{P}(\boldsymbol{r},t,\boldsymbol{Q})$ of the medium can be expressed as:

$$\boldsymbol{P}(\boldsymbol{r},t,\boldsymbol{Q}) = \boldsymbol{P}_0(\boldsymbol{r},t) + \boldsymbol{P}_{ind}(\boldsymbol{r},t,\boldsymbol{Q}), \tag{2.5}$$

where

$$\boldsymbol{P}_0(\boldsymbol{r}, t) = \eta_0(\boldsymbol{k}_i, \omega_i)\boldsymbol{E}_i(\boldsymbol{k}_i, \omega_i)\cos(\boldsymbol{k}_i \cdot \boldsymbol{r} - \omega_i t) \tag{2.6}$$

is a polarization vibrating in phase with the incident photons and

$$\boldsymbol{P}_{ind}(\boldsymbol{r}, t, \boldsymbol{Q}) = (\partial\eta/\partial\boldsymbol{Q})_0\boldsymbol{Q}(\boldsymbol{r}, t)\boldsymbol{E}_i(\boldsymbol{k}_i, \omega_i)\cos(\boldsymbol{k}_i \cdot \boldsymbol{r} - \omega_i t) \tag{2.7}$$

is a polarization wave induced by the phonon. To determine the frequency and wavevector of $\boldsymbol{P}_{ind}$ the Eq.(2.7) can be rewritten as:

$$\begin{aligned}
\boldsymbol{P}_{ind}(\boldsymbol{r}, t, \boldsymbol{Q}) =&(\partial\eta/\partial\boldsymbol{Q})_0\boldsymbol{Q}(\boldsymbol{q}, \omega_m)\cos(\boldsymbol{q} \cdot \boldsymbol{r} - \omega_m t) \\
&\times \boldsymbol{E}_i(\boldsymbol{k}_i, \omega_i)\cos(\boldsymbol{k}_i \cdot \boldsymbol{r} - \omega_i t) \tag{2.8a} \\
=&\frac{1}{2}(\partial\eta/\partial\boldsymbol{Q})_0\boldsymbol{Q}(\boldsymbol{q}, \omega_m)\boldsymbol{E}_i(\boldsymbol{k}_i, \omega_i) \\
&\times \{\cos[(\boldsymbol{k}_i + \boldsymbol{q}) \cdot \boldsymbol{r} - (\omega_i + \omega_m)t] \\
&+ \cos[(\boldsymbol{k}_i - \boldsymbol{q}) \cdot \boldsymbol{r} - (\omega_i - \omega_m)t]\}. \tag{2.8b}
\end{aligned}$$

According to the classical theory, the $\boldsymbol{P}_{ind}$ expressed in Eq.(2.8b) consists of two sinusoidal terms with the frequencies of $\omega_i - \omega_m$ and $\omega_i + \omega_m$, which are denoted as *Stokes* and *anti-Stokes* shifted waves, respectively. If $(\partial\eta/\partial\boldsymbol{Q})_0$ goes to zero, $\boldsymbol{P}_{ind}$ is zero which indicates the vibration is not Raman-active. In other words, for a Raman-active vibration, the rate of polarizability change with the vibration must not be zero.

2.1.1.2   Raman Tensors and Selection Rules

Now that we understand the origin of Raman shift we will discuss the intensity of scattered radiation. The intensity of the scattered radiation, I_s, is related to the time-averaged power radiated by the induced polarizations $\boldsymbol{P}_{ind}$ into unit solid angle,

which can be expressed as [78]:

$$I_s \propto |\boldsymbol{e}_i \cdot \mathcal{R} \cdot \boldsymbol{e}_s|^2, \qquad (2.9)$$

where $\boldsymbol{e}_i$ and $\boldsymbol{e}_s$ are the polarizations of the incident and scattered lights, and $\mathcal{R}$ is known as the Raman tensor. By introducing a unit vector $\hat{\boldsymbol{Q}} = \boldsymbol{Q}/|\boldsymbol{Q}|$ parallel to the phonon displacement $\mathcal{R}$ can be defined as:

$$\mathcal{R} = (\partial \eta / \partial \boldsymbol{Q})_0 \hat{\boldsymbol{Q}}(\omega_m) \qquad (2.10)$$

In general $\mathcal{R}$ is a complex second-rank tensor with components like η, which can be obtained by a contraction of $\boldsymbol{Q}$ and the derivative of η with respect to $\boldsymbol{Q}$. The symmetry of the Raman tensor or the corresponding Raman-active mode can be deduced from measuring the dependence of the scattered intensity on the incident and scattered polarizations. On the other words, Raman scattering can be applied to determine both the frequency and symmetry of a zone-center phonon mode. The manipulation of the polarizations $\boldsymbol{e}_i$ and $\boldsymbol{e}_s$ and scattering geometries to switch on and off the vibrational modes is called Raman selection rules. For a Raman tensor, it is symmetric only when the difference in frequency between the incident and scattered light can be ignored. In practice, it is assumed to be symmetric because the laser frequency is much larger than phonon frequency. Usually non-symmetric components in the Raman tensor can be introduced only by magnetic fields [78].

2.1.2   Temperature Effect of Phonons

Considering the elastic vibrations of a crystal with one atom in the primitive cell, the motion of each individual atom within a plane can be written as (Figure 2.1) [77]:

$$M\frac{d^2u_s}{dt^2} = C(u_{s+1} + u_{s-1} - 2u_s), \qquad (2.11)$$

where C is the force constant between nearest-neighbor planes and will differ for longitudinal and transverse waves, M is the mass of an atom, and u_s, u_{s+1} and u_{s-1} are the displacements of the plane s, $s+1$ and $s-1$, respectively. Assumptions are made that all the displacements have the same time dependence $\exp(-i\omega t)$ and that this differential equation has traveling wave solution, i.e.,

$$u_{s\pm1} = u \cdot \exp(isKa)\exp(\pm iKa), \qquad (2.12)$$

where a is the spacing between planes and K is the wavevector. Therefore, the dispersion relation between ω and K can be expressed as:

$$\omega^2 = (2C/M)(1 - \cos Ka). \qquad (2.13)$$

Within the harmonic approximation, phonons have no interaction and an infinite lifetime. However, the main focus of this work is on the temperature dependence of Raman scattering. At very low temperatures, the thermal effect of lattice vibration can be described by a harmonic model, which is limited in the potential energy of terms quadratic in the interatomic displacements. However, as temperature goes up the harmonic theory would yield these consequences: (1) phonons do not decay or change with time; (2) there is no thermal expansion; (3) heat capacity becomes constant at high temperatures; (4) adiabatic and isothermal elastic constants are equal, and the elastic constants are independent of pressure and temperature [77]. In reality, none of these implications holds true. Therefore, the anharmonic (higher than quadratic) terms in the interatomic displacements should be taken into account to correct the deficiencies of the harmonic theory. The change of phonon frequency and width with temperature is a manifestation of anharmonic effects in the lattice potential energy, which is the main focus of this work.

The change of phonon frequency with temperature ($\Delta\omega$) can be divided into two
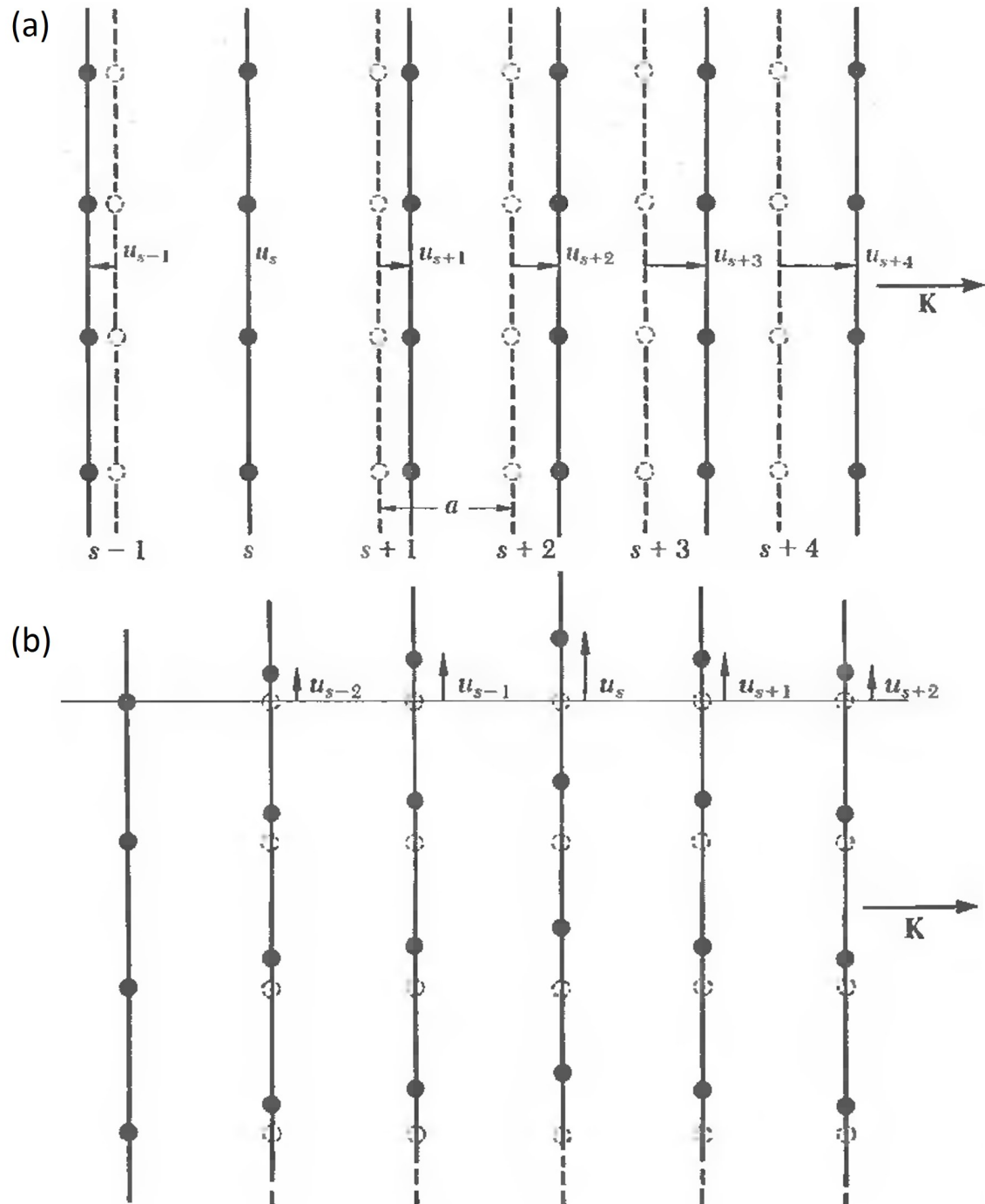
Figure 2.1: The displacement of planes of atoms. (a) Planes of atoms as displaced during passage of a longitudinal wave. (b) Planes of atoms when displaced as a longitudinal wave (solid lines). The dashed lines represents atoms in equilibrium. The coordinate u measures the displacement of the planes. Reproduced from Kittel C. [77].

parts: (1) thermal expansion of the lattice ($\Delta\omega_E$), (2) anharmonic effect ($\Delta\omega_A$) which causes the change of phonon self-energy. Thus Raman shift can be written as [79, 80]:

$$\Delta\omega(T) = \Delta\omega_E(T) + \Delta\omega_A(T), \tag{2.14}$$

where T is thecrystal temperature. Although the first term, $\Delta\omega_E$, in Eq.(2.12) stands for the thermal expansion which occurs as a result of anharmonicity, it affects the harmonic frequencies through the change of force constant C, which may change with volume. Whereas, the second term is the purely anharmonic contribution to the shift, also known as the "self-energy" shift, which is only considered as a function of temperature T at constant volume.

Firstly, the contribution of thermal expansion to the shift of phonon frequency can be estimated by Grüneisen approximation, expressed as [79, 81]:

$$\Delta\omega_E(T) = \omega_{T_0}\exp\left(-m\gamma \int_{T_0}^{T} \alpha \ \mathrm{d}T\right) - \omega_{T_0}, \tag{2.15}$$

where ω_{T_0} is the phonon frequency at temperature T_0; m is the degeneracy, for cubic bulk crystal, m equals 3; γ is the Grüneisen parameter, and α is the TEC of the crystal.

After separating out the contribution of the thermal expansion, the remaining change of phonon frequency is attributed to the pure temperature effects. These effects are manifested as the higher terms of the interatomic displacement, which are correlated to an interaction of phonons. As a result, a phonon from a given state will decay into other phonons after a finite time. In a perturbation theory, the vibrational Hamiltonian can be written as [82]:

$$H = H_0 + H_A \tag{2.16}$$

where H_0 is the harmonic Hamiltonian, and H_A is the anharmonic Hamiltonian. H_A consists of the perturbation terms involving three, four, five, and more interacting phonons. As the simplest case, three-phonon interaction involves in decay of a phonon into two other phonons and vice-versa.

In thermal equilibrium, the phonon occupation number follows the Planck distribution function [77]:

$$\langle n \rangle = \frac{1}{\exp\left(\hbar\omega/\tau\right) - 1}, \tag{2.17}$$

where $\langle \cdots \rangle$ denotes the average in thermal equilibrium, and $\tau = k_B T$ (k_B is Boltzmann constant). Normally, the change of phonon frequency arising from pure temperature effects can be derived from a semi-quantitative simple Klemens model [82, 83], which is expressed as:

$$\Delta\omega_A(T) = A\left(1 + \frac{2}{e^x - 1}\right) + B\left(1 + \frac{3}{e^y - 1} + \frac{3}{(e^y - 1)^2}\right) \tag{2.18a}$$

$$= A\left(1 + 2\langle n_1 \rangle\right) + B\left(1 + 3\langle n_2 \rangle + 3\langle n_2 \rangle^2\right), \tag{2.18b}$$

where $x = \hbar\omega/(2k_B T)$, $y = \hbar\omega/(3k_B T)$, and A and B coefficients are constants, representing contribution of three- and four-phonon processes to the change of phonon frequency, respectively. $\langle n_1 \rangle$ and $\langle n_2 \rangle$ are the occupation numbers of phonons with frequencies of $\omega/2$ and $\omega/3$. Here the assumptions are made that three-phonon process involves in the decay of a phonon into two phonons with the same frequency of $\omega/2$, and four-phonon process into three phonons with the same frequency of $\omega/3$.

The anharmonicity arising from temperature effects also involves the damping of phonons, which is attributed to the decay of phonons as well. If only three- and four-phonon processes are taken into consideration, the damping constant $\Gamma(T)$ can

be written as [82]:

$$\Gamma(T) = C\left(1 + \frac{2}{e^x - 1}\right) + D\left(1 + \frac{3}{e^y - 1} + \frac{3}{(e^y - 1)^2}\right) \qquad (2.19a)$$

$$= C\left(1 + 2\langle n_1\rangle\right) + D\left(1 + 3\langle n_2\rangle + 3\langle n_2\rangle^2\right), \qquad (2.19b)$$

where C and D coefficients are constants. In Raman spectroscopy, the damping constant reflects the broadening of Raman peaks.

2.2   Temperature Dependence of photoluminescence (PL)

Besides Raman spectroscopy, in this dissertation PL spectroscopy was another useful technique to investigate the electronic structures of the 2D materials. It is a non-destructive method often used to analyze the electronic structure near the fundamental band gap, and light emission processes related to doping, and impurity levels of the crystal. Temperature dependent PL is often used to investigate radiative and non-radiative recombination process and exciton-phonon interactions in semiconductor materials.

2.2.1   Photoluminescence (PL)

Most of time, PL is the light emission after the absorption of excitation photons of energy $(\hbar\omega_{ex})$ higher than that of the band gap, and the energy $(\hbar\omega_{em})$ of radiated photons is lower than the excitation photons.

PL can be divided into three stages, as indicated in Figure 2.2. First, the electrons in the valence band (ground states) are excited into the conduction band (excited states) by absorbing photons with energy of $\hbar\omega_{ex}$, creating electron-hole pairs. Second, the non-equilibrium electrons and holes tend to reach thermal equilibrium, which is cause by energy transfer to the crystal lattice, i.e., a step-by-step excitation of lattice vibrations. As a result, the electrons relax to the CBM while the holes to the VBM. Finally, the electron-hole pairs recombine through the emission of light whose energy is $\hbar\omega_{em}$. In high-quality semiconductors, the PL process discussed above is

the typical transition which occurs at the band edge, which is dominated by radiative annihilation of electron-hole pairs (excitons) producing the so-called free exciton peak.
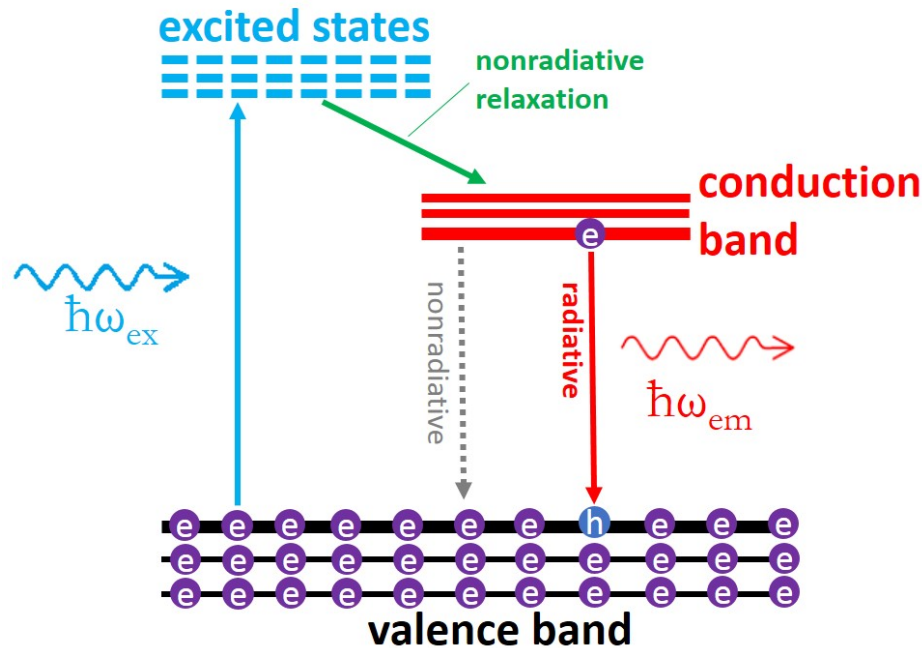
Figure 2.2: Sketch of the basic processes involved in a typical PL of semiconductors.

However, quite often a semiconductor contains various impurity and defect states within the fundamental bandgap, of which some are shallow, i.e., close to the band edges, and some are deep, i.e., away from the band edges. Such impurities or defects usually play the roles of donors or acceptors. Under equilibrium conditions, some of the electrons from the donors will be captured by the acceptors, resulting in donor (D^+) and acceptor (A^-) states. By optical excitation, electrons and holes that created in the conduction and valence bands, respectively, will then be captured by D^+ and A^- states to produce neutral D_0 and A_0 centers. Some of the electrons on the neutral donors will recombine radiatively with holes on the neutral acceptors. The process is known as a donor-acceptor pair transition. Meanwhile, the excitons may also be attracted to impurities such as donors or acceptors to form bound excitons

at low temperature. This attraction lowers the exciton energy, hence the energy of radiated photons is lower than that of the band-edge free-exciton transition. The recombination of an exciton bound to a neutral donor atom is usually denoted by D_0X, while that to a neutral acceptor A_0X. Excitons can also bind to ionized impurities, form bound excitons denoted as D^+X or A^-X. These complex, known as trions, can be considered as charged excitons, which are abbreviated as X^+ (positively charged) and X^- (negatively charged) [78].

2.2.2 Temperature Dependence of Photoluminescence (PL)

The PL emission spectra usually show a characteristic temperature dependence. As the temperature increases, the emission energy usually shifts to a lower energy, the emission band broadens, and at high temperatures the emission is quenched. Temperature dependent PL spectroscopy is often used to investigate the radiative and non-radiative recombination processes and exciton-phonon interaction in semiconductor materials. In general, the thermal quenching in PL intensity with increasing temperature is attributed to the thermal activation of nonradiative recombination processes.

A widely used relation for the variation of the energy gap (E_g) with temperature (T) in semiconductor materials is the so-called Varshni relation that is given as [84]:

$$E_g = E_0 - \frac{\alpha T^2}{T + \beta},\qquad(2.20)$$

where E_0 is the band gap at $T = 0$ K, and α and β are constants. The variation of the energy gap with temperature is believed to stem from two mechanisms: (1) A shift in the relative position of the conduction and valence bands due to the temperature-induced change of the lattice; (2) The major contribution comes from a shift of the energy gap due to a temperature-dependent electron lattice interaction.

A simple Arrhenius formula, as given below, is often used to describe the tem-

perature induced quench in PL intensity. It is valid when only one simple thermal quench mechanism is involved and no other mechanisms that may transfer or deplete the carriers to or from the state of interest [85, 86]. The Arrhenius formula can be written as [87]:

$$I(T) = \frac{I_0}{1 + A\exp\left(-E_a/k_B T\right)},\tag{2.21}$$

where $I(T)$ represents the integrated PL intensity, E_a is the activation energy of the thermal quenching process, k_B is the Boltzmann constant, I_0 is the integrated intensity at $T = 0$ K, and A is a pre-factor related to the density of non-radiative recombination centers of the quenching process.
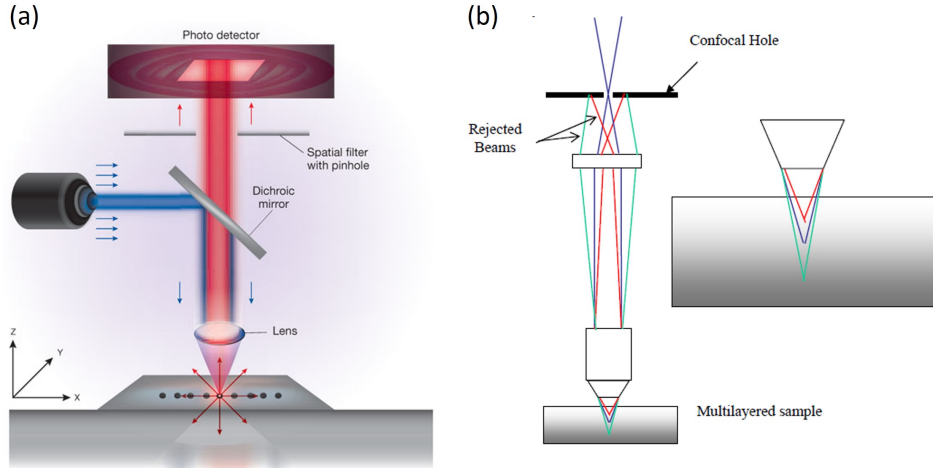
Figure 2.3: Confocal microscope. (a) A simplified view of confocal microscope. (b) The schematic of the confocality. Panel a reproduced from Nwaneshiudu A., et al. [88].

2.3   Experimental Setups

In recent years, the confocal microscope has been widely used as a research instrument to measure Raman and fluorescence in physics, material science, biology, and medicine fields. In comparison with conventional non-confocal microscopy, confocal microscopy is an optical technique to increase the optical resolution and contrast by adding a pinhole at the confocal plane [89], as shown in Figure 2.3a. For a conventional non-confocal microscope, due to diffraction effect the maximum resolution is proportional to the size of its objective, and inversely proportional to the wavelength

of the light being observed. Thus, the microscope is said to be diffraction limited. As a result of diffraction, the pattern observed in the image shows a bright region in the center accompanied by a series of concentric rings of decreasing intensity around it, which is called the Airy disc. The diameter of the Airy disc can be written as:

$$d = \frac{1.22\lambda}{NA},\tag{2.22}$$

where λ is the wavelength of light being observed and NA is numerical aperture of the objective being used.

However, the confocal microscope can increase the resolution beyond the diffraction limit. As shown in Figure 2.3a, the incident light (usually laser) is focused through the objective on the sample examined, and the same objective collects the light coming back from the sample, such as reflected light, Raman or PL. In conventional microscopy, some of the light scatters which could blur or obscure the image. Confocal microscopy overcomes this problem using a small pinhole aperture, allowing the pass of only the light emitting from the desired focal spot. Any light outside the pinhole is blocked (Figure 2.3b). In the very original design of confocal system [90], the pinhole is placed at the confocal plane of microscope system; however, in the case of Figure 2.3a it is placed in a conjugate focal plane as the focal plane on the sample. The light passing through the pinhole is finally collected by a sensitive light detector, such as charge-coupled device (CCD) or photomultiplier tube (PMT).

Therefore, the advantages of using confocal microscopy are as below: (1) the increase of axial resolution as well as lateral resolution; (2) the improvement of image contrast; (3) capability to reconstruct 3D images. Given all these advantages of confocal microscope, the works related to optical spectroscopies in this dissertation were mostly carried out with a confocal system – Horiba LabRAM HR800. With the confocal configuration, the spatial resolution can be achieved beyond the diffraction
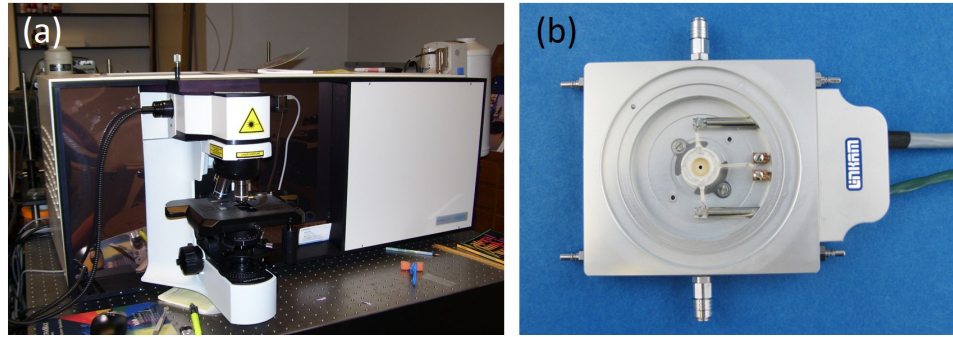
Figure 2.4: Experimental setups. The views of (a) Horiba LabRAM HR800 micro-Raman/PL spectroscope, and (b) Linkam TS1500 heating stage.

limit. Meanwhile, with a long focal length of spectrometer (800 cm) allows the tool to achieve a high spectral resolution. For instance, with a grating of 1200 grove/mm and a CCD of 2048-pixel array, the spectral resolution of the system is $\sim$0.5 cm^{-1} when 532 nm laser is used. With a 2400 grove/mm grating, the resolution can be even better. Another advantage of this tool is the ability of scanning the sample with a precisely-controlled sample stage, which allows us to perform a mapping of Raman or PL at a designated area to examine the variation of a specific optical characteristic. Besides this confocal system, all the temperature-dependent measurements were performed with a heating system – Linkam TS1500. This system has a temperature control accuracy of less than 1 °C, and allows us to purge gases into the chamber or even to create a vacuum environment. In Figure 2.4 shows the appearance of these two instruments.

CHAPTER 3: TEMPERATURE DEPENDENCE OF RAMAN SCATTERING IN
GRAPHENE

3.1   Fabrication and Characterization of Graphene

3.1.1   Fabrication of Graphene

Graphene, as a single layer of graphite, can be fabricated by either mechanical exfoliation or chemical vapor deposition. For mechanical exfoliation, the graphene is usually transferred to silicon substrate coated with a 300 nm SiO_2 thermal layer, with which graphene can be observed under optical microscope [10, 91]. For CVD growth, the graphene films are typically synthesized on Cu or Ni, and then transferred to SiO_2/Si substrate. During the transferring process, scotch tape is utilized for ME graphene and PMMA for CVD grown films, thus it is quite possible that polymer residues from the tape and PMMA will be remained on top of the graphene films, which are difficult to be fully removed either by solvents like methanol or by annealing. Figure 3.1 shows the optical images of two graphene samples fabricated by these two methods. Especially for the CVD sample, polymer residues can be clearly observed. Besides the two samples fabricated with these two methods, the optical image of graphite, which is used for exfoliation and as reference, is also shown in Figure 3.1.

3.1.2   Characterization of Graphene Samples

AFM is perhaps in general the most reliable method to identity single- and few-layer 2D materials, but for graphene it has limitations. The thickness of graphene has been theoretically predicted to be of $\sim$0.35 nm. However, due to the chemical contrast between graphene and the substrate, which results in a chemical thickness of 0.5–1 nm (much bigger than the interlayer graphite spacing), the identification of single layer graphene is a great challenge with AFM. Therefore, seeking for a
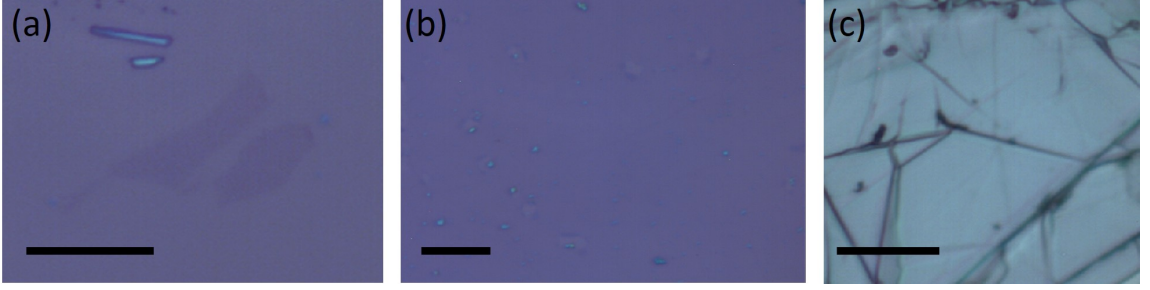
Figure 3.1: Optical images of graphene samples and graphite. (a) ME graphene on SiO$_2$/Si by the scotch tape technique. (b) CVD-grown graphene transferred onto SiO$_2$/Si by PMMA. (c) Graphite. The scale bar is 10 µm.

more reliable method to determine the layer number of exfoliate graphene layers is necessary for the widespread utilization of this material. As it has been demonstrated, the graphene's electronic structure can be uniquely reflected in its Raman spectrum, which reveals the changes in the electronic band structure for single layer, bilayers, and few layers [92]. Therefore, Raman spectroscopy can be used as fingerprints to nondestructively identify the thickness (layer number) of graphene layers.

Bulk graphite belongs to the space group of $P63/mmc$ (D_{6h}^4); its isogonal point group is D_{6h}. The irreducible representations of graphite vibration modes at Brillouin zone center are: $\Gamma^{graphite} = 2A_{2u} + 2B_{2g} + 2E_{1u} + 2E_{2g}$ [93,94]. Among them, there are two Raman active vibrations at the Γ point of the Brillouin zone: $E_{2g(2)} \approx 1582$ cm^{-1} and $E_{2g(1)} \approx 42$ cm^{-1}. For single graphene layer, there are two atoms per unit cell, giving six normal modes for the zone center. The irreducible representations for the zone-center modes of graphene are: $\Gamma^{graphite} = A_{2u} + B_{2g} + E_{1u} + E_{2g}$ [95]. The A_{2u} mode represents translation perpendicular to the graphene plane and the E_{1u} the translation in the graphene plane. The B_{2g} mode is an inactive optical phonon mode of which the carbon atoms vibrate perpendicularly to the graphene plane. The E_{2g} mode is doubly degenerate in-plane optical vibration, which is the only Raman active mode for graphene at the zone center. The frequency of the E_{2g} mode is expected at ~1587 cm^{-1} [92]. In the literature, the graphite $E_{2g(2)}$ mode is usually assigned

as the G peak, which is carried over to single or few-layers graphene. If the number of layers increases from graphene to graphite, the peak position of G band tends to decrease from 1587 cm^{-1} to 1581.5 cm^{-1} while its intensity increases linearly from monolayer to 20-layers [96].

If graphite sample contains disorder in its crystalline structure, a new Raman line appears at ~1370 cm^{-1}. It is assigned as disorder-induced mode, or D-mode. Conventionally, this mode stands for the vibration related to the K point of graphite Brillouin zone. Its frequency is also close to that of the Γ point optical phonon in diamond. In the second-order spectrum of graphite there is one main feature at ~2700 cm^{-1}, historically denoted as D^* or G' or $2D$ mode. The frequency of this mode is very close to twice that of D mode. The notation of $2D$ is used in this dissertation. The frequency of the D mode shifts to higher frequency with increasing excitation energy, and the $2D$ band shifts twice as much as the D band, confirming the $2D$ mode is an overtone of the D mode [93, 97]. This is due to double resonance process that links the phonon wave vectors to the electronic band structure. This process predicts that graphene has a single $2D$ peak. As number of layers increases, $2D$ band becomes more complicate, showing more features. Besides G, D and $2D$ peaks, there are also vibrational modes at ~2450 cm^{-1} and ~3248 cm^{-1}.

Figure 3.2 shows the Raman spectra of the three samples shown in Figure 3.1, measured by 532 nm excitation laser. All the major peaks discussed above are observed in these spectra. The D peak, 1345 cm^{-1}, is only seen in CVD-grown sample, because it contains more defects which are from both growth and transfer processes. Besides D peak, a peak at 1620 cm^{-1} is observed which is denoted as D' [98]. In CVD-grown sample, both D and D' bands are activated by a single-phonon inter-valley and intravalley scattering process through defects, respectively. The defects provide the missing momentum to satisfy momentum conservation in the Raman s-cattering [99, 100]. No D-band feature is observed in both mechanically exfoliated

graphene and graphite, indicating they are of high quality or nearly defect-free. The two most intense features are the G peak and $2D$ peak. The G peak is due to the doubly degenerate zone center E_{2g} mode; whereas, the $2D$ band is the second order of zone-boundary phonons near K point, having the frequency of twice of the D band. For G peaks, the frequency is measured to be 1587.6 cm^{-1} for CVD-grown graphene, 1584.5 cm^{-1} for ME graphene, and 1581.5 cm^{-1} for graphite. The frequency of G band increases as the thickness decreases. For graphene the peak position of G band is very sensitive to doping effect [101]. Since the CVD-grown graphene has more ad-sorbed polymeric residues on top of the film than the ME sample, more doping could be introduced to the graphene layer causing a blueshift of G band. The full width at half maximum (FWHM) of the three samples are 18.8 cm^{-1} (CVD), 11.2 cm^{-1} (ME), and 15.0 cm^{-1} (graphite), respectively. The larger FWHM of CVD-grown graphene is due to its lower crystalline quality, such as defects and non-uniformity, which can significantly affect the crystal structure.
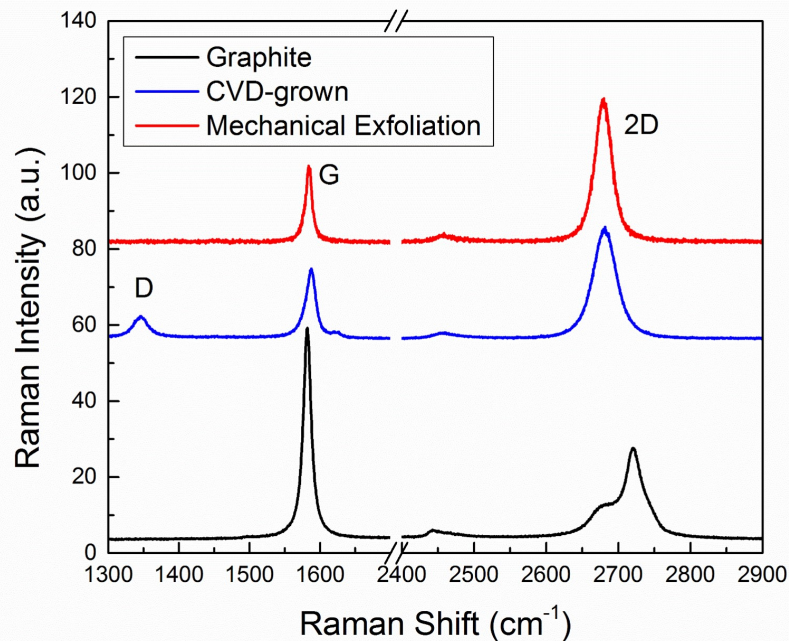
Figure 3.2: The Raman spectra of graphene and graphite.

As of $2D$ peak, both CVD-grown and ME graphene samples exhibit single symmetric peak at 2680.7 and 2679.6 cm^{-1}, respectively. However, graphite shows a clear doublet feature. The $2D$ peak in graphene is due to two phonons with opposite momentum in the highest optical branch near the K point, which is called double resonance (DR) process. The DR process links the phonon wave vectors to the electronic band structure. Within DR, Raman scattering is a process of fourth order involving four virtual transitions (as shown in Figure 3.3) [92]: (1) a laser induced excitation of an electron-hole pair indicated as a→b vertical transition; (2) electron-phonon scattering with an exchanged momentum q close to K (b→c); (3) electron-phonon scattering with an exchanged momentum $-q$ (c→b); (4) electron-hole recombination (b→a). Thus, the DR condition is reached while the energy is conserved in these transitions. In single layer graphene only a single peak is observed that is corresponding to the phonon satisfying DR conditions with momentum $q > K$, along the Γ–K–M direction, whereas the other two possible DR phonons, with $q < K$ and $q \sim K$, give a much smaller contribution to the Raman intensity. As the layer number increases to 2 or more, more components within the $2D$ peak appear, which in principle is attributed to the splitting of the electronic bands rather than the splitting of the phonon branches. Because the splitting of the phonon branches theoretically calculated is much smaller than experimentally observed splitting of $2D$ Raman peak [92]. Thus, the doublet feature of $2D$ band is solely due to the splitting of electronic band structure. By fitting the $2D$ band of graphite with Lorentzian function, the frequencies of the two components, denoted as $2D_1$ and $2D_2$, are 2677.1 and 2721.8 cm^{-1}, respectively, and the splitting is 34.7 cm^{-1}.

Figures 3.4 and 3.5 show Raman mapping results of both ME and CVD-grown graphene samples, respectively. For ME graphene sample, both G and D intensity maps (Figure 3.4a,d) exhibit uniform distribution, except for the edge where the measured area of graphene is smaller than laser spot. The peak position variation of

both bands is less than 1 cm^{-1}, so is the FWHM variation. All these data indicate that the ME graphene has an extremely high quality. It is worth noting that at the edge D peak is observed because the edge of the graphene flake is considered as defective. The uniformity of the mapping results of the ME sample suggests that the sample is free from the possible chemical contamination of the transfer process. Whereas, the mapping results of CVD-grown graphene is shown in Figure 3.5, revealing non-uniform distributions of peak position, intensity and FWHM. The maximum variations of G and $2D$ peak positions are 5.7 and 11.8 cm^{-1}, respectively. The extraordinarily large variation of the CVD-grown graphene is attributed to the defects in the film as well as the rippling introduced during transfer, showing a clear D peak feature as indicated in Figure 3.2.
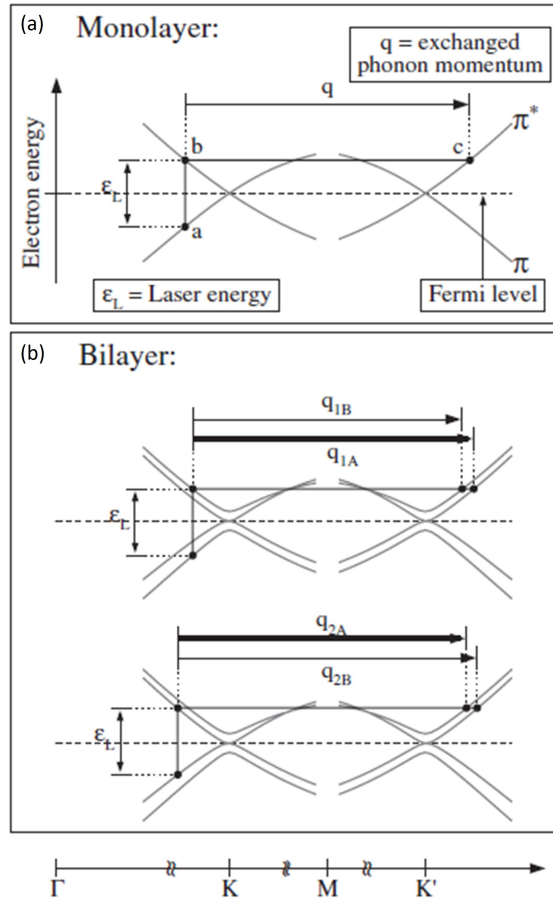
Figure 3.3: Double resonance for the $2D$ peak in (a) monolayer and (b) bilayer. Reproduced from Ferrari A. C. et al. [92].
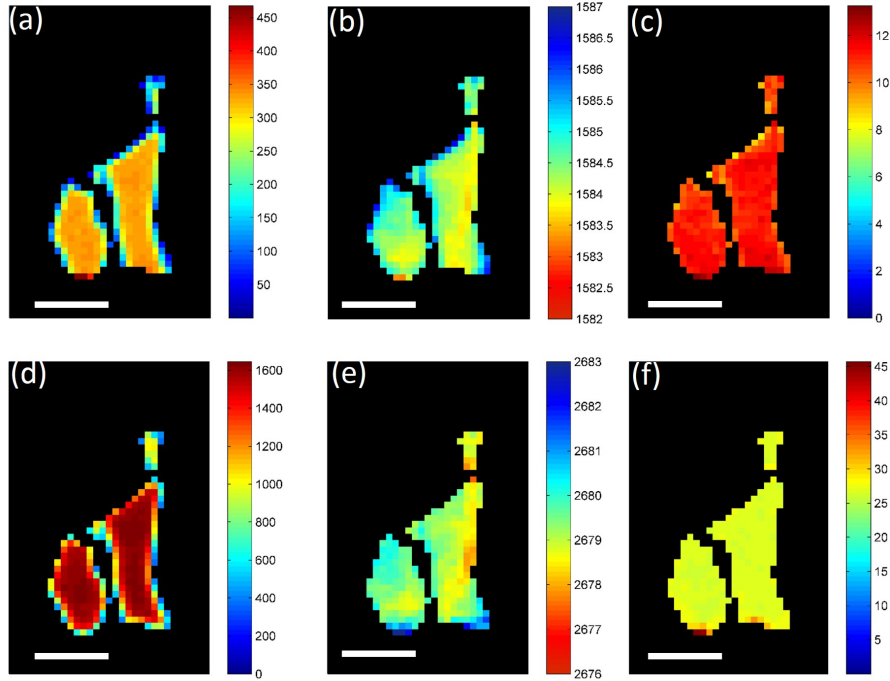
Figure 3.4: G and $2D$ band Raman mapping results of ME graphene sample. (a) and (d) The intensity maps of (a) G band and (d) $2D$ band. (b) and (e) The maps of Raman peak frequencies of (b) G band and (e) $2D$ band. (c) and (f) The maps of FWHM of (c) G band and (f) $2D$ band.

3.2   Temperature Dependent Measurements and Results

Like graphite, graphene is chemically inert in most case as well as good thermal stability up to several hundred °C without severe degradation. However, thermal treatment can cause graphene non-negligible changes in its material properties. As the annealing temperature goes up, graphene films that are held by SiO_2/Si substrate, as an example, undergoes in-plane compression and rippling due to conformal adhesion or thermal expansion difference between graphene and substrate. The annealing process can significantly change the structural and electronic properties of graphene, resulting in the charge carrier mobility of annealed graphene devices much lower than that of pristine devices [102]. Usually, the graphene samples are prepared by tapes or CVD. The polymeric adhesive residues are difficult to be removed completely even by annealing at high temperature.
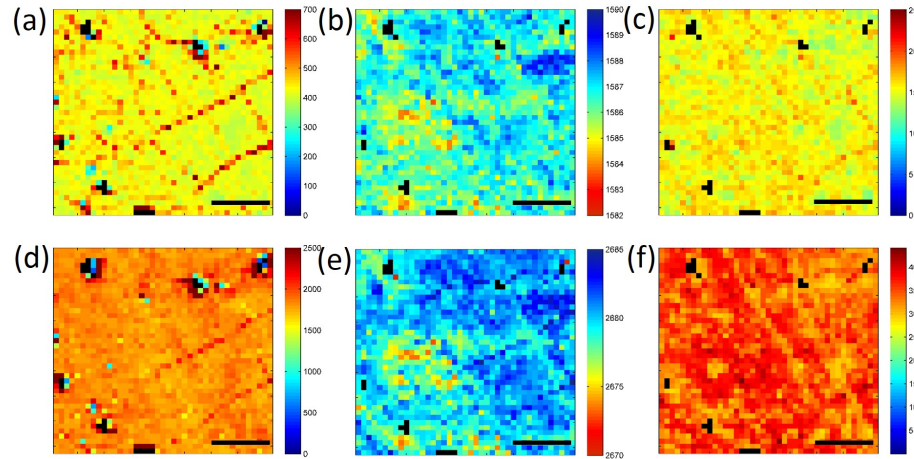
Figure 3.5: G and $2D$ band Raman mapping results of CVD-grown graphene sample. (a) and (d) The intensity maps of (a) G band and (d) $2D$ band. (b) and (e) The maps of Raman peak frequencies of (b) G band and (e) $2D$ band. (c) and (f) The maps of FWHM of (c) G band and (f) $2D$ band.

There were a few temperature dependent Raman studies on graphene with the intent to obtain the temperature coefficients of the graphene Raman modes [103, 104]. These studies were performed in a temperature region (typically below 200 °C) where the Raman frequency shifts appeared to be more or less linear. We have instead to investigate the temperature effects to much higher temperatures, to the limit of the material thermal degradation occurs. Raman spectroscopy in a broader temperature range can help to understand the influence of the residues and the changing 2D material/substrate bonding on the properties of graphene.

Temperature dependent Raman of all the three samples is performed in the range from room temperature to 400 °C for graphene samples and to 500 °C for graphite in a nitrogen (N_2) purged heating chamber. The laser excitation line is 532 nm with the power of $\sim$1 mW. The temperature dependences of both G and $2D$ band frequencies are shown in Figure 3.6. For graphite, since $2D$ peak contains two components, Lorentzian fitting has been applied to extract the individual temperature dependence of $2D_1$ and $2D_2$. Figure 3.7 shows the representative spectra of graphene samples and graphite at different temperatures.
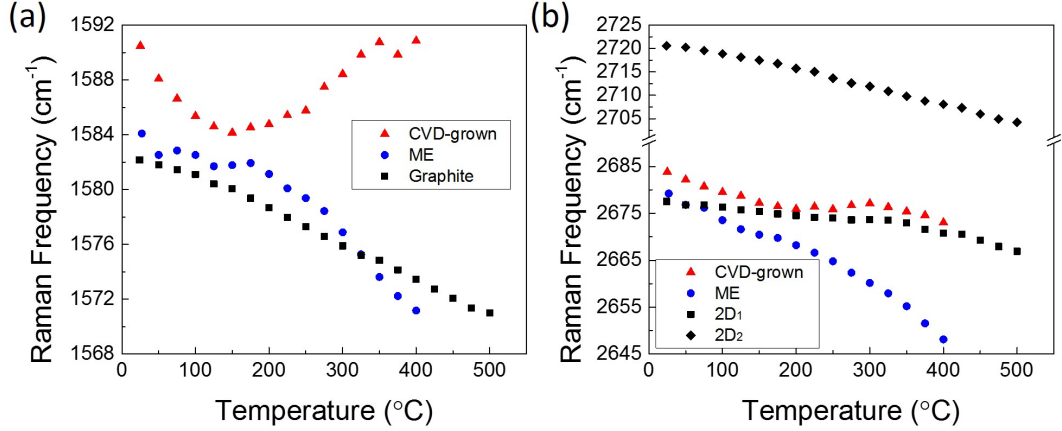
Figure 3.6: Temperature dependence of Raman frequencies of (a) G and (b) $2D$ bands for the two graphene samples and graphite.

Graphite, as the reference, exhibits more linear temperature dependence than the other two graphene samples. Empirically, the temperature dependence of Raman shift is often described as:

$$\omega(T) = \omega_0 + \chi\Delta T, \tag{3.1}$$

where ω_0 is the frequency at RT, χ is the temperature coefficient, and ΔT is the temperature change relative to RT. Fitting the dependence with Eq.(3.1), the temperature coefficients are -0.025, -0.020, and -0.036 cm^{-1}/K for G, $2D_1$, and $2D_2$ bands, respectively. However, when temperature goes beyond $100\,^\circ$C nonlinear effect occurs to both G and $2D$ bands, which is due to the anharmonic effect of phonons as discussed in Eq.(2.14). For ME graphene sample, the temperature dependence starts to become nonlinear when temperature is $> 100\,^\circ$C for both modes. The G band, which is in-plane vibration, is very susceptible to the surrounding environment, particularly the substrate. As a single-layer film, the morphology can be modified when the temperature increases, because the differential thermal expansion of graphene with respect to the substrate. Graphene has a negative in-plane TEC of $(-8.0\pm0.7)\times10^{-6}$ K^{-1} [22], while SiO$_2$ has a small positive TEC of $\sim0.5\times10^{-6}$ K^{-1}. Thus, if there is significant bonding between graphene and substrate, with increasing temperature graphene film
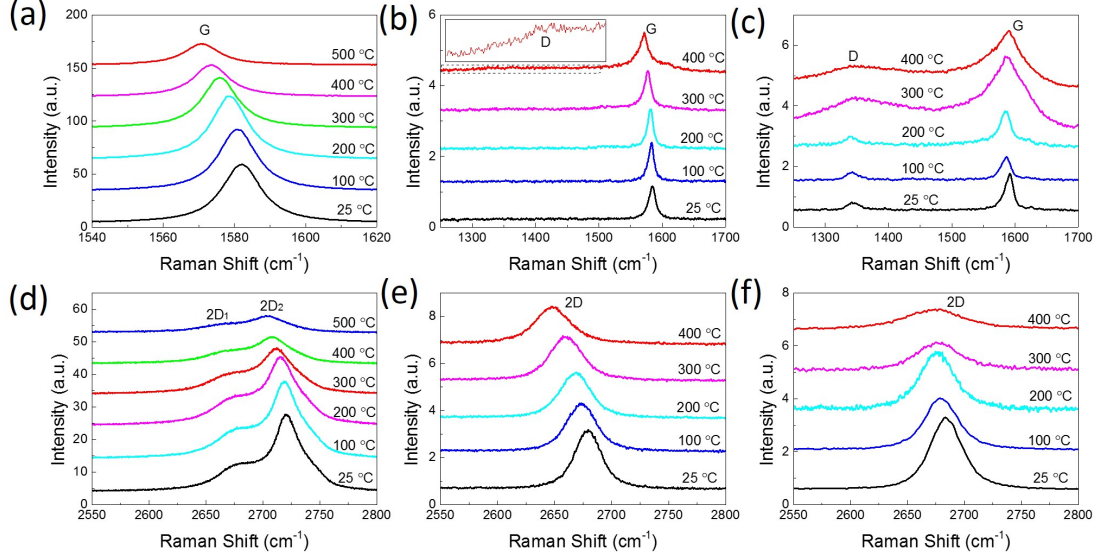
Figure 3.7: The representative Raman spectra at different temperatures for the two graphene samples and graphite. (a)-(c) G band spectra. (d)-(f) $2D$ band spectra.

will undergo a tensile strain, as graphene tends to shrink while the substrate expand. As temperature reaches $100\,°C$, the strain reaches a critical point that the film slips on the surface of substrate and release the strain, resulting in a kink at $\sim175\,°C$ in G-band temperature dependent curve. After the rearrangement of the graphene film, the temperature dependence tends to be linear again, but with a larger slope due to tensile strain. The bonding likely becomes stronger after the relaxation, thus, does not show another apparent kink. Similar nonlinear behavior is observed in $2D$-band temperature dependence, showing a smaller kink at $\sim175\,°C$. Starting from the temperature of $300\,°C$, a peak appears at ~1350 cm^{-1} which is believed to be D peak, as shown in Figure 3.7b. In Figure 3.8a-b, the spectra before and after temperature-dependent Raman measurements are shown. The peak position of G band exhibits a blueshift from 1584.1 to 1588.7 cm^{-1}, while that of $2D$ band shows almost no shift after the annealing process. The blueshift of G band is due to the compressive strain originating from the difference in TEC between graphene and substrate. The FWHM broadens from 13.1 to 19.1 cm^{-1} for G band, and from 25.4 to 31.4 cm^{-1} for $2D$ band, respectively. Besides, the appearance of the broad D peak at RT after annealing indi-

cates the increase of doping or defect level in the film, which might not originate from graphene itself but amorphous carbon generated from residual hydrocarbons of the tape at high temperature. This doping effect coupled with the morphology change of graphene film is the origin of the broadening and shift of both G and $2D$ bands after annealing.
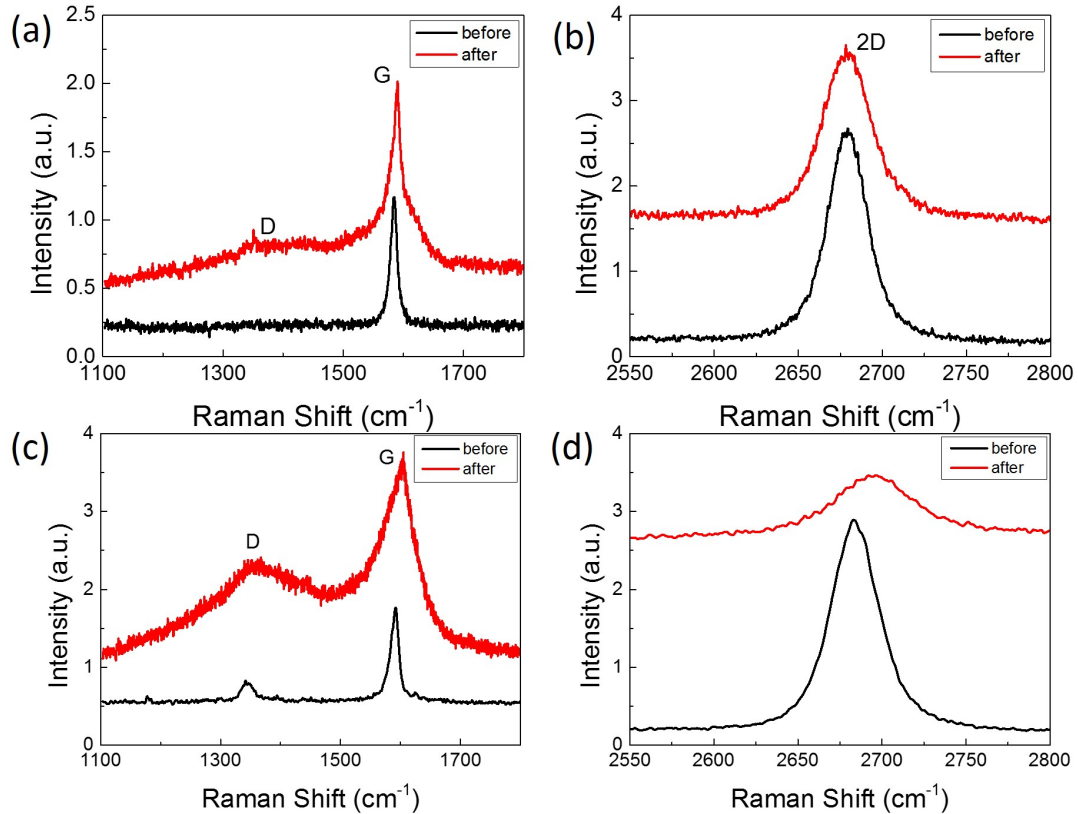
Figure 3.8: The spectra before and after temperature-dependent Raman measurement. (a)-(b) The Raman spectra of (a) G and (b) $2D$ bands before and after the measurements for the ME graphene sample. (c)-(d) The Raman spectra of (c) G and (d) $2D$ bands before and after the measurements for the CVD graphene sample.

For G band, the results of CVD-grown graphene sample show a super nonlinear temperature dependence, with a steeper redshift in Raman frequency than the graphite as temperature elevated to $150\,°C$ and a strong bowing afterward. As discussed in ME graphene sample, the slip of graphene occurs when the strain reaches a critical point, which may cause the G peak to blueshift. However, since the density

of polymer residues is higher in CVD-grown film that that in ME film, the D and G bands are extremely broad at high temperatures (Figure 3.7), which is due to doping caused by the residual hydrocarbons. Meanwhile, the doping from residues can also cause the blueshift of G band. With increasing temperature, the more decomposition of the residues is, the more doping would be introduced to the film, resulting in more blueshift in G band frequency. After the sample is cooled down to room temperature, the broad D and G peaks are still seen, as shown in Figure 3.8. As for $2D$ band, the temperature dependence shows an 'S'-shaped curve, similar to that of ME graphene sample. The $2D$ band of CVD-grown graphene does not show as significant shift as that of ME graphene at elevated temperatures. Additionally, as the temperature rises, the changes of film morphology such as ripples will provide additional scattering of the near-K-phonons associated with $2D$ band, arising from the anharmonic phonon-phonon interaction [105]. Comparing the spectra of $2D$ band before and after annealing, the peak position shifts from 2683.9 to 2695.5 cm^{-1} while the FWHM increases from 30.7 to 57.3 cm^{-1}, which is also associated with the increasing density of doping or defects in the film.

3.3   Conclusions

In conclusion, temperature-dependent Raman spectroscopy has been applied to investigate the vibrational and thermal properties of graphene, prepared by either mechanical exfoliation or CVD, which is held by SiO$_2$/Si substrates. Graphite as the reference shows the redshift of both G and $2D$ peaks. However, the temperature dependence of graphene samples exhibits nonlinear behavior. For the CVD-grown graphene, both G and D peaks become very broad after annealing, which are attributed to the hydrocarbonization of the polymeric residues mainly from the transfer process. The annealing process cause the residues to form amorphous carbon on the surface of graphene, resulting in the change of electronic structure, and hence the scattering process of phonons. Furthermore, as the temperature increases, the

morphologic change of graphene, which arises from the difference in TEC between graphene and substrate, is another important contribution to the shift of Raman frequency. As for ME graphene, since much less residues are introduced to the film, the extent of broadening of G and D peaks is smaller than that of CVD-grown graphene. Whereas, the change of film morphology still plays a significant role in the shift of G and $2D$ peaks. Therefore, though annealing provides an easy way to remove polymer residues on graphene, the leftover remains can significantly modify the electronic structure and further affect the performance of graphene-based devices. These observations suggest that the development of a polymer-free transfer technique is desirable, and the protection of graphene from further contamination after fabrication is necessary.

CHAPTER 4: TEMPERATURE DEPENDENCE OF RAMAN SCATTERING IN
MONOLAYER AND BILAYER MOS$_2$

4.1   Fabrication and Characterization of MoS$_2$ Samples

4.1.1   Sample Fabrication

MoS$_2$ samples investigated have been prepared by two methods: mechanical exfoliation (from a purchased single crystal sample from SPI Supplies) and chemical vapor deposition (provided by Prof. Linyou Cao's group at NCSU [106]). The 1L MoS$_2$ flake was mechanically exfoliated from nature crystalline bulk MoS$_2$ and transferred onto a silicon wafer covered by a 300-nm-thick thermal oxide (SiO$_2$) layer (Sample 1L-ME-SiO$_2$). The CVD-grown 1L and 2L samples were prepared on two types of substrates, SiO$_2$/Si and sapphire labeled as, respectively, 1L-CVD-SiO$_2$, 1L-CVD-Sa, 2L-CVD-SiO$_2$, and 2L-CVD-Sa. Originally the MoS$_2$ films were grown on sapphire wafers, and then transferred to SiO$_2$/Si wafers by scotch tape. A bulk MoS$_2$ sample was placed on SiO$_2$/Si substrate as reference. Figure 4.1 shows the optical images of all these samples.

4.1.2   Characterization of MoS$_2$ Samples

Figure 4.2 shows an AFM image of the sample 1L-ME-SiO$_2$, confirming the monolayer MoS$_2$ thickness to be $\sim$0.7 nm. Besides AFM to determine the thickness or layer number of MoS$_2$ thin film, Raman spectroscopy is another powerful and nondestructive technique to not only determine the layer number by the Raman frequency of major MoS$_2$ Raman modes, but also to investigate structural and electronic properties of MoS$_2$.

A single-layer MoS$_2$ is formed by the arrangement of a triangular or simple hexagonal plane of Mo atoms sandwiched between two triangular layers of S atoms in
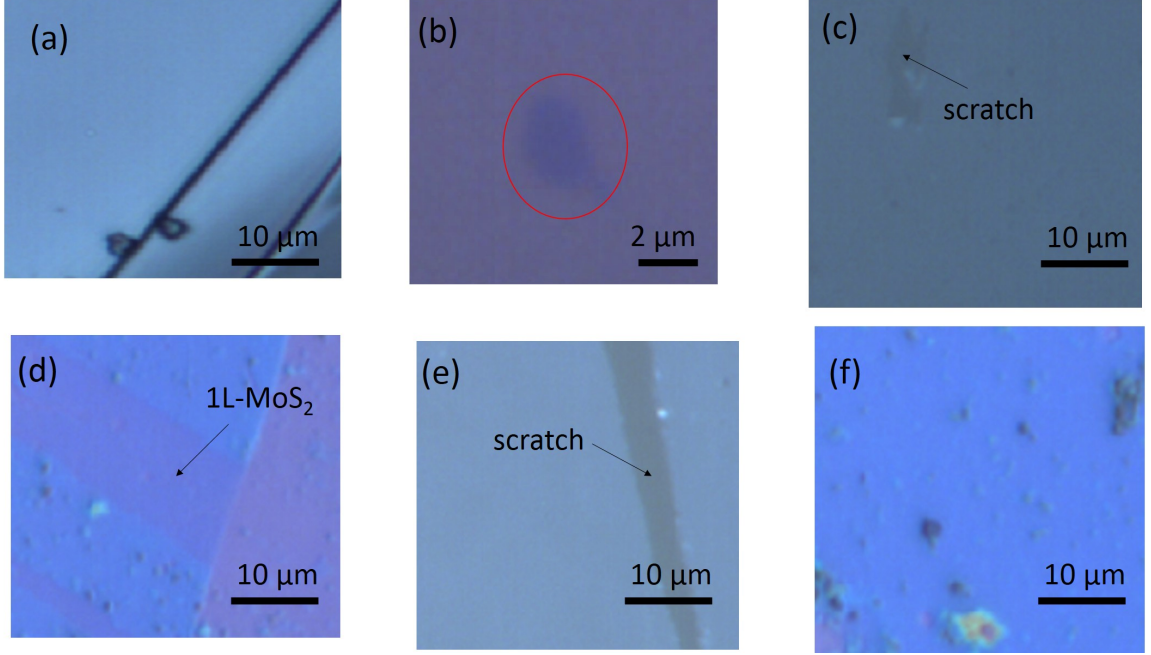
Figure 4.1: The optical images of MoS$_2$ samples. (a) Bulk MoS$_2$. (b) ME monolayer MoS$_2$ on SiO$_2$/Si – 1L-ME-SiO$_2$. (c) CVD-grown monolayer MoS$_2$ on sapphire – 1L-CVD-Sa. (d) CVD-grown monolayer MoS$_2$ transferred onto SiO$_2$/Si – 1L-CVD-SiO$_2$. (e) CVD-grown bilayer MoS$_2$ on sapphire – 2L-CVD-Sa. (f) CVD-grown bilayer MoS$_2$ transferred onto SiO$_2$/Si – 2L-CVD-SiO$_2$. Polymeric residues can be clearly seen.

a triangular prismatic fashion (Figure 4.3a). Bulk MoS$_2$ is a periodically stacked S-Mo-S layers through vdW force. The space group of single layer MoS$_2$ is $P6m2$ (point group D_{3h}), and the four first-order Raman active modes at the center of Brillouin zone are 32 cm^{-1} (E_{2g}^2), 286 cm^{-1} (E_{1g}), 383 cm^{-1} (E_{2g}^1), and 408 cm^{-1} (A_{1g}), as illustrated in Figure 4.3b [43, 46]. The E_{2g}^2 mode arises from the relative motion between two MoS$_2$ layers, which will vanish in the single layer sample. The E_{2g}^1 mode is forbidden in back-scattering measurement on the basal plane perpendicular to the c axis. The E_{2g}^1 mode is attributed to the in-plane relative motion between the two S atoms and the Mo atom, whereas the A_{1g} mode the out-of-plane vibration of two S atoms in opposite directions. Strictly speaking, the two active Raman modes E_{2g}^1 and A_{1g} (in D_{6h} for bulk MoS$_2$) should be assigned as E' and A_1' in the monolayer MoS$_2$ (in D_{3h}) [107, 108]. However, to see the evolution from the bulk to single-layer [46, 109], the two modes are simply labelled as E_{2g}^1 and A_{1g} for all cases, as commonly done in

the literature.
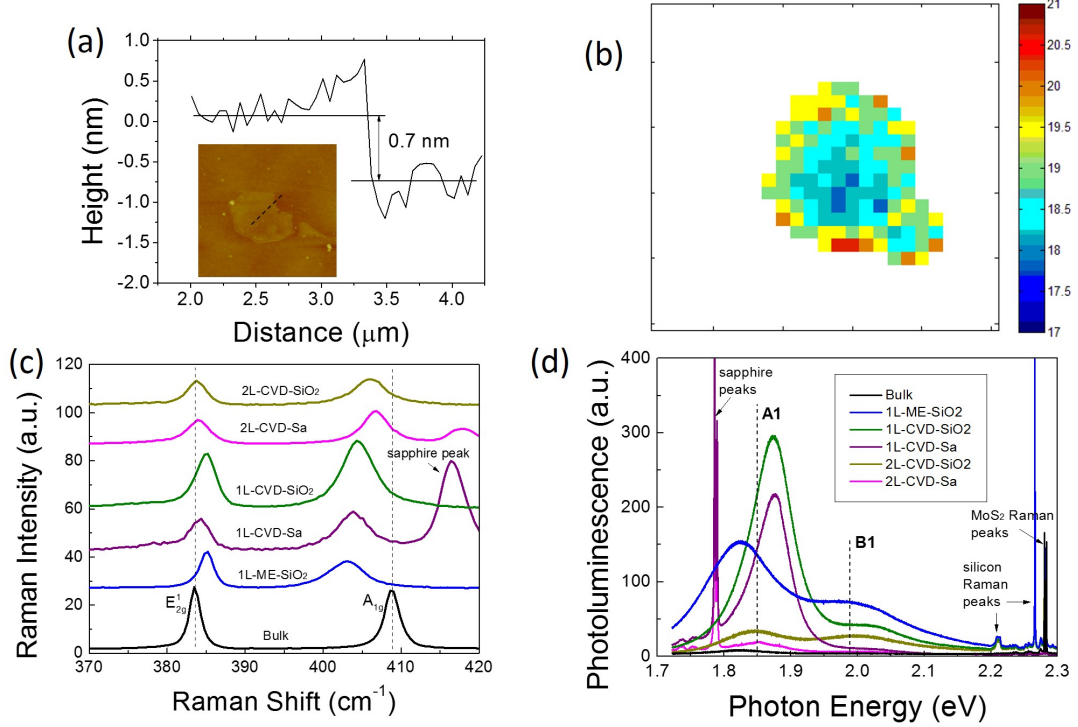
Figure 4.2: The characterizations of all the six MoS$_2$ samples. (a) AFM image of 1L-ME-SiO$_2$ showing the thickness of the film to be 0.7 nm. (b) The map of frequency difference between E_{2g}^1 and A_{1g} modes. (c)-(d) (c) Raman and (d) PL spectra of all the six samples.

The room temperature Raman spectra of all the six samples in Figure 4.1 are shown in Figure 4.2c, measured with 532 nm laser at $\sim$1 mW using the 100$\times$ lens. The Raman frequency difference ($\Delta\omega$) between the E_{2g}^1 and A_{1g} modes can be correlated with the layer number [109]. For monolayer MoS$_2$, $\Delta\omega = 19$ cm^{-1}, for bilayer 22 cm^{-1}, and for the bulk 26 cm^{-1} [109, 110]. $\Delta\omega$ is a better indicator for the layer number than the absolute ω value of each peak that is more sensitive to the strain. Theoretically, when the layer number increases, the interlayer van der Waals force in MoS$_2$ suppresses atom vibration, leading to higher force constants. Therefore, both E_{2g}^1 and A_{1g} modes are supposed to stiffen (blueshift) [111, 112]. The observed blueshift of A_{1g} mode with increasing layer number is consistent with the theoretical prediction. However, it is also found that the frequency of E_{2g}^1 peak decreases as the
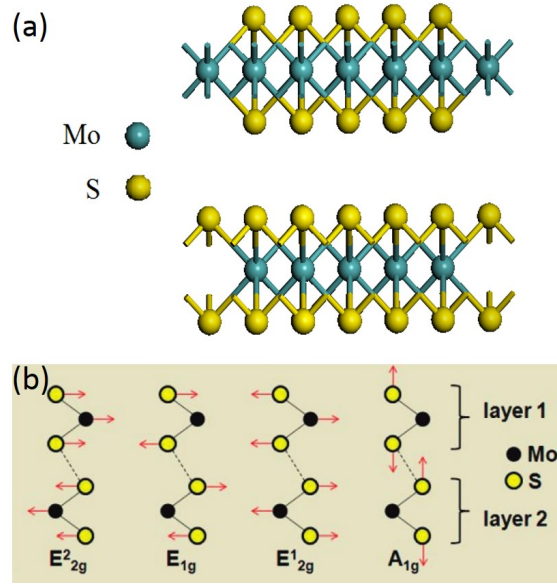
Figure 4.3: MoS$_2$ structure and Raman active modes. (a) Schematic model of MoS$_2$ structure. (b) Atomic displacements of the four Raman-active modes for the bulk MoS$_2$.

layer number increases, suggesting that interlayer vdW force plays a minor role while stacking-induced structure changes or long-range Coulombic interlayer interactions in multilayer MoS$_2$ may dominate the change of atomic vibration. Figure 4.2b shows the spatial variation of the frequency difference ($\Delta\omega$) of 1L-ME-SiO$_2$, and it is all found to be less than 20 cm^{-1}, indicating the film is indeed monolayer.

As is known, when the layer number of MoS$_2$ goes to monolayer, the band structure of MoS$_2$ transforms from indirect to direct [44]. It has also been reported that the PL of MoS$_2$ has two peaks that correspond to A (1.85 eV) and B (1.98 eV) exciton transitions, split by the spin-orbit coupling of the valence band. PL spectra of all these samples are shown in Figure 4.2d. For sample 1L-ME-SiO$_2$, the A and B transitions are, respectively, at 1.82 eV and 1.98 eV, for single-layer CVD samples 1.87 eV and 2.0 eV, and for bilayer CVD samples 1.85 eV and 1.99 eV. The precise excitonic bandgap value is in fact not know so far. The accepted values are approximately within the range of 1.8-1.9 eV [15, 44, 109, 113, 114] This situation is unfortunately general for monolayer or few layers TMDs. The variation of the PL peak positions of

MoS$_2$ samples could be due to the interaction between the film and the substrate and possibly impurities and doping in the films. For MoS$_2$ films on SiO$_2$/Si substrate, it is generally believed that there is charge transfer between MoS$_2$ and substrate to form trions which has a lower energy than free excitons [115]. This could be another reason that 1L-ME-SiO$_2$ exhibits smaller energy of A-exciton emission. In general, the 1L MoS$_2$ samples show the strongest PL signal, while the bulk MoS$_2$ negligible, as expected due to the electronic band structure change.

4.2   Temperature Dependence of Raman Scattering

4.2.1   Temperature Dependent Raman Spectroscopy

The temperature dependences of both E_{2g}^1 and A_{1g} peak positions were performed in the range from room temperature (25 °C) to 500 °C, shown in Figure 4.4a-d. The upper temperature range in this work is substantially higher than those in the previous works < 250 °C. The results of bulk MoS$_2$ are used as a reference. Empirically, the temperature dependence of Raman shift can be described by:

$$\omega(\Delta T) = \omega_0 + \chi_1 \Delta T + \chi_2 (\Delta T)^2 + \chi_3 (\Delta T)^3, \tag{4.1}$$

where ω_0 is the frequency at room temperature, ΔT is the temperature change relative to room temperature, and χ_1 is the first-order temperature coefficient. The second (χ_2), third (χ_3) or higher order temperature effects are usually assumed to be small in the literature. In reality, the nonlinear effects are found to be quite significant for 1L or 2L MoS$_2$ even in a temperature range where the linear dependence might be expected to be adequate, for instance, below 200 °C, depending on the substrate. Even for bulk MoS$_2$, the nonlinearity occurs at around 200 °C for both E_{2g}^1 and A_{1g}, though rather weak, but nevertheless evident in our data.

It is perhaps reasonable to assume that the temperature shift for a free standing few-layer MoS$_2$ should be rather close to that of the bulk material, despite the dif-

ference in the absolute position. Therefore, to show more clearly the substrate effect, we can take the temperature shifts of the bulk sample as references. Figure 4.4e-h plot the difference in the Raman frequency shifts between the thin film sample and the bulk, $\delta\omega(\Delta T) = |\omega(\Delta T) - \omega_0|_{\text{thin film}} - |\omega(\Delta T) - \omega_0|_{\text{bulk}}$, for E_{2g}^1 and A_{1g} and for 1L and 2L samples. Below we discuss separately E_{2g}^1 and A_{1g} to examine the effects of two types of substrates.

(1) E_{2g}^1: For both the 1L and 2L samples, as shown in Figure 4.4a,c, and Figure 4.4e,g, the E_{2g}^1 mode exhibits relatively weak nonlinearity or in general appears to be close to the temperature dependences of the bulk sample. The temperature dependences of the deviations from the bulk mode are qualitatively similar for the same type of substrate: 1L-CVD-Sa and 2L-CVD-Sa vs. 1L-CVD-SiO$_2$ and 2L-CVD-SiO$_2$, which is more apparent in Figure 4.4e,g, due to subtle difference in the film-substrate coupling (to be discussed later). The deviations of 1L-ME-SiO$_2$ are somewhat different from the other samples, as shown in Figure 4.4e.

(2) A_{1g}: For both 1L-ME-SiO$_2$ and 1L-CVD-SiO$_2$, as shown in Figure 4.4b,f, the temperature dependence of A_{1g} mode is drastically different from that of the bulk, showing strong nonlinearity starting at temperature near $100\,^{\circ}\text{C}$ and an overall 'S' shape dependence. The Raman spectra of 1L-ME-SiO$_2$ at a few representative temperatures are shown in Figure 4.5. The FWHM of A_{1g} mode is 5.7 cm^{-1} at room temperature, increasing to a maximum of 10.3 cm^{-1} at around $125\,^{\circ}\text{C}$, then it decreases to 6.3 cm^{-1} when the temperature reaches $500\,^{\circ}\text{C}$, whereas the FWHM of E_{2g}^1 mode increases from 2.2 cm^{-1} at room temperature monotonically to 4.8 cm^{-1} at $500\,^{\circ}\text{C}$. However, 1L-CVD-Sa shows only small deviation from the bulk dependence, with an average slope of -0.0159 cm^{-1}/K by using linear fitting, up to $500\,^{\circ}\text{C}$, then an obvious change occurs, becoming nearly flat with a slope of -0.0027 cm^{-1}/K. As for the 2L samples, Figure 4.4d,h, similar to 1L-CVD-SiO$_2$, 2L-CVD-SiO$_2$ exhibits more significant deviation from the bulk sample than 2L-CVD-Sa when temperature

$< 400\,^{\circ}$C. For 2L-CVD-Sa, the slope changes significantly when $T > 400\,^{\circ}$C from -0.0162 cm^{-1}/K to -0.0102 cm^{-1}/K. Again, one may notice that the temperature dependences of the deviations from the bulk mode are qualitatively similar for the same type of substrate: 1L-CVD-Sa and 2L-CVD-Sa vs. 1L-CVD-SiO$_2$ and 2L-CVD-SiO$_2$, which is more apparent in Figure 4.4f,h.

Visually from Figure 4.4a-d, the A_{1g} mode shows more nonlinearity than the E_{2g}^1 mode. Qualitatively similar results have been observed in graphene: the peak position of G band, an in-plane vibrational mode, is less susceptible to the substrate influence than an out-of-plane vibration mode $\sim$861 cm^{-1} [103, 116]. Similarly it is reasonable to expect that in MoS$_2$ the in-plane mode (E_{2g}^1) will be less affected by the interaction between film and substrate than the out-of-plane mode (A_{1g}). Thus, it is not difficult to understand that the E_{2g}^1 mode typically shows more linear temperature dependent Raman shift than A_{1g} mode for both 1L and 2L samples. The difference between the SiO$_2$ and sapphire substrate also indicates that the coupling between the film and substrate depends on the substrate type and/or how the film and substrate is bonded.

The temperature dependent data of all the samples are fitted to a third order polynomial function according to Eq.(4.1), with the coefficients listed in Table 4.1. The linear temperature coefficients of E_{2g}^1 and A_{1g} in bulk MoS$_2$ are $\chi_1 = -0.0221$ $\pm$ 8.9 $\times$ 10-4 cm^{-1}/K and $-0.0197 \pm 8.9 \times$ 10-4 cm^{-1}/K, respectively. Bulk MoS$_2$, as the reference, can be treated as a stacking of single-layered MoS$_2$ films, and each layer has the same properties. With increasing temperature, all layers expand with the same rate without introducing any strain, leading to a nearly linear redshift of the Raman peak position for both E_{2g}^1 and A_{1g} modes. Although the interlayer coupling has led to significant frequency shifts for the two modes between 1L and bulk, the changes in temperature coefficients are expected to be relatively small. For the E_{2g}^1 mode, the first-order temperature coefficients (χ_1) of SiO$_2$ samples, both 1L and 2L,
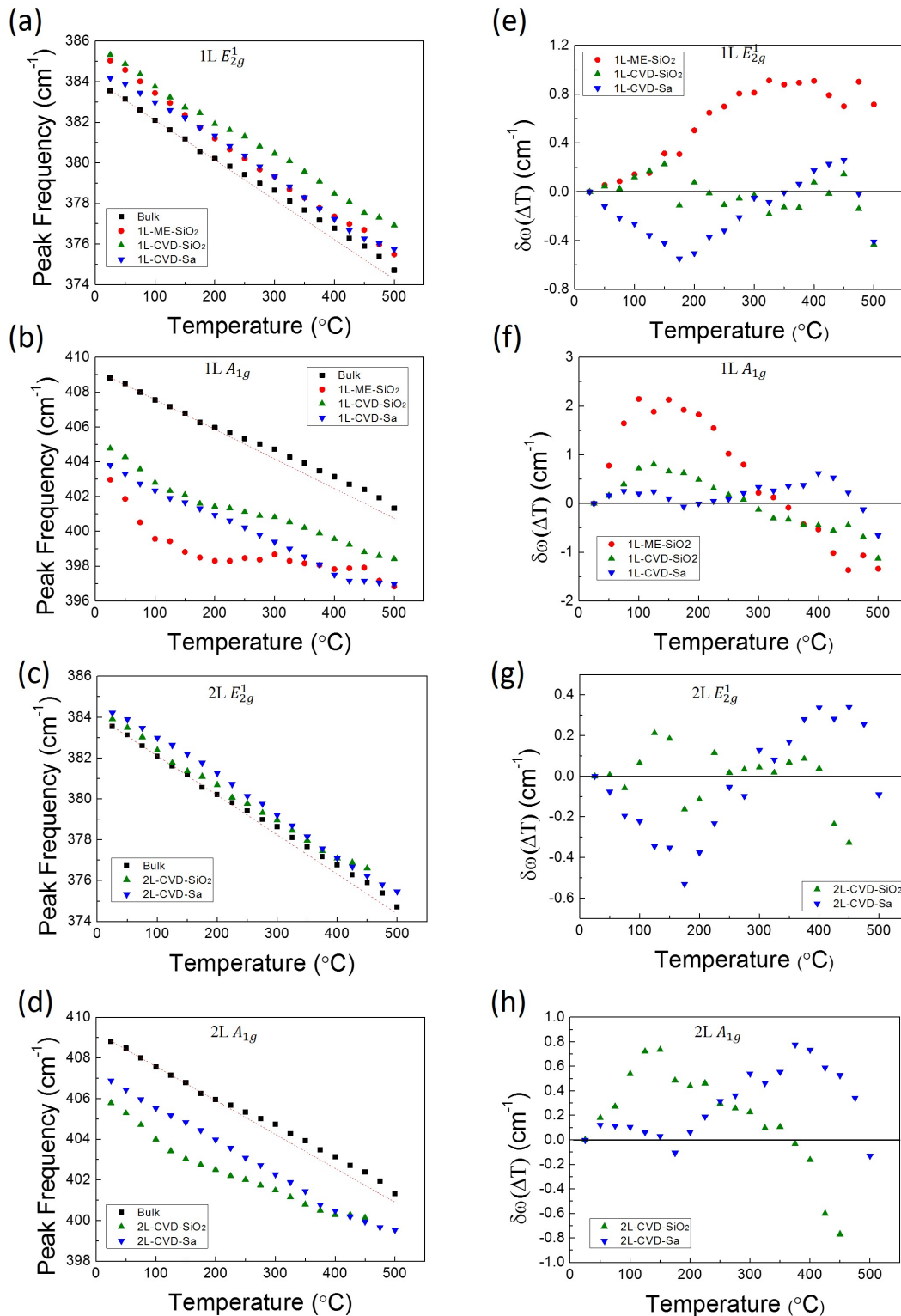
Figure 4.4: The temperature dependence of E^1_{2g} and A_{1g} modes for all six samples. (a)-(d) Temperature dependence of Raman frequencies of E^1_{2g} and A_{1g} modes in bulk and all other 1L and 2L samples. (e)-(h) The Raman frequency deviation of 1L and 2L MoS$_2$ relative to bulk MoS$_2$ as the reference.
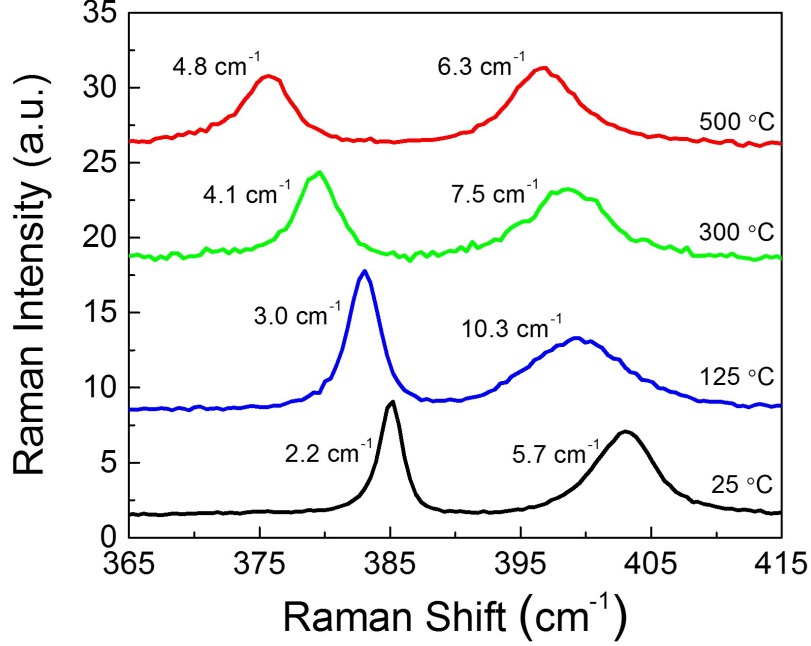
Figure 4.5: Representative Raman spectra of 1L-ME-SiO$_2$ sample at selected temperatures. The FWHM of E_{2g}^1 and A_{1g} are labelled next to the peaks.

are close to that of bulk MoS$_2$, while those of the sapphire samples are much smaller. For A_{1g}, all the SiO$_2$ samples yield much larger χ_1's than that of bulk MoS$_2$, while sapphire samples are close to bulk MoS$_2$. Our results for the films on SiO$_2$/Si are contradicting to or significantly different from those reported in the literature, because the improved data accuracy allows to examine the nonlinear effect that was neglected.

Because all the SiO$_2$ samples were produced by mechanical exfoliation with the scotch tape, including transferred MoS$_2$ films, it is possible that wrinkles or ripples were introduced to the films, resulting in a considerable strain in the film. Figure 4.6 gives the spatial maps of the Raman frequencies of E_{2g}^1 and A_{1g} modes for mechanically exfoliated single-layer MoS$_2$ film on SiO$_2$/Si (1L-ME-SiO$_2$) at room temperature. The maps demonstrate that the frequency of A_{1g} show a larger variation than that of E_{2g}^1, indicating that the morphology of the film impacts the Raman frequency of A_{1g} more than that of E_{2g}^1. On the other hand, both 1L and 2L MoS$_2$ films were originally

Table 4.1: Temperature coefficients of bulk, 1L and 2L samples with polynomial fitting to third order.

	χ_1 (cm^{-1}/K)	χ_2 (cm^{-1}/K^2)	χ_3 (cm^{-1}/K^3)
E_{2g}^1			
bulk	$-0.0221 \pm 8.9 \times 10^{-4}$	$2.12 \times 10^{-5} \pm 4.4 \times 10^{-6}$	$-2.94 \times 10^{-8} \pm 6.1 \times 10^{-9}$
1L-ME-SiO$_2$	-0.0241 ± 0.0015	--	--
1L-CVD-SiO$_2$	-0.0217 ± 0.0017	$2.04 \times 10^{-5} \pm 8.4 \times 10^{-6}$	$-2.68 \times 10^{-8} \pm 1.2 \times 10^{-8}$
1L-CVD-Sa (till 425 °C)	$-0.0143 \pm 5.7 \times 10^{-4}$	$-1.44 \times 10^{-5} \pm 3.4 \times 10^{-6}$	$7.71 \times 10^{-9} \pm 5.6 \times 10^{-9}$
2L-CVD-SiO$_2$ (till 400 °C)	-0.0233 ± 0.0018	$3 \times 10^{-5} \pm 1.1 \times 10^{-5}$	$-4.61 \times 10^{-8} \pm 2 \times 10^{-8}$
2L-CVD-Sa (till 425 °C)	$-0.0135 \pm 8.4 \times 10^{-4}$	$-2.54 \times 10^{-5} \pm 5.0 \times 10^{-6}$	$2.93 \times 10^{-8} \pm 8.2 \times 10^{-9}$
bulk (Ref. [117])	-0.0147		
1L ME SiO$_2$ (Ref. [118])	-0.0179		
2L ME SiO$_2$ (Ref. [118])	-0.0137		
Few layers (Ref. [119])	-0.0132		
A_{1g}			
bulk	$-0.0197 \pm 8.9 \times 10^{-4}$	$2.49 \times 10^{-5} \pm 4.4 \times 10^{-6}$	$-3.53 \times 10^{-8} \pm 6.1 \times 10^{-9}$
1L-ME-SiO$_2$	-0.0626 ± 0.0038	$2.11 \times 10^{-4} \pm 1.7 \times 10^{-5}$	$-2.34 \times 10^{-7} \pm 2.1 \times 10^{-8}$
1L-CVD-SiO$_2$	-0.0301 ± 0.0023	$8.15 \times 10^{-5} \pm 1.1 \times 10^{-5}$	$-1.00 \times 10^{-7} \pm 1.6 \times 10^{-8}$
1L-CVD-Sa (till 425 °C)	-0.0199 ± 0.0012	$3.10 \times 10^{-5} \pm 7.2 \times 10^{-6}$	$-5.77 \times 10^{-8} \pm 1.2 \times 10^{-8}$
2L-CVD-SiO$_2$ (till 400 °C)	-0.0310 ± 0.0018	$8.56 \times 10^{-5} \pm 1.2 \times 10^{-5}$	$-1.16 \times 10^{-7} \pm 2.0 \times 10^{-8}$
2L-CVD-Sa (till 425 °C)	-0.0160 ± 0.0014	--	--
bulk (Ref. [117])	-0.0123		
1L ME SiO$_2$ (Ref. [118])	-0.0143		
2L ME SiO$_2$ (Ref. [118])	-0.0189		
Few layers (Ref. [119])	-0.0123		

grown on sapphire. It has been reported, for graphene, the possibility of forming bonds between mechanically exfoliated graphene and substrate is quite low; however, such bonds are possible with high-temperature growth. It is reasonable to believe that the CVD growth of MoS_2 films at the temperature higher than $800\,°C$ could produce somewhat stronger bonding between the MoS_2 film and sapphire substrate than in the case of transferred film. With increasing temperature, the chemical bonding would influence the in-plane vibration, giving rise to a damping of Raman frequency redshift to E_{2g}^1 mode at the low temperature region, as manifested on the reduced magnitude of χ_1 for the CVD-grown MoS_2 films on sapphire. Furthermore, the film-substrate coupling leads to the sign changes for both χ_2 and χ_3 compared to the bulk for the E_{2g}^1 mode of the on-sapphire samples. In contrast, mechanically transferred MoS_2 films on SiO_2/Si do not form the chemical bonding between film and substrate other than van der Waals force, leading to the temperature dependence of Raman shift or χ_1 of the E_{2g}^1 mode similar to bulk MoS_2. However, the MoS_2 films on SiO_2/Si are more likely to be affected by the changes in the film morphology such as wrinkles and ripples when temperature increases, due to TEC mismatch between MoS_2 and SiO_2. These changes of morphology in turn will have a large impact on out-of-plane vibration (A_{1g}), causing not only the nonlinear effect of temperature coefficient but also the large deviation of χ_1 from bulk MoS_2 for the SiO_2/Si samples. As for the sapphire samples, the chemical bonding restricts the MoS_2 film from morphology change, and the coupling with the substrate has a relatively small influence on the A_{1g} mode. Therefore, we can conclude that the morphology of MoS_2 films plays a significant role in temperature dependence of A_{1g} mode, which leads to the large and highly non-linear deviation from the bulk, while the bonding between film and substrate introduces weaker effects, in similar magnitudes, to both E_{2g}^1 and A_{1g} modes on their temperature induced Raman shifts.

The integrated Raman intensity for both E_{2g}^1 and A_{1g} modes has been found to
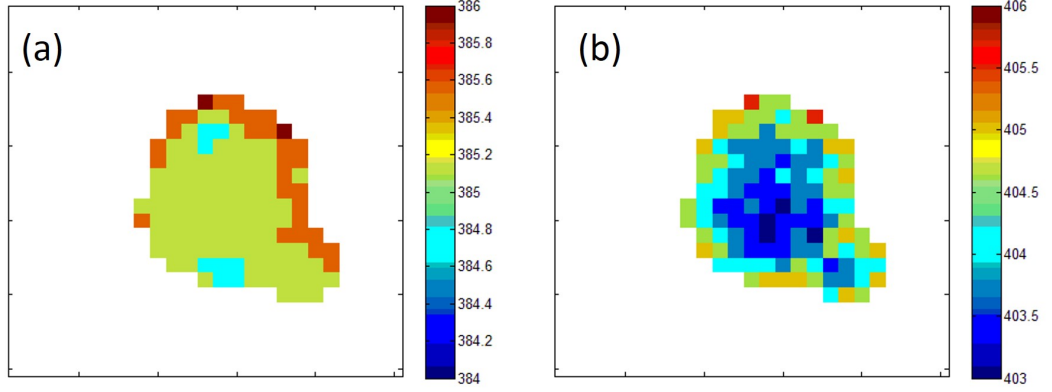
Figure 4.6: Spatial maps (6 μm ×6 μm) of the Raman frequencies of (a) E_{2g}^1 and (b) A_{1g} modes for 1L-ME-SiO$_2$ sample, and the unit is cm^{-1}.

decrease in all CVD-grown samples when T is greater than $400\,°C$, possibly due to the decomposition of MoS$_2$ films. The thermal decomposition temperature for most samples including bulk is somewhere $> 800\,°C$, except for 2L-CVD-SiO$_2$ being near $450\,°C$. For all CVD-grown MoS$_2$ films on sapphire, no Raman signal is detectable when the temperature reaches $575\,°C$, indicating the decomposition of MoS$_2$ films.

The Raman spectrum does not recover at room temperature after reaching the maximum temperature. For 1L-ME-SiO$_2$, the main change is that the frequency difference between A_{1g} and E_{2g}^1 modes increases by 2.5 cm^{-1}, as shown in Figure 4.7. In addition, their peak intensities decrease. There are at least two possible reasons: (1) the strain or morphology has changed, as expected, (2) the sample might be partially oxidized or decomposed. Similar results have been reported for graphene [120].

4.2.2 Simulation for Temperature Dependence of Raman Shift

As Eq.(2.14) shows, the intrinsic temperature dependence of the Raman shift can be divided into thermal expansion of the lattice ($\Delta\omega_E$) and an anharmonic effect ($\Delta\omega_A$) which causes the change of phonon self-energy. In addition, thermally induced strains due to TEC mismatch ($\Delta\omega_M$) between MoS$_2$ film and substrate should be
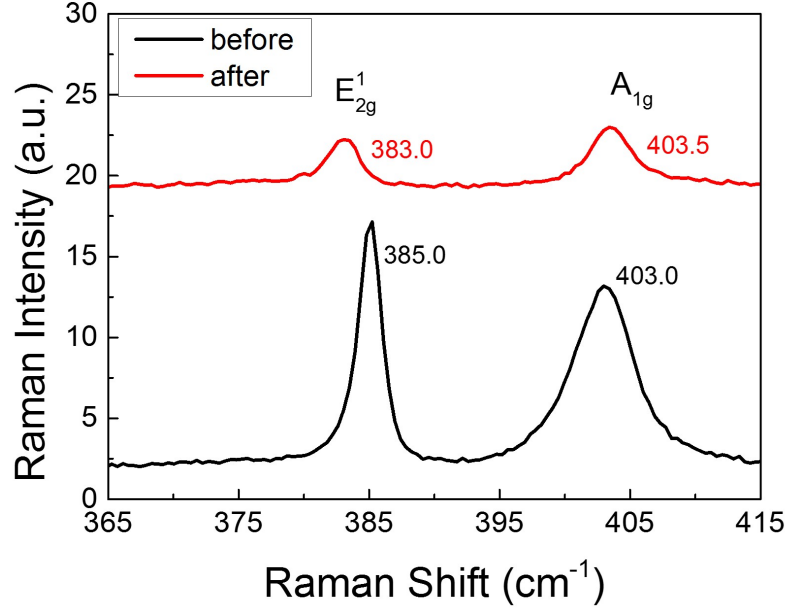
Figure 4.7: Raman spectra collected before and after temperature-dependent Raman measurements.

considered. Thus, the measured frequency change can be written as [22]:

$$\Delta\omega(T) = \Delta\omega_E(T) + \Delta\omega_A(T) + \Delta\omega_M(T), \tag{4.2}$$

where the term $\Delta\omega_M$ can be expressed as [22]:

$$\Delta\omega_M(T) = \beta \int_{25\,°C}^{T} \left(\alpha_{\mathrm{sub}}(T) - \alpha_{\mathrm{MoS_2}}(T)\right) \mathrm{d}T, \tag{4.3}$$

where β is the biaxial strain coefficient, α_{sub} and α_{MoS_2} are the TECs of substrate and MoS$_2$, respectively. With increasing temperature, both MoS$_2$ and SiO$_2$ expand but at different rates, resulting in strain in the MoS$_2$ thin films. Since the TEC of MoS$_2$ is larger than that of SiO$_2$, the strain in the film will be compressive. When the strain reaches a critical point the MoS$_2$ film tends to slip on the surface of the substrate as well as change the film morphology. For 1L-ME-SiO$_2$ sample, this process takes place at $\sim$100 °C where there is an obvious slope transition of A_{1g} frquency shift. As

a result, defects may be introduced in the MoS_2 film such as the breakdown of Mo-S bonds and the slow decomposition of the film, showing a broadening of A_{1g} Raman peak (Figure 4.5).

Eq.(4.3) assumes that the film and substrate is in coherent strain, which is likely invalid for the transferred film. For bulk MoS_2, there is no TEC mismatch between MoS_2 layers, so that the third term is zero. Therefore, using Eq.(2.14) the Raman shift of bulk MoS_2 can be simulated. To simulate the contribution of thermal expansion of the lattice ($\Delta\omega_E$) from Eq.(2.15), the Grüneisen parameters of both E_{2g}^1 and A_{1g} modes for bulk MoS_2 are $\gamma(E_{2g}^1) = 0.21$ and $\gamma(A_{1g}) = 0.42$ [121], respectively. The in-plane and out-of-plane TECs for bulk MoS_2 can be derived from expressions as below [122]:

$$\alpha_a(T) = \left(\frac{0.6007 \times 10^{-5} + 0.6958 \times 10^{-7}T}{a}\right)\left(\frac{1}{°C}\right), \qquad (4.4a)$$

$$\alpha_c(T) = \left(\frac{0.1064 \times 10^{-5} + 1.5474 \times 10^{-7}T}{c}\right)\left(\frac{1}{°C}\right), \qquad (4.4b)$$

where a and c are the lattice constants of MoS_2 in Å. They are calculated to be $2.48 \times 10^{-6}/°C$ and $9.14 \times 10^{-6}/°C$, respectively, for in-plane and out-of-plane TECs at room temperature. The second term of right-handed side in Eq.(2.14) is expressed as Eq.(2.18a), which is called "self-energy" shift due to anharmonic coupling of multiple phonons. The coefficients A and B can be estimated by fitting the rest frequency shift after subtracting the contribution of thermal expansion of the lattice. The fitting parameters of A and B for both E_{2g}^1 and A_{1g} modes are listed in Table 4.2. Figure 4.8 shows the simulated Raman shifts of both E_{2g}^1 and A_{1g} modes for bulk MoS_2 with good agreement to experimental results. The results show that the pure thermal expansion effect is relatively small, and the self-energy contribution dominates the redshift.

Table 4.2: The fitting parameters A and B for both E_{2g}^1 and A_{1g} modes used in three- and four-phonon coupling model.

bulk MoS$_2$	A (cm^{-1})	B (cm^{-1})
E_{2g}^1	-3.05835	0.04204
A_{1g}	-5.68777	0.26566
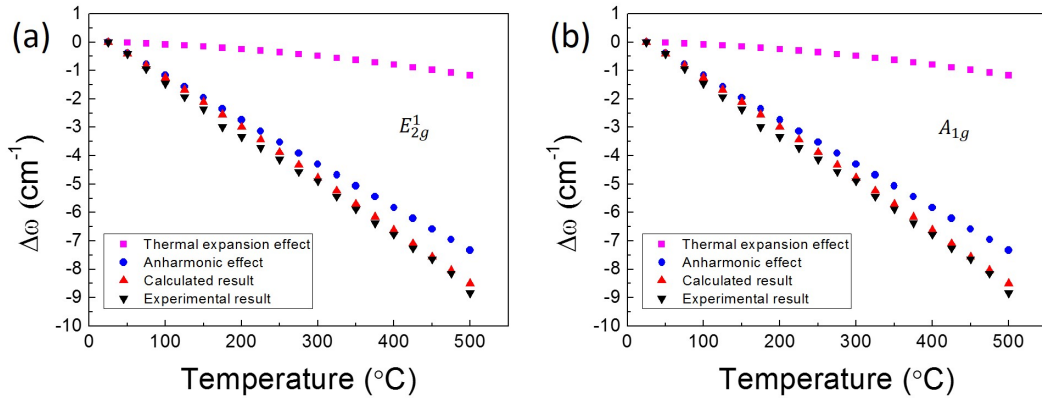
Figure 4.8: The modeling of temperature dependent Raman shift. The model of temperature dependent Raman shift relative to room temperature including the contributions of thermal expansion effect of lattice and anharmonic effect as compared to experimental results of bulk MoS$_2$ for (a) E_{2g}^1 and (b) A_{1g} modes.

4.2.3 Full Width at Half Maximum (FWHM)

Figure 4.9 shows the temperature dependent FWHM of both E_{2g}^1 peak and A_{1g} peak for all samples, by fitting to a Lorentzian lineshape function. Bulk MoS$_2$ has room-temperature FWHMs of 1.6 and 2.2 cm^{-1}, respectively, for E_{2g}^1 and A_{1g}. Other samples have greater FWHMs, indicating that the film-substrate coupling and defects existing in these samples may have caused the peak broadening. The FWHM of E_{2g}^1 mode, in general, increases linearly with increasing temperature. However, the A_{1g} mode does not show a monotonic dependence but with a maximum linewidth in the middle of the temperature range. As it is discussed above, the mismatch of TECs between MoS$_2$ films and substrates gives rise to changes of morphology e.g. wrinkles or ripples, consequently leading to a significant change of the temperature

coefficients of A_{1g} mode. For all 1L and 2L samples, the FWHM of A_{1g} reaches the maximum when the realignment process occurs. For instance, the anomaly of temperature dependent Raman shift of 1L-ME-SiO$_2$ takes places at the temperatures starting from $\sim$100 °C, while the FWHM reaches the maximum at 100 °C and then starts to decrease afterward. This gives an additional illustration that the change of the morphology by the TEC mismatch can affect the out-of-plane vibrational mode more than the in-plane mode when the temperature reaches a critical value.
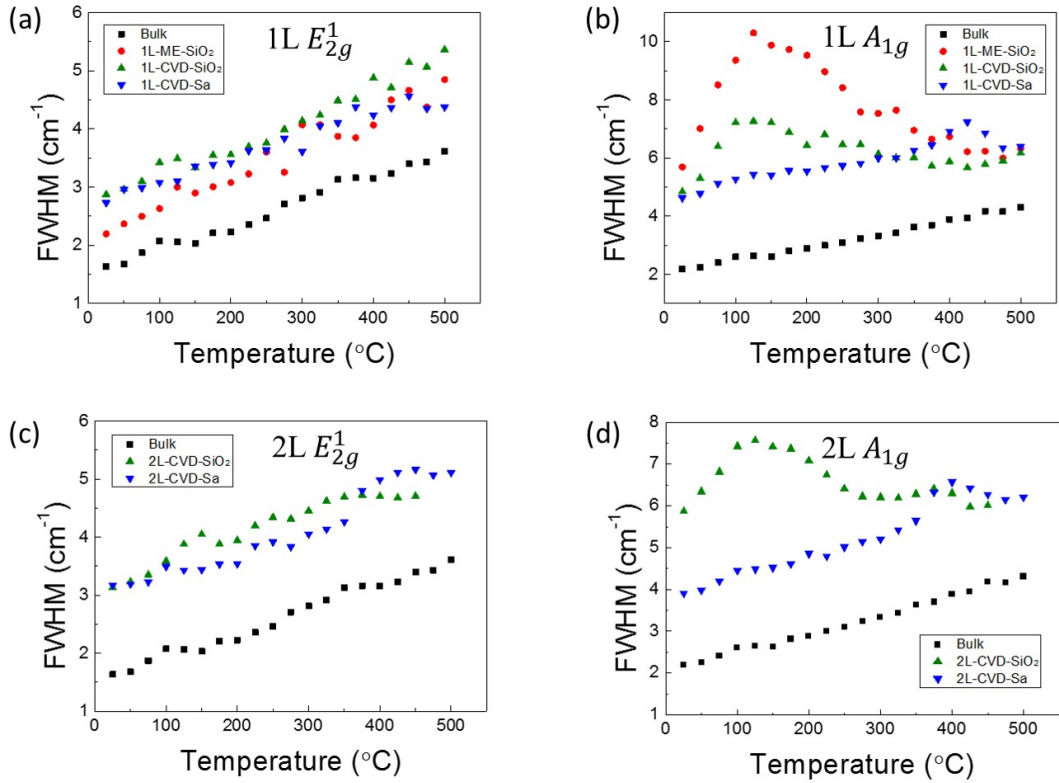
Figure 4.9: Temperature dependence of FWHM of E_{2g}^1 and A_{1g} modes in bulk and all other 1L and 2L samples.

4.3 Annealing Effect on Monolayer MoS$_2$ Film Transferred on SiO$_2$/Si Substrate

The morphology plays a significant role in the properties of MoS$_2$ films, and the morphologic variation of the film in a very thin film like a monolayer typically results in variation of strain in the film. It has been well studied both theoretically and experimentally that the strain in the two-dimensional material can be detected

through the shift of its phonon modes using micro-Raman spectroscopy. For monolayer MoS_2, E^1_{2g} mode is sensitive to the strain, while A_{1g} mode shows weaker strain dependence but it is also sensitive to doping in the film [123]. Besides using E^1_{2g} shift as an indicator of the strain, the bandgap exhibits sensitive response to the strain applied in MoS_2 film, which can be used as another method to extract the strain distribution in the film. In addition to strain effect, the doping effect is another key element that affects the properties of monolayer MoS_2, which can be analyzed by the shift of A_{1g} mode as well as the PL spectrum. The origin of doping for monolayer MoS_2 is considered to be the defects in the film and the charge transfer between the substrate and the film [114, 124].

Comparing the temperature dependence of monolayer MoS_2 films on SiO_2 and sapphire substrates, for A_{1g} mode, the nonlinear dependence of SiO_2 samples, as we discussed above, is quite possibly attributed to the morphologic change with increasing temperature, while, for E^1_{2g} mode, the smaller temperature coefficient of sapphire samples is due to the bonding at the interface of the substrate and the film. The temperature-dependent Raman measurements can be considered as an annealing process for the samples. Since the annealing can significantly change the morphology of the film as well as the bonding between the substrate and the film, one may ask: "would the temperature dependence be different if annealing the films for a second round?" In our previous temperature dependent studies, in order to understand the temperature dependences of the material properties in the full temperature range up to the decomposition temperature, we tended to bring the sample to the highest possible temperature at which the data could be practically taken. Thus, at the end of the measurement, the sample was damaged. However, as mentioned above, the morphology change was occurring along the process of varying temperature, which is effectively an annealing process. In this section, we report the temperature dependent study of MoS_2 monolayer by repeating the heating cycle, but each time only

increasing the temperature to a "safe" level.

Monolayer MoS_2 film was originally grown on sapphire by CVD and then transferred onto Si substrate coated with 300 nm thick SiO_2 using polystyrene (PS) [125]. Figure 4.10a shows the optical image of the MoS_2 film with its AFM image in Figure 4.10b. The thickness is measured to be ~1 nm, indicating it is monolayer. The larger thickness of this transferred monolayer than the previous ME sample suggests a larger morphologic variation of this sample. Wrinkles and cracks can be seen in optical image Figure 4.10a. Wrinkles, as one typical morphology feature in a two-dimensional material, can manifest as local variation in strain. In order to further confirm whether the film is monolayer, the mapping of frequency difference between A_{1g} and E_{2g}^1 modes over an area of 20 µm × 20 µm (marked square in Figure 4.10a) is shown in Figure 4.10c, with a maximum of 19.2 cm^{-1}, indicating the film overall is monolayer. The strip of relatively larger frequency difference in the map matches to a wrinkle in the film.
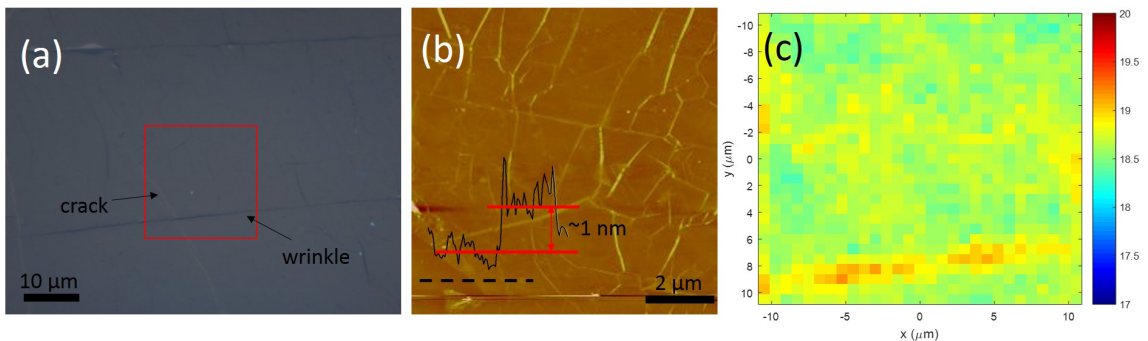
Figure 4.10: The optical image and characterizations of the monolayer MoS_2 film transferred onto SiO_2/Si substrate. (a) Optical image, (b) AFM image, (c) Map of frequency difference $\Delta\omega$ between E_{2g}^1 and A_{1g} modes in the red-squared area.

Figure 4.11 presents the Raman and PL mapping results at room temperature before annealing the film using spatial resolved micro-Raman and PL spectroscopy. Laser power of ~1 mW at 532 nm and 50× lens were used. The mapping data of Raman intensity (Figure 4.11a-b) show overall uniform intensity distribution over the

film except for around the crack with smaller intensity and along the wrinkle with higher intensity. However, the PL intensity mapping shows more significant variation of $\sim$20% (Figure 4.11c). Raman and PL peak position mapping results are shown in Figure 4.11d-f, with maximum shifts of $\sim$0.6 cm^{-1} for E_{2g}^1 mode, $\sim$0.7 cm^{-1} for A_{1g} mode, and $\sim$12 meV for PL, respectively. The deformation potentials for Raman modes and bandgap under biaxial strain have been estimated to be $\sim$4.7 cm^{-1}/% for E_{2g}^1, $\sim$1.8 cm^{-1}/% for A_{1g}, and $\sim$80 meV/% for bandgap, respectively [126]. Thus, the corresponding strain difference in the film, using the maximum difference in the peak position, can be estimated to be $\sim$0.13% for E_{2g}^1, $\sim$0.39% for A_{1g}, and $\sim$0.15% for PL, respectively. The non-uniform strain distribution, reflected in the E_{2g}^1 frequency fluctuation, indicates the rippling of the film. However, the estimated strain difference from A_{1g} mode is much larger than that from E_{2g}^1 mode and PL, indicating that the doping effect plays a significant role in monolayer MoS$_2$ film. By comparing the peak position mapping of E_{2g}^1 and PL peak positions, the blue-circled (red-circled) area with relatively higher (lower) frequencies in E_{2g}^1 mode, which are expected to be under relatively larger compressive (tensile) strain, also exhibit higher (lower) PL energies, reflecting as lower (higher) PL intensity. This phenomenon can be explained by the relocalization of photo-induced excitons which tend to diffuse to lower bandgap regions before recombining. In contrast, areas with relative larger tensile train have lower bandgap energies , thus trapping excitons and generating stronger PL locally (Figure 4.11c).

Single-point temperature-dependent Raman measurements were carried out in the temperature range from room temperature to 305 °C with the step of 20 °C, with the same setup as those of previous MoS$_2$ samples. The sample point was selected from the central area. The first-cycle temperature dependence of both Raman modes of the monolayer MoS$_2$ film is shown in Figure 4.12a-b, with several representative spectra at different temperatures shown in Figure 4.12c. As expected, both E_{2g}^1 and
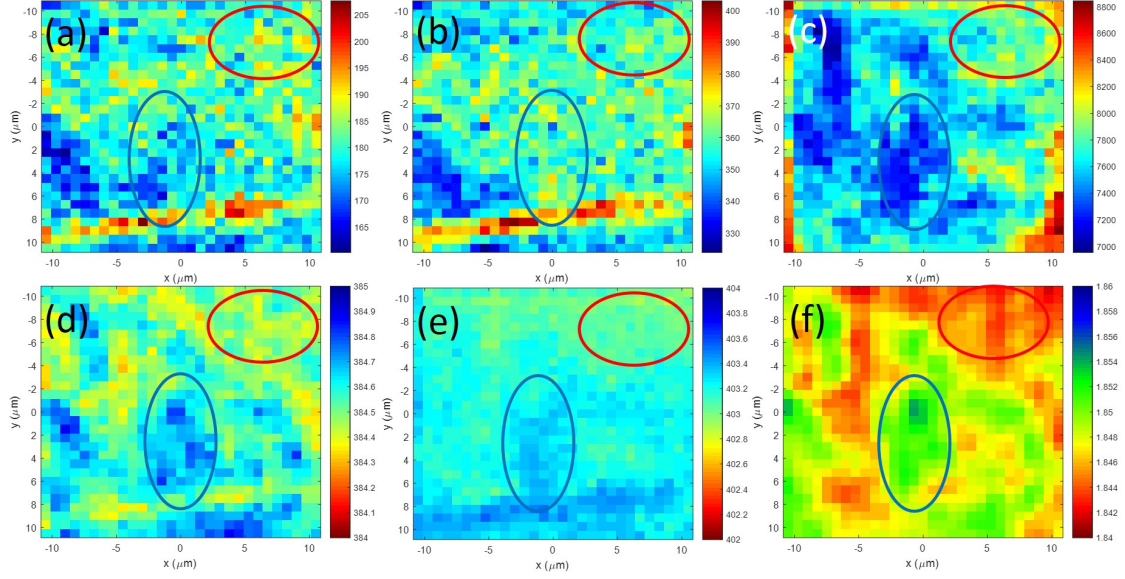
Figure 4.11: The Raman and PL mapping results of the monolayer MoS$_2$ film. (a)-(c) The intensity maps of E_{2g}^1, A_{1g} and PL intensities. (d)-(e) The maps of peak positions of E_{2g}^1, A_{1g} and PL.

A_{1g} modes, in general, exhibit redshift in their frequencies with increasing temperature. The E_{2g}^1 mode shows a very linear temperature dependence while the A_{1g} mode highly nonlinear, in good agreement with the results of previous MoS$_2$ samples. The temperature dependence of E_{2g}^1 mode is fitted by Eq.(3.1) and that of A_{1g} mode is fitted by Eq.(4.1) up to the third order, and the temperature coefficients are listed in Table 4.3. As discussed earlier, the nonlinear temperature dependence of A_{1g} mode is attributed to the change of film morphology, while E_{2g}^1 mode is not sensitive to morphology. With increasing temperature, the film tends to change its morphology due to the mismatch of TEC between the SiO$_2$ substrate and MoS$_2$ monolayer. The TEC of SiO$_2$ is $\sim 0.5 \times 10^{-6}$ K^{-1} at room temperature, much smaller than monolayer MoS$_2$ ($\sim 7 \times 10^{-6}$ K^{-1} at RT), thus, its thermal expansion with increasing temperature is much smaller than that of MoS$_2$. Therefore, the strain within the small measured spot tends to accumulate with increasing temperature, and eventually goes beyond the confinement of vdW force, resulting in the change of the morphology of the film.

Table 4.3: Temperature coefficient of E_{2g}^1 and A_{1g} modes in two temperature cycles.

		First cycle	Second cycle
E_{2g}^1	χ (cm^{-1}/K)	$-0.0192 \pm 3.2 \times 10^{-4}$	$-0.0183 \pm 8.6 \times 10^{-5}$
A_{1g}	χ_1 (cm^{-1}/K)	-0.0390 ± 0.0035	-0.0198 ± 0.0014
	χ_2 (cm^{-1}/K^2)	$6.97 \times 10^{-5} \pm 2.4 \times 10^{-5}$	$-5.74 \times 19^{-6} \pm 9.8 \times 10^{-6}$
	χ_3 (cm^{-1}/K^3)	$-3.69 \times 10^{-8} \pm 4.8 \times 10^{-8}$	$4.17 \times 10^{-8} \pm 2.0 \times 10^{-8}$
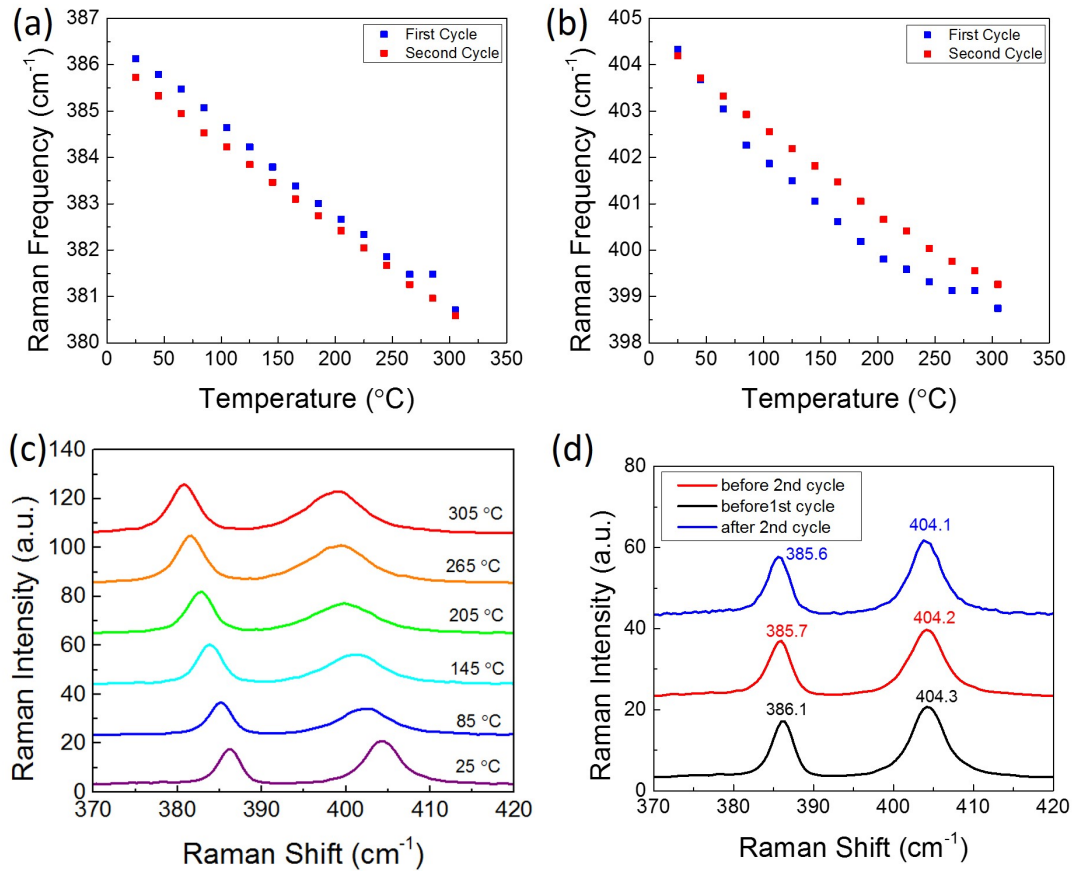
Figure 4.12: The temperature dependence of Raman spectroscopy of monolayer MoS$_2$ up to 305 °C. (a)-(b) The temperature dependences of (a) E_{2g}^1 and (b) A_{1g} modes in the first and second heating cycles. The first cycle is in solid blue square, and the second solid red circle. (c) Representative Raman spectra at different temperatures. (d) The Raman spectra at room temperature before the first-cycle heating, and before and after second-cycle heating.

On the other hand, the morphology of the film varies with increasing tempera-

ture, leading to the change of mechanical coupling of MoS_2 film with SiO_2 substrate. With increasing temperature, the charge transfer between the film and the substrate tends to increase as the contact of the MoS_2 film with the substrate becomes more uniform and close. Since A_{1g} mode is known to be sensitive to doping effect, the stronger charge transfer leads to larger shift of A_{1g} frequency, leading to the initial faster redshift (up to $100\,°C$) of the A_{1g} frequency. After the film's morphology becomes more uniform and stable at higher temperatures, the redshift rate of A_{1g} frequency gradually slow down. In addition, the PS residues left on the film during transfer process [125], though will be eliminated with increasing temperature, may still introduce extra doping into the film to change the temperature dependence of A_{1g} mode. Therefore, the first-cycle annealing process modifies the morphology of the film and gets rid of the polymer residues from transfer process.

Figure 4.12a-b show the second-cycle temperature dependence of the E_{2g}^1 and A_{1g} modes at the same spot as the first cycle, after the sample is annealed at $305\,°C$ for 30 minutes and then cooled down back to RT. Similar to the results of first-cycle measurements, the E_{2g}^1 mode shows a linear temperature dependence, while the A_{1g} remains nonlinear, but the extent of nonlinearity is smaller than that of the first cycle. The results of E_{2g}^1 and A_{1g} modes are fitted with Eq.(3.1) and Eq.(4.1), and their temperature coefficients are listed in Table 4.3. For E_{2g}^1 mode, the temperature coefficient in the second cycle becomes slightly smaller than that in the first cycle, which is attributed to the change of strain, i.e., the bonding has become stronger, in the film after the first-cycle annealing of the film. With the first-cycle annealing, the morphology has been modified, resulting in not only the doping concentration change but also the strain distribution in the film. Figure 4.12d shows the RT Raman spectra acquired before the first- and second-cycle annealing, respectively. The intensity shows very little change. The E_{2g}^1 frequency after the first cycle is slightly smaller than that before the first cycle by 0.4 cm^{-1}, indicating that the strain at this

location becomes more tensile after the first-cycle annealing. The A_{1g} frequency remains nearly the same. In the second cycle of temperature dependent measurements, the overall redshift of E_{2g}^1 mode becomes less, and hence smaller temperature coefficient. For A_{1g} mode, only a small nonlinear temperature dependence is observed, especially at relatively high temperatures, and its first-order temperature coefficient is almost halved compared to the first-cycle temperature dependent measurements. As discussed in first-cycle annealing, the morphology of the film has been modified and rearranged to a more stable condition, so the second-cycle annealing will not change the film morphology significantly. The Raman spectrum after second-cycle annealing, shown in Figure 4.12d, almost shows no changes compared to that after first-cycle annealing, which further confirms our assumption.

Comparing the temperature dependences of these two-cycle annealing on the transferred MoS_2 sample with as-grown MoS_2 film on sapphire, the temperature coefficients of E_{2g}^1 mode from both cycles are larger than those of sapphire samples. As the smaller temperature coefficient of second cycle is attributed to the improved bonding between the substrate and the film, the as-grown monolayer MoS_2 on sapphire, whose bonding in between is much stronger than transferred samples, exhibits even smaller temperature coefficient. For A_{1g} mode, the nonlinear behavior of temperature dependence is quite similar to those previously measured transferred samples, either 1L or 2L, which has been proposed to the morphologic change of film with increasing temperature. However, the extent of nonlinearity decreased in the second cycle, and the Raman spectrum of measured spot showed no significant change before and after the annealing process. These evidences prove that the morphology of the MoS_2 film can be modified through annealing and becomes stable afterwards.

After annealing at $305\,°C$ for one hour and then cooling down to RT, Raman and PL mapping were performed, and the results are shown in Figure 4.13a-d for mapping data of Raman and PL peak positions (Figure 4.13a-c) and PL intensity

(Figure 4.13d). The variations of Raman and PL peak positions are found to be ~ 1 cm^{-1} for E_{2g}^1, ~ 0.7 cm^{-1} for A_{1g}, and ~ 15 meV for PL over the MoS$_2$ film, which corresponds to the variations in strain as $\sim 0.21\%$ for E_{2g}^1, $\sim 0.39\%$ for A_{1g}, and $\sim 0.19\%$ for PL, respectively. The strain difference over the mapped area becomes larger after two cycles of annealing due to the morphologic change of the film as we discussed above. Interestingly, the PL intensity map, as shown in Figure 4.13d, is not exactly following the anti-correlation relation between the peak energy and intensity. For instance, the PL energies of location 1 and 2 (labelled in Figure 4.13c) are higher than surrounding areas, in accord with the higher E_{2g}^1 frequency in location 1 and 2 (the higher frequency is, the lower tensile strain); however, the PL intensity in location 1 is higher than that in surrounding areas while location 2 lower. Therefore, this cannot be simply explained by one mechanism of either strain or doping. Both locations undergo relatively blueshift in E_{2g}^1 frequency, suggesting less tensile strain. However, the A_{1g} frequency in location 1 is smaller than that in location 2 (Figure 4.13b), indicating that the doping concentration in location 1 is higher than that in location 2. In other words, after the rearrangement of film morphology after two cycles of annealing, the mechanical coupling of the MoS$_2$ film with the substrate varies over the film as well as the doping concentration. The concentration in location 2 is lower than that in location 1. Thus, though the PL energy in location 2 is higher than surrounding area, the lower doping concentration still leads to higher PL intensity. Whereas, the lower PL intensity in location 1 can be either explained by funnel effect or high doping concentration that quenches PL. The PL spectra from locations 1 and 2 (Figure 4.13e) show that the full width at half maximum (FWHM) of the PL spectrum at location 2 is 26 nm, smaller than location 1 which is 35 nm, suggesting lower doping concentration in location 2.
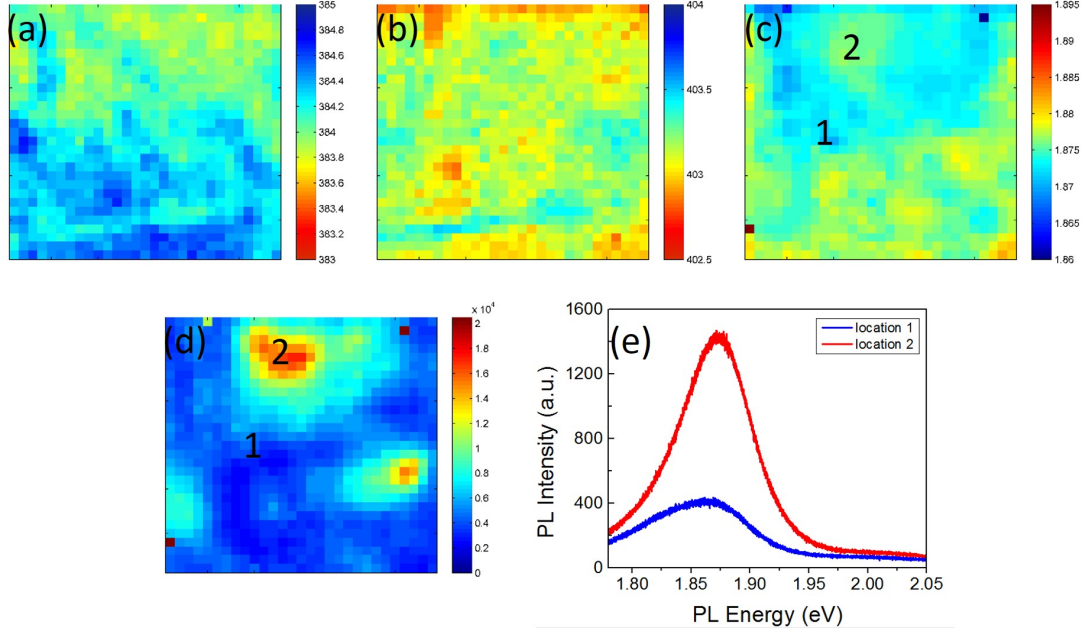
Figure 4.13: The PL and Raman mapping results after the second-cycle heating. (a)-(b) The maps of Raman frequencies of (a) E_{2g}^1 and (b) A_{1g} modes. (c) The map of PL peak position. (d) The intensity map of PL. (e) PL spectra of location 1 and 2 labelled in c.

4.4   Conclusions

In summary, temperature-dependent Raman studies were performed to investigate the vibrational properties of the in-plane E_{2g}^1 and out-of-plane A_{1g} modes of single- and bi-layer MoS_2 samples prepared by three methods: (1) as grown by CVD on sapphire substrate, (2) initially grown on sapphire substrate, then transferred onto SiO_2/Si substrate, and (3) ME samples placed on SiO_2/Si substrate, in a temperature range of 25–500 °C. Bulk MoS_2 has also been measured to serve as the references, with the first-order temperature coefficients of the Raman frequency shifts given as $\chi_1(E_{2g}^1) = -0.0221 \pm 8.9 \times 10^{-4}$ cm^{-1}/K and $\chi_1(A^{1g}) = -0.0197 \pm 8.9 \times 10^{-4}$ cm^{-1}/K, respectively, for the E_{2g}^1 and A_{1g} mode. The thermal decomposition temperature is found to be approximately 575 °C for CVD-grown films on sapphire. The film-substrate coupling affects the temperature dependence of Raman frequency, intensity, and linewidth for both E_{2g}^1 and A_{1g} modes in the 1L and 2L MoS_2. The impact

depends on the substrate type and/or film-substrate binding mechanism. For the CVD grown film on the original sapphire substrate with likely chemical bonding between them, the film-substrate coupling significantly reduces the linear temperature coefficients of the Raman shift of the E_{2g}^1 mode to $-0.0143 \pm 5.7 \times 10^{-4}$ cm^{-1}/K for 1L and $-0.0135 \pm 8.4 \times 10^{-4}$ cm^{-1}/K for 2L, but has no or small effect on the A_{1g} mode, with -0.0199 ± 0.0012 cm^{-1}/K for 1L and -0.0160 ± 0.0014 cm^{-1}/K for 2L. For the transferred film on SiO$_2$/Si substrate, originally grown on sapphire by CVD, for the E_{2g}^1 mode, the temperature coefficients were found to be very close to the bulk value as -0.0217 ± 0.0017 cm^{-1}/K for 1L and -0.0233 ± 0.0018 cm^{-1}/K for 2L; but for A_{1g} mode, they increase substantially to -0.0301 ± 0.0023 cm^{-1}/K for 1L and -0.0310 ± 0.0018 cm^{-1}/K for 2L. The substrate effects are most pronounced for the A_{1g} mode, showing as stronger nonlinearity on the temperature shift of the Raman frequency and non-monotonic temperature dependence of the Raman linewidth. Similar or even stronger effects were observed on a mechanically exfoliated 1L film from a bulk single crystal.

To further understand the substrate effect on the MoS$_2$ films, two cycles of temperature-dependent Raman measurements were performed on the same spot of a transferred MoS$_2$ monolayer on SiO$_2$/Si substrate. In the first cycle of annealing, both E_{2g}^1 and A_{1g} modes show the similar temperature dependence as other transferred samples studied earlier, including A_{1g} exhibits extremely nonlinear dependence. Whereas, after the second cycle the temperature dependence becomes more linear with respect to that in the first cycle. In contrary to A_{1g} mode, the temperature dependence of E_{2g}^1 mode in both annealing cycles is quite linear. By comparing the mapping data before and after annealing, evident changes of the film morphology has been observed, which is due to the TEC difference between monolayer MoS$_2$ and substrate.

These results suggest that for the mechanically transferred thin film, due to

the mismatch in thermal expansion between the film and substrate, the temperature change can lead to significant changes in the thin-film morphology as a result of realignment of the film on the substrate, which can be most easily probed by the temperature dependence of the A_{1g} mode associated with the out-of-plane atomic vibration. Temperature dependent Raman study provides an efficient tool for investigating the coupling between the 2D material and substrate either with chemical or mechanical bonding.

Based on the analyses on the results of different samples, we suggest that the most accurate linear Raman temperature coefficients for a hypothetical free-standing monolayer MoS_2 should be: for the E_{2g}^1 mode, -0.0217 ± 0.0017 cm^{-1}/K, obtained from a transferred CVD sample; and for the A_{1g} mode, -0.0199 ± 0.0012 cm^{-1}/K, obtained from an as-grown CVD sample on sapphire, which is supported by -0.0198 ± 0.0014 cm^{-1}/K, obtained by a transferred CVD sample after annealing. These values are practically the same as the bulk values within the error bars.

CHAPTER 5: TEMPERATURE DEPENDENCE OF RAMAN AND PL IN
MONOLAYER WS$_2$

5.1   Fabrication and Characterization of WS$_2$ Samples

5.1.1   Sample Fabrication

The techniques of growing large-area single crystalline monolayer WS$_2$ film and transferring it onto a secondary substrate make the investigation of temperature dependent Raman scattering of monolayer WS$_2$ possible. Five samples were prepared by both ME and CVD: (a) "1L-SiO$_2$" is a monolayer WS$_2$ film grown on Si substrate coated with 300 nm SiO$_2$; (b) "1L-SA-TRI" is a triangular-shaped monolayer WS$_2$ film, grown on sapphire substrate; (c) "1L-SA-FILM" is a large area monolayer WS$_2$ film grown on sapphire substrate; (d) "1L-TRAN-SiO$_2$" is a transferred monolayer WS$_2$ film originally grown on sapphire and then transferred onto SiO$_2$/Si substrate; (e) "Bulk-SiO$_2$" is a thick layer of WS$_2$ (> 20 layers) on the same SiO$_2$/Si substrate as "1L-SiO$_2$". All samples were prepared by our collaborators at NCSU. Figure 5.1 shows the optical images of the five samples (the "bulk" sample is on the same substrate as "1L-SiO$_2$").

5.1.2   Characterization of WS$_2$ Samples

To determine the thickness of WS$_2$ films, an AFM image is shown in Figure 5.2a confirming that the thickness is $\sim$0.7 nm, i.e., monolayer. Similar to MoS$_2$, Raman spectroscopy, as a nondestructive and powerful technique, can be used to determine the layer number of WS$_2$ thin films [46, 127]. Bulk WS$_2$ studied here has the same crystal structure as MoS$_2$ studied in the previous chapter, and belongs to the same point group symmetry of D_{3h}. Figure 5.2b shows the Raman spectra of all the five samples, measured by 441.6 nm laser excitation ($\sim$150 μW). Two major peaks, E_{2g}^1
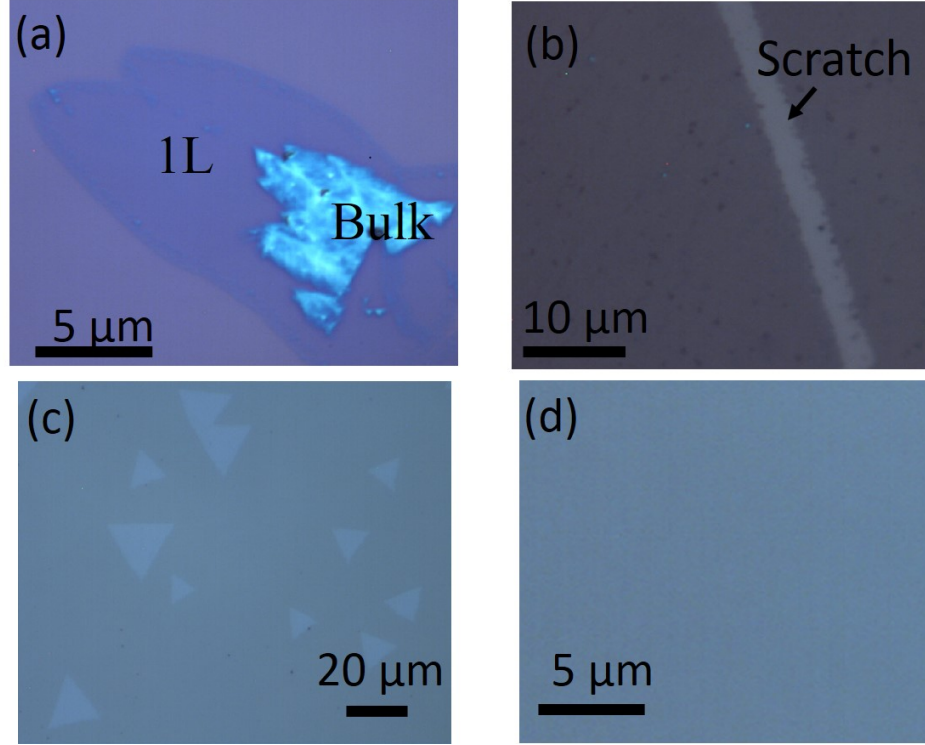
Figure 5.1: The optical images of monolayer WS$_2$ samples. (a) CVD-grown monolayer WS$_2$ on SiO$_2$/Si – 1L-SiO$_2$ accompanied by bulk MoS$_2$ – "bulk"-SiO$_2$. (b) CVD-grown monolayer WS$_2$ transferred onto SiO$_2$/Si – 1L-TRAN-SiO$_2$. (c) CVD-grown monolayer WS$_2$ triangles on sapphire – 1L-SA-TRI. (d) CVD-grown monolayer WS$_2$ film on sapphire – 1L-SA-FILM.

and A_{1g}, are observed, which correspond to the in-plane and out-of-plane vibration modes (the inset of Figure 5.2b). The E_{2g}^1 mode involves the in-plane motion of W+S atoms and A_{1g} the out-of-plane motion of two S atoms. For monolayer WS$_2$, their values are $\sim$355 cm^{-1} and $\sim$417 cm^{-1}, respectively [127]. The frequency difference between these two modes has been shown to be a simple signature to determine the layer number of WS$_2$. In Figure 5.2b, the frequency difference between E_{2g}^1 and A_{1g} modes is 61.7 cm^{-1} for 1L-SiO$_2$, and 65 cm^{-1} for "bulk" WS$_2$. Note that the E_{2g}^1 frequency of the bulk is overall lower than that of monolayer samples, while A_{1g} higher. This is due to the interlayer interactions same as MoS$_2$. Within the monolayer samples, the variation of the frequencies of both E_{2g}^1 and A_{1g} modes is an effect of the substrate (i.e. strain) and doping. More discussions will be given in the

next section. When using near-resonant 532 nm laser excitation, very rich Raman features appear, in particular a very strong second-order peak $2LA(M)$ sitting close to E_{2g}^1 peak, as shown in Figure 5.2c. A Lorentzian fitting procedure is applied to deconvolute $2LA(M)$ and E_{2g}^1 components.
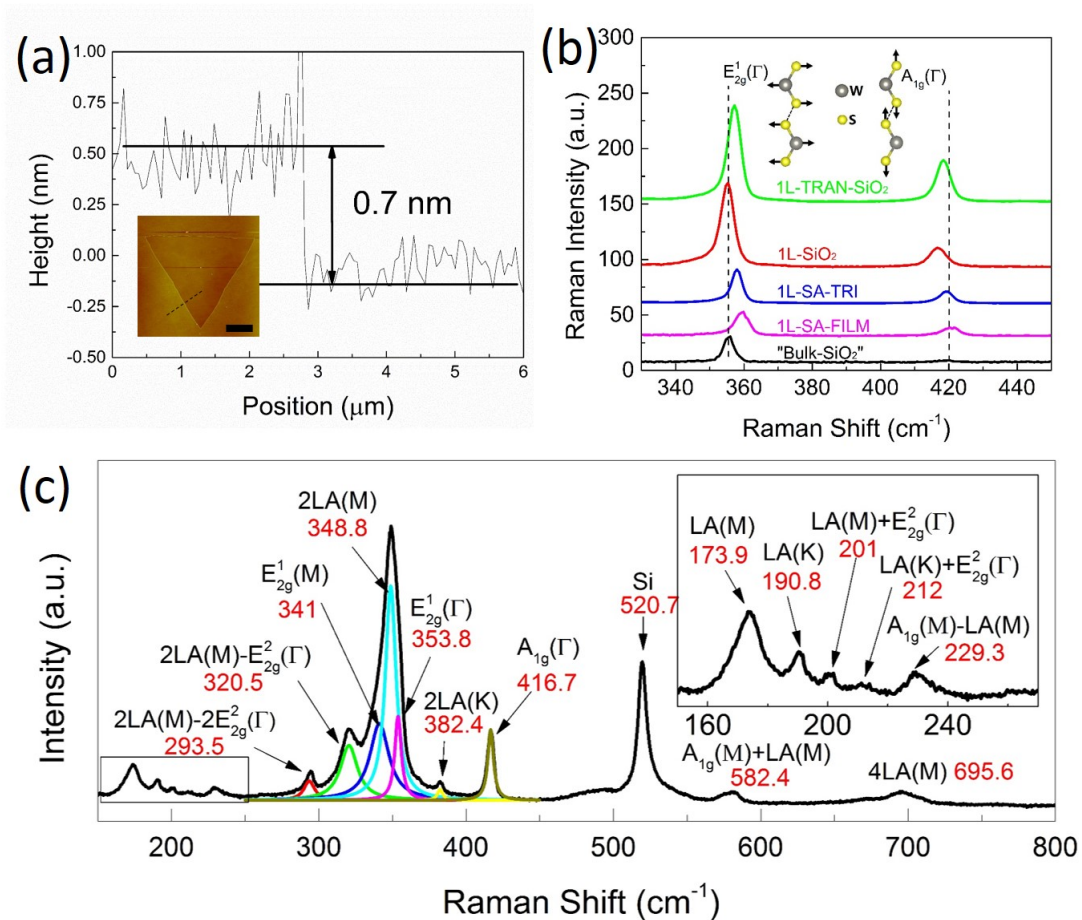
Figure 5.2: The characterizations of all WS_2 samples. (a) The AFM image of 1L WS_2 triangle on sapphire (1L-SA-TRI) showing the thickness is $\sim$0.7 nm. (b) Raman spectra of all the WS_2 samples collected with 441.6 nm laser. The inset shows the atomic displacements for the two major Raman modes E_{2g}^1 and A_{1g}. (c) A Raman spectrum collected with 532 nm laser.

Figure 5.3 shows the comparison of Raman spectra under both 532 nm and 441.6 nm laser excitation for all the four monolayer samples as well as the "bulk" WS_2. Under 441.6 nm excitation, the two on-sapphire samples show comparable Raman intensities, whereas the 1L-SiO$_2$ sample shows lower signal by a factor of 2-3,

but the transferred sample 1L-TRAN-SiO$_2$ has the strongest signal, $\sim$3 times of the on-sapphire samples. Under 532 nm excitation, the most striking observation from comparing the four 1L samples lies in that that signals of the on-SiO$_2$ samples, both as-grown and transferred, are substantially stronger than those of the other two on-sapphire samples, in particular the 1L-SiO$_2$ is stronger by over a factor of 10–20, and 1L-TRAN-SiO$_2$ by a factor of 3–5. Comparing the three as-grown samples, we observe an anti-correlation between the resonant and off-resonant signals, i.e., stronger resonant signal under 532 nm excitation corresponding to weaker off-resonant signal under 442 nm excitation. The transferred film on SiO$_2$ shows the strongest off-resonant signal, about 10 times of the as-grown sample on the same type of substrate, but about a factor of 3 weaker under near resonant excitation. Clearly, it is not possible to explain the variations among these samples simply by the variations in sample quality. These comparisons offer the first indication of the substrate as well as film-substrate bonding dependence of the 2D-WS$_2$ film, and more than one mechanisms at work for these substrate effects. The relative intensities of different samples at the two excitation wavelengths are summarized in Table 5.1.

Table 5.1: Relative intensities of Raman and PL of four monolayer WS$_2$ samples measured by two excitation wavelengths: 532 nm and 441.6 nm. For each column, the weakest intensity serves as unity reference.

	532 nm		441.6 nm	
	Raman	PL	Raman	PL
1L-SiO$_2$	20	7.5	1.0	25
1L-TRAN-SiO$_2$	7.3	300	10	125
1L-SA-TRI	1.7	1.5	3.3	2.5
1L-SA-FILM	1.0	1.0	2.3	1.0

Figure 5.3f-g shows PL spectra of all the WS$_2$ samples measured with 441.6 and 532 nm laser. Monolayer WS$_2$ has two interband transitions near the bulk direct
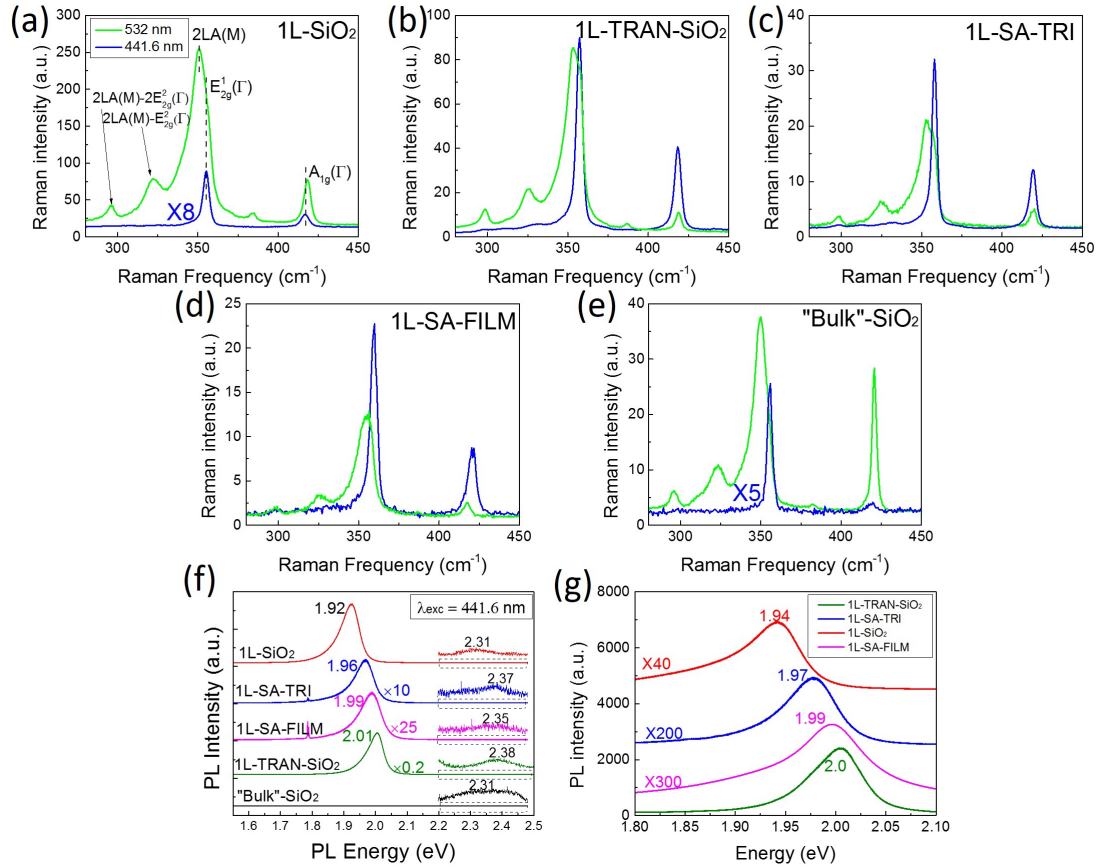
Figure 5.3: The comparison of Raman spectra collected with 441.6 nm and 532 nm lasers. (a)-(f) Raman and PL of all five WS_2 samples with excitation wavelengths of 441.6 nm (blue line) and 532 nm (green line). (f)-(g) PL with (f) 441.6 nm and (g) 532 nm excitation.

transitions at the K point due to spin-orbit splitting of the valence band, assigned as A exciton ($\sim$2.0 eV) and B exciton ($\sim$2.38 eV) [128,129]. The variation of the PL peak position is likely due to the strain effect which is introduced during growth process. The PL intensity of 1L-TRAN-SiO_2 is much stronger than 1L-SiO_2 by approximately a factor of 5, which is opposite to the relative intensity in Raman where 1L-SiO_2 is much stronger. The small bandgap shift should not significantly affect PL intensity, because of typically weak variation of absorption strength with wavelength. There are two known major effects influencing the intensity of band edge PL emission: (1) doping, and (2) optical interference effect. The stronger bonding for the as-grown sample

seems to quench the PL relative to the transferred sample with weaker bonding to the otherwise same SiO$_2$ substrate. However, the PL intensities of the on-SiO$_2$ samples are in general much stronger than the on-sapphire samples, for instance, by as much as 125 times between 1L-TRAN-SiO$_2$ and 1L-SA-FILM. The major PL intensity reduction for the on-sapphire samples could be due to non-radiative recombination via substrate. Additionally, the interference effect of the thin-layer SiO$_2$ could slightly enhance the light absorbed by the WS$_2$ film and the collection efficiency. The relative PL intensities are summarized in Table 5.1. In short, the SiO$_2$ substrate seems to offer much stronger PL than sapphire substrate for either excitation wavelength. These observations illustrate the fact that the film-substrate interaction could be rather complex.

The great enhancement of Raman intensity, especially $2LA(M)$, can be explained by the resonant Raman effect. The B-exciton energy, ~ 2.35 eV, is very close to the energy of green laser that is 2.33 eV. In this case, resonant Raman occurs, which can be described by the equation below [130]:

$$I(E_L) = K \left| \frac{\langle f|H_{e-r}|b\rangle\langle b|H_{e-ph}|a\rangle\langle a|H_{e-r}|i\rangle}{(E_L - E_g - i\Gamma_a)(E_L - E_{ph} - E_g - i\Gamma_b)} \right|^2, \tag{5.1}$$

where $I(E_L)$ is the Raman scattering intensity, and K is a constant; $\langle i \rangle$ is the initial state, $\langle a \rangle$ and $\langle b \rangle$ are two intermediate states, $\langle f \rangle$ is the final state; H_{e-r} and H_{e-ph} are the Hamiltonians of the radiation of the light and the electron-phonon coupling, respectively; E_L is the energy of the incident light, E_g is the energy of the electronic transition, and E_{ph} is the phonon energy; Γ_a and Γ_b are the damping constants related to the lifetimes of the two intermediate states $\langle a \rangle$ and $\langle b \rangle$, respectively. The first term in the denominator of Eq.(5.1) reflects the resonance of the incoming photon with the B exciton transition energy, the second term of the outgoing photon involving the phonon energy. The B-exciton PL emission energy of 1L-SiO$_2$ at 2.31 eV is the closest

to the laser energy among the four 1L samples. The strongest resonant Raman signal from this sample suggests that the incoming electronic resonant plays the dominant role. The resonant effect was shown to become progressively weaker with reducing the excitation wavelength. Although between the two on-SiO_2 samples the Raman intensity difference under 532 nm excitation could be explained by the difference in proximity to the resonance condition due to the B exciton energy level difference (2.31 vs. 2.38 eV), the Raman intensity difference under 441.6 nm could be caused by another mechanism that is yet to be determined. One possibility could be the difference in charge transfer or doping related to the difference in the film-substrate bonding.

5.2   Temperature Dependence of Raman Scattering

The temperature dependent Raman study was reported for a 1L ME WS_2 from 77 to 623 K with the temperature coefficients of both E_{2g}^1 and A_{1g} modes being -0.006 cm^{-1}/K [131], although the data were apparently nonlinear in temperature. The high temperature Raman studies were carried out for the four 1L WS_2 samples as well as "bulk" WS_2 from RT to 500 °C. Figure 5.4a shows the temperature dependent Raman spectra of 1L-SiO_2. For both E_{2g}^1 and A_{1g} modes, the Raman frequency decreases with increasing temperature. In addition, the intensity of $2LA(M)$ decreases drastically as the temperature rises, because the bandgap redshift detunes the laser energy from resonance. Empirically, the temperature dependence of Raman shift, same as MoS_2, can be described by Eq.(3.1). It is noted that for both sapphire samples, one of sapphire Raman peaks at 417 cm^{-1} overlaps with WS_2 A_{1g} peak. Thus, the spectrum of the sapphire substrate was taken at each temperature and carefully subtracted to yield the WS_2 Raman spectrum, as illustrated in Figure 5.5.

The change in Raman frequency ($\Delta\omega$) of WS_2 samples with increasing temperature can be expressed by Eq.(4.2) with the three contributions from $\Delta\omega_E$, $\Delta\omega_A$ and $\Delta\omega_M$. Figure 5.4 shows the temperature dependence of Raman frequency for both E_{2g}^1
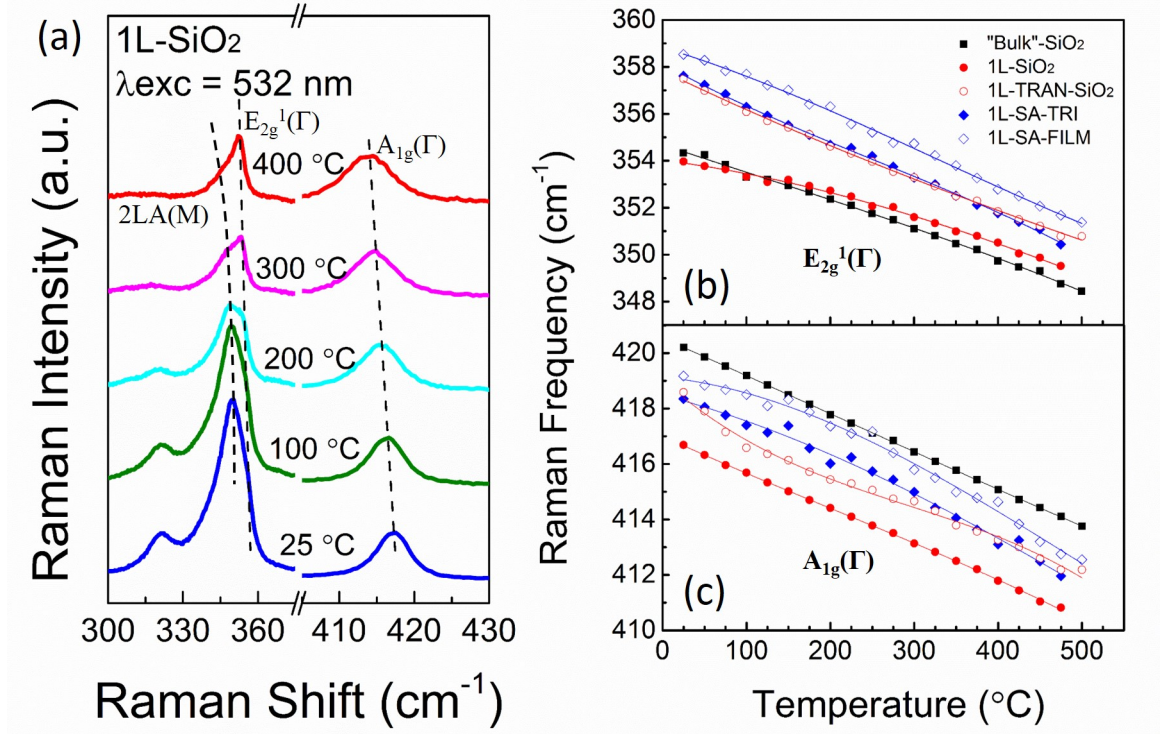
Figure 5.4: Temperature dependence of Raman spectroscopy of all the WS_2 samples. (a) Representative Raman spectra of 1L-SiO$_2$ sample at different temperatures. (b)-(c) Temperature dependence of Raman frequencies of (b) E_{2g}^1 and (c) A_{1g} modes in "bulk" and 1L samples. The solid lines are fitting results using Eq.(4.1).

and A_{1g} modes in all the five samples. As a rough practice, one could consider both E_{2g}^1 and A_{1g} exhibiting linear redshifts with increasing temperature. However, the clearly observable differences in slope among the samples and the subtle non-linearity reflect the intricate film-substrate interaction.

For E_{2g}^1, the study on MoS_2 in the previous chapter indicates that the transferred sample shows the least substrate effect on this in-plane mode. Thus, we may take 1L-TRAN-SiO$_2$ as an approximate reference for a free-standing 1L WS_2. In fact, as shown in Figure 5.4b, the temperature dependence of this sample is very similar to the strain free bulk MoS_2, showing a weak non-linear effect at high temperature. Other than the small variations in frequency, the temperature shifts of the two on-sapphire samples are very similar to that of the 1L-TRAN-SiO$_2$, indicating relatively small strain in the epitaxial film and weak bonding to the substrate. However, the slopes for the two
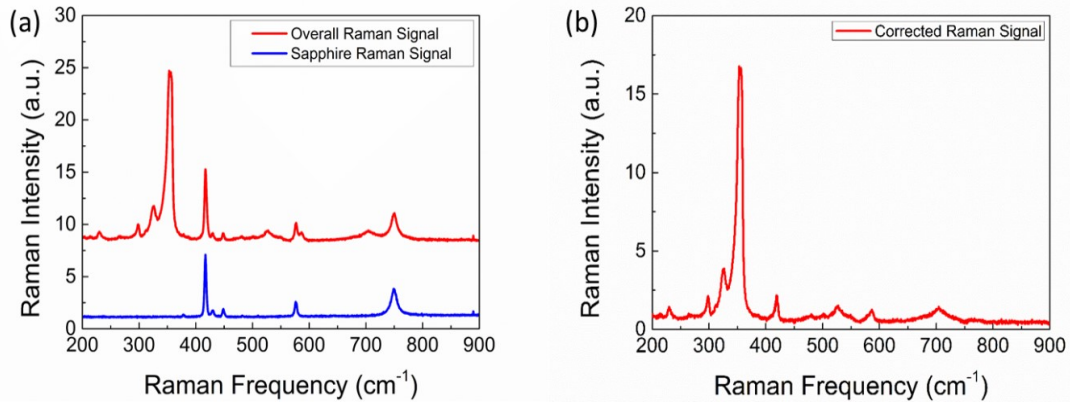
Figure 5.5: The baseline correction of Raman signal from WS_2 monolayer on sapphire. (a) Measured Raman spectra from 1L-SA-TRI (red) and sapphire substrate (blue), respectively, at room temperature. (b) Corrected Raman signal by subtracting Raman signal of sapphire from the overall Raman signal.

as-grown samples on SiO_2 are substantially smaller than that of 1L-TRAN-SiO_2. As suggested by the RT-PL data mentioned above, 1L-SiO_2 is under significant tensile strain at RT, manifesting as the lowest Raman frequency among all the samples. Thus, the third term in Eq.(4.2) becomes significant. The TEC of WS_2 is about one order of magnitude higher than that of SiO_2. With increasing temperature, the WS_2 film expands faster than SiO_2, which in turn results in a release of tensile strain in the WS_2 film. The strain release gives rise to a blue shift that compensates the intrinsic red shift given by the first and the second terms in Eq.(4.2), resulting in an apparent smaller temperature coefficient than 1L-TRAN-SiO_2 and sapphire samples. This is also largely true for the thicker sample, "bulk"-SiO_2, because it is not thick enough to allow the WS_2 to fully relax at RT, which explains why its temperature coefficient is higher than that of 1L-SiO_2 but lower than the other samples. However, for 1L-SA-TRI and 1L-SA-FILM, because the difference in TEC between sapphire and WS_2 is relatively small, no significant strain is generated in the films when cooled down to RT.

For A_{1g}, the previous study on MoS_2 indicates that this out-of-plane mode is particularly sensitive to the morphology of the film (e.g., mesoscopic scale mechan-

ical buckling and chemical residues associated with the transferred film), and very strong non-linearity was observed for the transferred film. As shown Figure 5.4c, the strongest non-linearity is observed for the transferred film 1L-TRAN-SiO$_2$, although not as drastic as reported for a ME MoS$_2$ film on SiO$_2$. The two as-grown samples on SiO$_2$ exhibit rather good linearity and with very close slopes. Because the strain induced frequency shift is much smaller for A_{1g} (-1.7 cm^{-1}/% from the density functional theory (DFT) calculation, to be discussed in section 5.4) than E_{2g}^1 (-4.4 cm^{-1}/%), the release of the tensile strain with increasing temperature partially offsets the intrinsic steeper slope in the initial part, which yields a nice linear dependence for the whole temperature range. Therefore, the intrinsic temperature coefficient for a free standing monolayer or bulk WS$_2$ is expected to be rather close to (but slightly larger) that of 1L-SiO$_2$ or "bulk"-SiO$_2$, respectively. The results for the two on-sapphire samples are somewhat more perturbed by the substrate than the on-SiO$_2$ samples. For the transferred sample, increasing temperature improves bonding with the substrate (e.g., through burning out the chemical residues introduced during the film transfer), thus enhances the charge transfer (n-type doping) from the substrate to the film, leading to the phonon frequency red shift. This effect may explain the accelerated red-shift in 1L-TRAN-SiO$_2$ below 100 °C. With increasing temperature further, thermally activated non-radiative recombination, as revealed by temperature dependent PL results (see section 5.3), tends to deplete the carriers, which slows down the red-shift. Above 250 °C, the temperature dependence approaches that of a free-standing film. This finding suggests that thermal annealing could have significant impact to electronic mobility of a transferred monolayer TMD film, but not in a simple way. On one hand, it improves the film morphology, which could help the mobility; on the other hand, it enhances the bonding to the substrate, which could lead to carrier depletion to the substrate or effectively shorten the carrier lifetime, and thus be detrimental to the mobility. This insight might explain

some reports suggest that the epitaxial TMD film has lower carrier mobility than the transferred film [132], while reversed observations have also been reported [133]. This observation could provide guidance for identifying the optimal thermal annealing process to achieve desirable properties in device applications. The linear fitting results of the temperature coefficients for all the samples are listed in Table 5.2.

Table 5.2: Temperature coefficients of bulk and 1L WS$_2$ samples.

	$E_{2g}^1(\mathrm{cm}^{-1}/K)$	$A_{1g}(\mathrm{cm}^{-1}/K)$
"Bulk"-SiO$_2$	$-0.0124 \pm 2 \times 10^{-4}$	$-0.0136 \pm 4 \times 10^{-5}$
1L-SiO$_2$	$-0.0100 \pm 3 \times 10^{-4}$	$-0.0130 \pm 9 \times 10^{-5}$
1L-TRAN-SiO$_2$	$-0.0142 \pm 1 \times 10^{-4}$	$-0.0124 \pm 4 \times 10^{-4}$
1L-SA-TRI	$-0.0154 \pm 3 \times 10^{-4}$	$-0.0140 \pm 3 \times 10^{-4}$
1L-SA-FILM	$-0.0155 \pm 2 \times 10^{-4}$	$-0.0143 \pm 6 \times 10^{-4}$

Finally we note that the integrated Raman intensities for both E_{2g}^1 and A_{1g} modes have been found to decrease dramatically when the temperature $> 475\,°C$, presumably due to the decomposition of WS$_2$ films. Upon returning to room temperature, the films usually cannot return to the initial states. For the 1L-SiO$_2$ sample, the Raman intensities of the two phonon modes decrease by $\sim$40%; however, their peak positions remain almost the same as before, indicating that the bonding between the substrate and film for the CVD-grown samples is fairly robust and not altered significantly by the "annealing" process. For the transferred sample, similar to the transferred MoS$_2$ films [134], both Raman intensities and positions showed significant changes, indicating that the heating process modifies the bonding between the film and substrate, and thus the strain distribution over the film. The Raman spectra before and after temperature-dependent Raman measurements are shown in Figure 5.6.
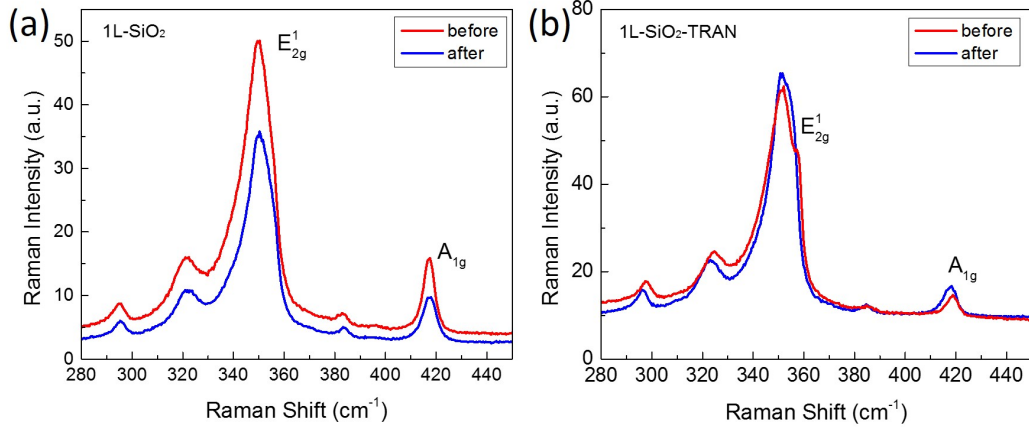
Figure 5.6: The Raman spectra before and after temperature-dependent Raman measurements for samples (a) 1L-SiO$_2$ and (b) 1L-SiO$_2$-TRAN.

5.3 Temperature Dependence of PL

The temperature dependence of PL are investigated for 1L-SiO$_2$ and 1L-SA-TRI samples, with a few representative PL spectra of each shown in Figure 5.7a-b. The peak energies as a function of temperature are plotted in Figure 5.7c. Similar to the trends observed in Figure 5.4b for the Raman shifts of E_{2g}^1, the PL peak energy shift for 1L-SiO$_2$ is significantly slower than 1L-SA-TRI, due to the release of the built-in tensile strain for the former. The reduced slope for 1L-SA-TRI at very high temperature ($> 300\,°$C) is due to increasingly significant thermal population of the higher states in the bands. The integrated PL intensities are shown in Figure 5.7d, showing thermal activated temperature quenching, starting approximately from room temperature. For 1L-SA-TRI, the well-known emission of Cd^{3+} centers from the sapphire substrate has been subtracted. Usually, the intensity of PL with increasing temperature can be fitted by Eq.(2.21) with one activation energy, which is suitable for the SiO$_2$ sample. However, for the sapphire sample, two activation energies are needed, thus the Eq.(2.21) can be modified as:

$$I(T) = \frac{I_0}{1 + A_1\exp(-E_{a1}/k_BT) + A_2\exp(-E_{a2}/k_BT)}, \qquad (5.2)$$

where E_{a1} and E_{a2} are the activation energies of the thermal quenching processes, and A_1 and A_2 are constants. For the SiO$_2$ sample, $A_2 = 0$. The fitting results are: for 1L-SiO$_2$, $E_{a1} = 0.40 \pm 0.01$ eV; for 1L-SA-TRI, $E_{a1} = 0.20 \pm 0.01$ eV and $E_{a2} = 1.51 \pm 0.06$ eV, respectively, with the fitting curves shown in Figure 5.7d. Temperature induced PL quenching in semiconductors is typically resulting from direct or indirect thermally activated non-radiative recombination processes associated with defects or impurities through emission of phonons. Activation energies as large as these values are unusual, which is largely because PL study is rarely performed in the temperature range much higher than RT to assess the potential process with such a large activation energy. At this stage, our understanding about defects and impurities in these 2D materials is very limited, thus, speculating the physical origins of these thermal quenching processes is premature. However, we would like to point out an important issue that could be particularly important to the 2D materials, that is, the interfacial effect involving carrier exchange between the 2D film and substrate through a thermal activation process. In fact, the magnitudes of the activation energies are comparable to the possible energy barriers between the film and substrate. Theoretical modeling based on first-principles techniques is needed to understand the film-substrate interaction that has yielded the effects reported here for electronic and vibration properties of the 2D materials.

5.4   Spatial Resolved Study on As-grown Monolayer WS$_2$ Triangles

In general, strain and doping are the two major causes to tune the optical properties of WS$_2$ monolayer, reflecting as the variation of Raman and PL spectroscopy. However, the origin of the induced strain and doping is most likely due to the growth and transfer processes. Similar to graphene, for transferred WS$_2$ samples, the transfer process introduces polymeric residues on top of the films, which can significantly dope the films, and hence modify the electronic properties. For CVD-grown samples, the quality of monolayer WS$_2$ depends on the precise control of growth conditions such
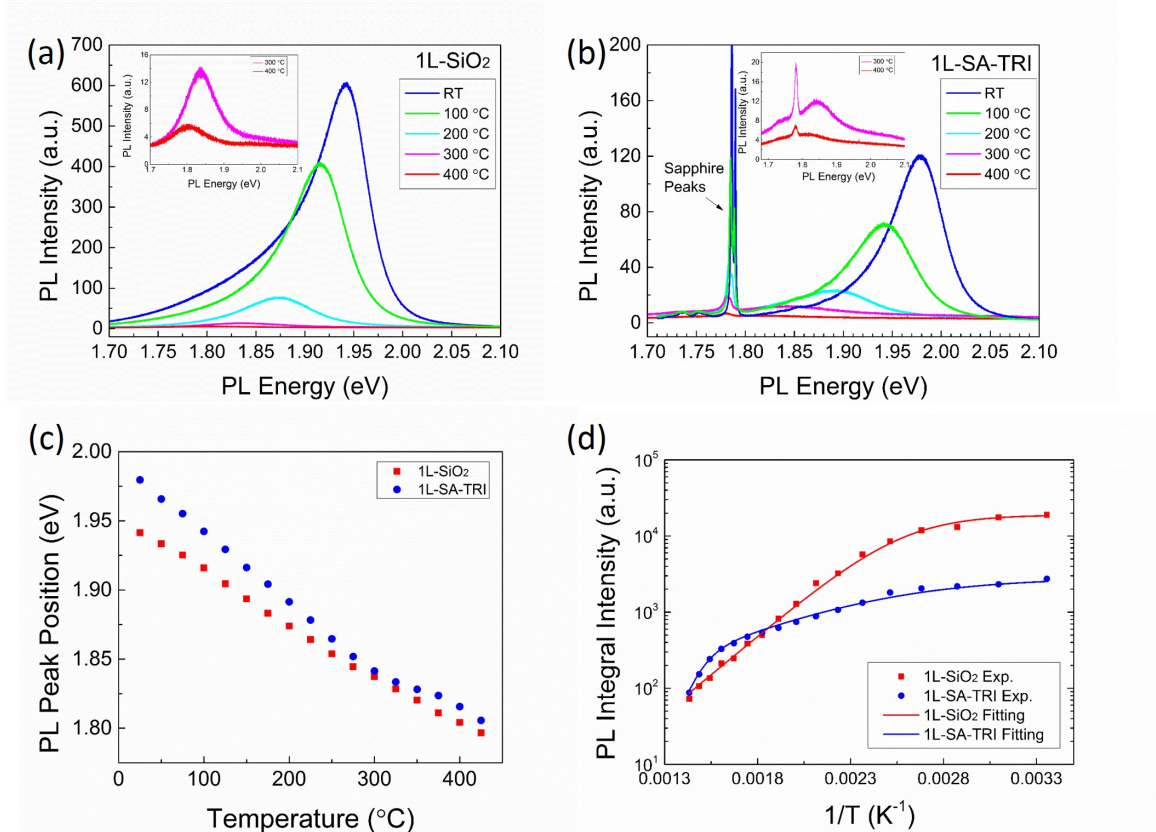
Figure 5.7: Temperature dependence of PL. (a)-(b) Representative PL spectra of (a) 1L-SiO$_2$ and (b) 1L-SA-TRI at particular temperatures. (c) Temperature dependence of PL peak energy for 1L-SiO$_2$ and 1L-SA-TRI samples. (d) Integral PL intensity of 1L-SiO$_2$ and 1L-SA-TRI at different temperatures.

as pressure, temperature, precursors, cooling rate and so on. Generally speaking, the CVD-grown samples are more defective than ME samples. The defects from growth process are another origin of doping. Furthermore, the interaction of monolayer WS$_2$ with the substrates, such as strain and charge transfer, plays a very important role in the optical properties of WS$_2$ monolayer as well.

WS$_2$ monolayers were originally synthesized on sapphire by CVD with the sulfurization of WO$_3$ precursors at a temperature of ~900 °C, involving the expanding and thinning of WS$_{2+x}$ flakes and eventually forming large monolayer WS$_2$ triangles (in the order of 10 µm) [50]. One can envision that the sulfurization process varies dramatically within the mostly monolayer triangle, because the growth time varies over

the triangle where the center area is longer while the edge shorter. Thus, the value of x may differ from one area to another, which can be either positive or negative. As a result, this could cause defects and structural deformation over the triangle. Moreover, it is reasonable to believe that the chemical bonding between the WS_2 film and substrate at the center area is stronger than that at the edge, because the growth or reaction time at the center area is longer. This spatial variation of the bonding strength can be the cause of non-uniform strain distribution over the triangle as well as doping concentration.

Figure 5.8 presents high spatial resolution Raman and PL mapping of the WS_2 triangle shown in Figure 5.1c, using 441.6 nm laser that is off-resonant with the B exciton bandgap to avoid the resonant Raman effect [135]. The Raman mapping data of both E_{2g}^1 and A_{1g} modes show weak intensity variation, less than 10%, over the triangle, with the interior region being stronger (Figure 5.8a-b). In contrast, the PL intensity mapping of the A exciton, as shown in Figure 5.8c, exhibits more significant variations, particularly in the regions near the edges with an average intensity about 10 times of the center. Figure 5.8g shows representative PL spectra from four locations (edge, general, center, and apex areas) labelled in Figure 5.8a. They differ not only in intensity but also in peak energy.

It is known that strain and doping effects play significant but distinctly different roles on Raman frequencies of E_{2g}^1 and A_{1g} modes [123, 136]. Under tensile strain both modes are expected to show a redshift, but more for E_{2g}^1 mode (i.e., with a larger deformation potential) [137]. Meanwhile A_{1g} modes is more sensitive to the doping effect due to the symmetry of conduction band edge state in monolayer WS_2, resulting in stronger electron-phonon coupling and thus more significant redshift or softening of A_{1g} mode [123, 136]. Figure 5.8d-e show the mapping data for the Raman frequencies of both E_{2g}^1 and A_{1g} modes. The regions with solid blue ellipses exhibit more blueshift than others, while dashed red ones more redshift. By examining the
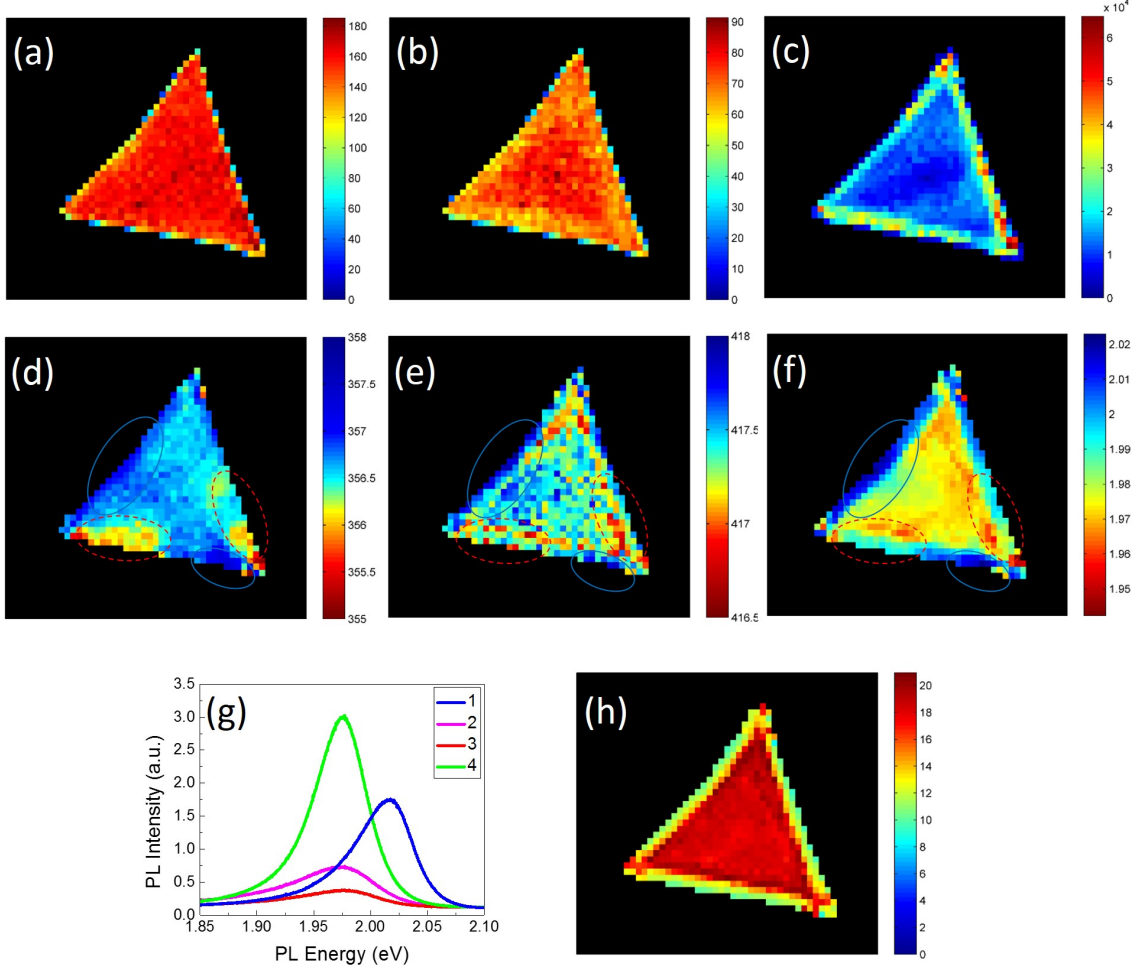
Figure 5.8: The Raman and PL mapping results of the monolayer WS$_2$ triangle on sapphire. (a)-(c) Intensity maps of (a) E_{2g}^1 mode, (b) A_{1g} mode, and (c) PL of the WS$_2$ triangle.(d)-(f) Maps of peak position of (d) E_{2g}^1 mode, (e) A_{1g} mode, and (f) PL. (g) PL spectra of locations 1-4. (h) PL width map of the WS$_2$ triangle.

two regions, a maximum frequency difference of E_{2g}^1 is measured to be $\sim$2.3 cm^{-1} and A_{1g} $\sim$1.5 cm^{-1}. Similar to Raman, PL is susceptible to strain and doping effects as well. The mapping of PL peak position (Figure 5.8f) shows a maximum difference in peak energy of $\sim$75 meV.

All these variations in peak positions and intensities of both Raman and PL cannot be explained simply by just one mechanism. However, here we propose that the variations of peak positions over the triangle may primarily arise from the variation in the epitaxial strain that is introduced during growth process. The film grown on

sapphire tends to be under tensile strain due to the difference in thermal expansion between the film and the substrate. During the expanding phase of the growth, it is quite possible that the strain distribution over the large triangle will not be uniform due to the geometry of the film and interaction with the substrate. This non-uniform strain, i.e. localized strain, can explain the variations of Raman frequencies of both E_{2g}^1 and A_{1g} modes, as well as the PL peak position.

To estimate quantitatively the strain induced in the film, we carried out DFT calculations for the strain dependent bandgap and phonon frequencies for uniform strain [138]. The results are shown in Figure 5.9. The deformation potentials for uniform tensile strain are respectively 4.4 cm^{-1}/%, 1.7 cm^{-1}/%, and 140 meV/% for E_{2g}^1, A_{1g}, and band gap E_g, respectively. Using the calculated deformation potentials and experimentally measured shifts, the values of maximum strain difference over the triangle are estimated from E_{2g}^1 mode to be $\sim$0.53%, and from PL $\sim$0.54%, which match very well with each other. However, from A_{1g} mode the estimated strain would be $\sim$0.88%, implying that strain might not be the only mechanism for the redshift. Therefore, we suggest that the doping effect in the film might contribute partially to the redshift of A_{1g}.
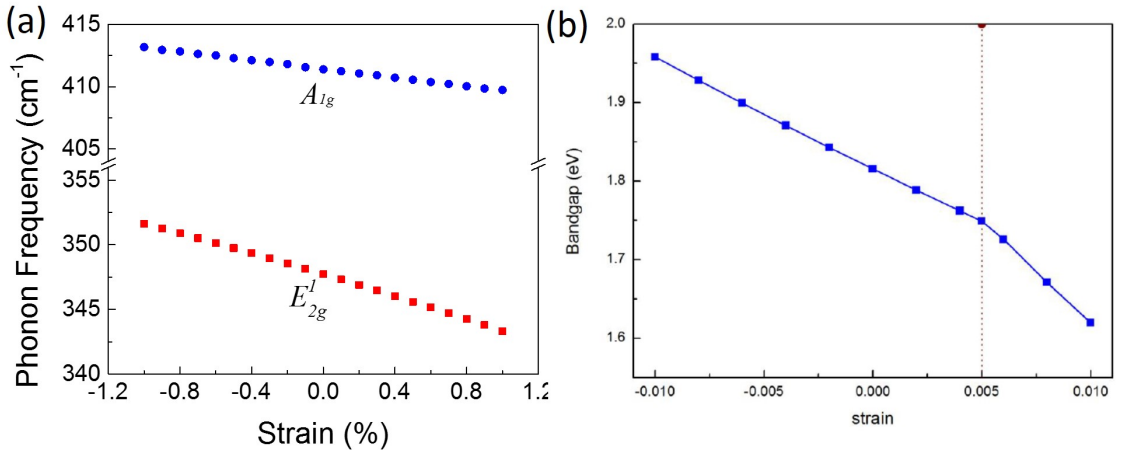
Figure 5.9: DFT calculation of strain-induced Raman and PL shifts. (a) DFT-calculated phonon shift as a function of strain for E_{2g}^1 and A_{1g} modes. (b) The band gap of monolayer WS$_2$ as a function of uniform strain.

Monolayer TMDs are intrinsically n-type doped due to substrate charge transfer [114], and intrinsic structural defects such as mono-sulfur vacancy (V_S) and di-sulfur vacancy (V_{S2}) which are originated from growth process [124]. These sulfur vacancies have been directly observed by scanning transmission electron microscopy (STEM) in monolayer MoS_2 and WS_2 [139,140]. They are expected to behave as in-gap levels which may quench the band edge PL [141]. The n-type doping caused by shallow donors will lead to the formation of side bands with emission energy lower than that of the neutral exciton and thus the broadening of the overall PL linewidth. However, the distribution of doping concentration over one individual WS_2 triangle is not uniform as a result of the perturbations during the growth process. As we mentioned above, defects are formed during growth, which are mainly sulfur vacancies, and hence n-type doping. Doping or defect, as is known, is one of the origins of PL quenching. In Figure 5.8f, the PL intensities of central area are weaker than those of apex and edge areas. In order to further explain this non-uniform distribution, the spatial variation of the overall PL linewidth is shown in Figure 5.8h, revealing that the linewidth at the edge area is the smallest over the WS_2 sample. Because a smaller linewidth indicates a lower doping/defect concentration, the linewidth distribution suggests that at the edge area the doping concentration is smaller than the central area. On the other word, the central area is more defective. The better quality, consequently, is one of the reasons of the higher PL intensity at the edge, as shown in Figure 5.8g. Another origin of higher PL intensity at the edge is the less charge transfer between the film and the substrate. On the surface of sapphire, the surface states originating from the Al-O bond terminates and dangling bonds take over, conventionally whose charge density could be very high [142]. Electrons are subjected to be trapped in these surface states, because the Fermi levels of sapphire and WS_2 are supposed to be at the same height in an equilibrium state [143]. Therefore, the photo-generated electrons in PL measurements of WS_2 film will lift up the Fermi level of WS_2, forming

a positive potential between the surface states and the WS_2 film. As a result, the electrons tend to escape from WS_2 film to substrate, hence the quenching of PL. Due to the fact that shorter growth time at the edge area results in weaker bonding at the interface between sapphire and WS_2 than those at the central area, it is reasonable to believe that the charge transfer at the edge is weaker, and consequently the radiative recombination rate at the edge is higher or the PL is stronger. In short, besides strain effect to cause the shift of PL peak position, the doping effect from impurities and the charge transfer between substrate and WS_2 film are the reasons to cause the variation of PL quantum yield.

In order to further investigate the effects of strain and doping/defects mentioned above on the properties of WS_2, WS_2 triangles were transferred to a silicon wafer coated with 300 nm thick SiO_2 layer. Holes of different diameters were etched into the wafer. As the optical image is shown in Figure 5.10a, a hole of $\sim$14 µm in diameter was covered by a WS_2 triangle. The PL intensity mapping of the WS_2 triangle is shown in Figure 5.10b. The PL intensity of the suspended region is more than that of the supported region by a factor of 2–10. This enhancement cannot be simply explained by an increase of the optical absorption cross section, because the Raman intensity, which has the optical absorption cross section, shows a small decrease (Figure 5.10f). Figure 5.10c-d shows mapping images of PL peak energy and E_{2g}^1 frequency. Both PL peak energy and E_{2g}^1 frequency at suspended region, in general, exhibit a redshift with respect to those at supported region, suggesting that the suspended WS_2 undergoes tensile strain. The maximum difference of PL energy and E_{2g}^1 frequency between supported and suspended regions is $\sim$45 meV and $\sim$2.0 cm^{-1}, which correspond to the strain of $\sim$0.34% and $\sim$0.45%, respectively. The difference between the two estimated strain values can be due to the doping effect in the film.

Figure 5.10e-f show the PL and Raman spectra of locations 1 and 2 labelled in
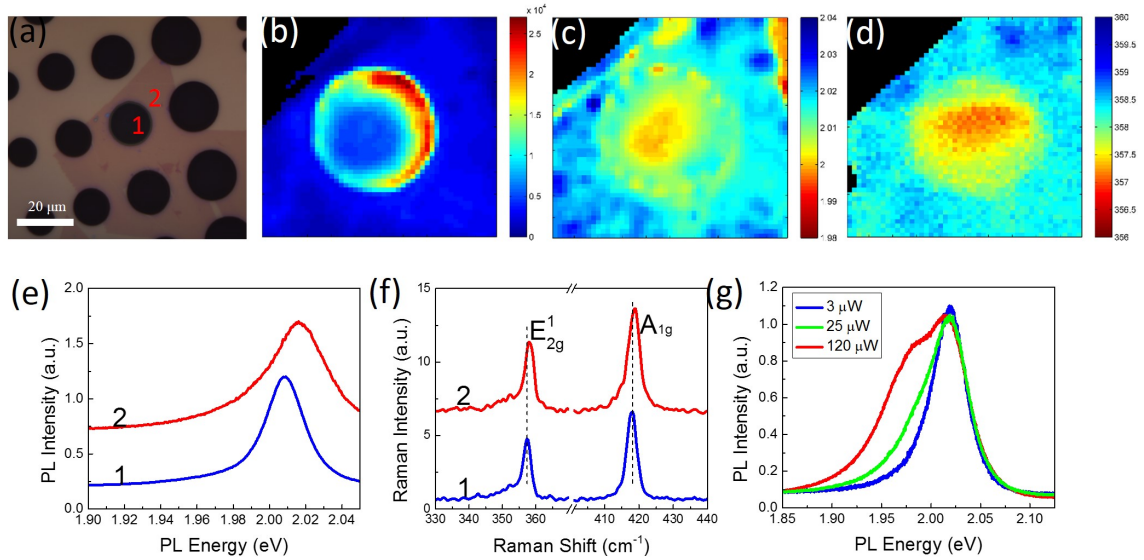
Figure 5.10: The optical characterizations of WS$_2$ triangles after transferred. (a) Optical image of the transferred WS$_2$ on SiO$_2$/Si substrate etched with holes. (b) PL intensity map of an area of 24 µm×24 µm. (c)-(d) The maps of peak position of (c) PL and (d) E_{2g}^1 mode. (e)-(f) PL and Raman spectra of locations 1 and 2. (g) Laser power dependence of PL.

Figure 5.10a. The PL peak energy and the E_{2g}^1 frequency of location 2 are 2.017 eV and 356.8 cm^{-1}, respectively. The PL peak energy difference between locations 1 and 2 is 8 meV, corresponding to a strain difference of 0.06%, while the E_{2g}^1 frequency 0.7 cm^{-1} to 0.16%. The origin of the discrepancy of strain values could be the doping effect. One source of doping is the intrinsic impurities and the polymeric residues from growth and transfer processes, which could significantly modify the electronic bands of WS$_2$ monolayer, at either suspended or supported regions. However, at supported region the charge transfer between the film and the substrate becomes more significant than the influence from impurities and residues, leading to the quenching of photo-generated free carriers and hence lower PL intensity. Meanwhile, due to the charge transfer the doping in supported region is higher than that in suspended region, which usually leads to narrowing in band gap energy, i.e. redshift in PL peak energy. Therefore, the real band gap of location 2 can be re-estimated by the strain difference extracted from E_{2g}^1 mode, which is 2.031 eV (610.5 nm). Moreover, a side peak with

a lower energy is observed in most PL spectra, which can be assigned as A^- trion peak rather than defect or impurity [115]. Because the lower-energy peak increases with increasing power which confirms that this peak is correlated to A^-, as shown in Figure 5.10g. The dissociation energy of A^- with respect to A can tuned by varying the power of the 532 nm excitation. With increasing power the trion dissociation energy increases due to the increase in carrier density, i.e. Fermi energy. For the spectra in Figure 5.10(g), the trion dissociation energy is estimated to be $\sim$43 meV at the laser power of 120 µW, while it decreases with decreasing power, e.g. to $\sim$24 meV at the power of 3 µW.

5.5   Conclusions

In conclusion, Raman and PL spectroscopies have been used to investigate the interplay of strain, doping and defects of CVD as-grown and transferred CVD-grown WS_2 monolayers. High-temperature PL and Raman studies were also performed on CVD-grown epitaxial monolayer WS_2 on SiO_2/Si and sapphire substrates. The interaction between the 2D film and substrate was shown to depend on substrate type for the as-grown samples and film-substrate bonding between the as-grown and the transferred samples. At RT, the PL intensity of monolayer WS_2 on SiO_2 was found to be much stronger than that on the sapphire substrate under both 532 and 441.6 nm excitation. The TEC mismatch between the thin-film and SiO_2/Si substrate generated a significant amount of strain after the film was cooled down to RT, manifesting itself as a bandgap shift, strong intensity modification in resonant Raman scattering, and large non-linearity in the temperature coefficient of the vibration mode frequency. The effects were minimal for the sapphire substrate. These effects, which are associated with the built-in strain, are inherent properties of the directly grown 2D films. However, this depended upon the specific substrate used. A significant difference existed in the states of the built-in strain between the directly grown and the transferred films, even on the same type of substrate. The in-plane vibration mode, E_{2g}^1,

was more sensitive to the strain effect, whereas the out-of-plane vibration mode, A_{1g}, was more sensitive to the film-substrate bonding or the film morphology. Because of the strong electron-phonon coupling of the A_{1g} mode as dictated by symmetry, a transferred film without proper thermal annealing was expected to have an inferior carrier mobility. The intrinsic temperature coefficients for the E_{2g}^1 and A_{1g} modes in monolayer WS$_2$ were determined to be: $\chi(E_{2g}^1) = -0.0142 \pm 2 \times 10^{-4}$ cm^{-1}/K, derived from the transferred film on SiO$_2$; and $\chi(A_{1g}) = -0.0130 \pm 9 \times 10^{-5}$ cm^{-1}/K (lower bound), derived from the as-grown film on SiO$_2$. These values were somewhat smaller than the corresponding ones in MoS$_2$: $\chi(E_{2g}^1) = -0.0221 \pm 9 \times 10^{-4}$ cm^{-1}/K, and $\chi(A_{1g}) = -0.0197 \pm 9 \times 10^{-5}$ cm^{-1}/K. For all other cases, the temperature coefficients were affected by the substrate to different extents, but this effect was most severe for the film grown on SiO$_2$ with $\chi(E_{2g}^1) = -0.0100 \pm 3 \times 10^{-4}$ cm^{-1}/K. Therefore, the temperature-dependent Raman investigations provided an effective tool for investigating the epilayer-substrate interaction. Additionally, high-temperature PL studies on monolayer WS$_2$ revealed thermal quenching processes with large activation energies of $E_{a1} = 0.40$ eV for the film grown on SiO$_2$ and $E_{a1} = 0.20$ eV and $E_{a2} = 1.51$ eV for the film grown on sapphire.

With mapping technique of Raman and PL spectroscopy, the strain distribution over the monolayer WS$_2$ triangle has been examined nondestructively. Through DFT simulation, the maximum difference in strain within a single triangle has been estimated quantitatively to be of $\sim$0.53% based on the shift of E_{2g}^1 mode for CVD-as-grown WS$_2$ film on sapphire. The main origin of the strain is the difference in TEC between WS$_2$ and the supporting sapphire substrate. During the cooling-down process of the growth, this difference of TEC in between introduces the strain to the film, which is observed to be non-uniform. In conjunction with PL mapping, similar maximum strain difference has been estimated to $\sim$0.54% based on the shift of PL peak energy. Besides the strain effect, the effects of both doping and defects, which

are from the growth and transfer processes, play significant roles in PL, resulting in the suppression of A-exciton peak for both CVD-grown and transferred WS_2 samples. In particular, the suspended WS_2 film shows more than 10 times stronger PL intensity than the supported WS_2 film, suggesting the involvement of charge transfer between the substrate and the film. Moreover, the A- trion peak accompanied by A-exciton emission has been observed, with a dissociation energy of $\sim$43 meV at the laser power of 120 µW.

CHAPTER 6: TEMPERATURE DEPENDENCE OF RAMAN SCATTERING IN THIN-FILM BLACK PHOSPHORUS

6.1   Black Phosphorus Sample Preparation and Its Anisotropic Effects

6.1.1   Sample Preparation and Characterization

High-quality BP crystals were purchased from Smart-Elements. BP flakes were obtained by mechanical exfoliation onto a silicon substrate coated with a 300 nm SiO_2 layer. Since BP is very sensitive to ambient environment, the sample was transferred into a heating chamber purging with N_2 gas for temperature dependent Raman measurements. The flow rate of N_2 was low enough not to cause sample cooling. After Raman measurements were finished, tapping mode AFM was carried out to determine the thickness of exfoliated BP flakes. Figure 6.1a-d shows the optical images of four exfoliated samples, labelled as S1-S6. An AFM image containing samples S1 and S2 is also shown in Figure 6.1e, and the thickness of S1 is measured to be $\sim$25 nm while that of S2 $\sim$10 nm ($\sim$20 layers). Samples S5 and S6 are in the same flake, but S5 is suspended on a hole etched into SiO_2 substrate. The diameter of the hole is 10 µm. The thickness of samples S5 and S6 is $\sim$70 nm, determined by AFM.
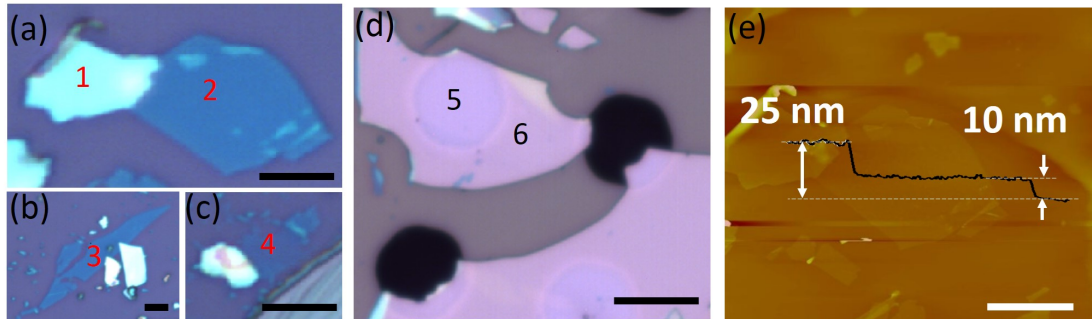
Figure 6.1: Optical images and an AFM image of BP films. The scale bar is 10 µm.

The unit cell of black phosphorus has four phosphorus atoms, and the space

group of bulk BP is D_{2h}. There are 12 lattice vibrational modes at Γ point, which can be expressed as following [144]:

$$\Gamma = 2A_g + B_{1g} + B_{2g} + 2B_{3g} + A_{1u} + 2B_{1u} + 2B_{2u} + B_{3u}, \qquad (6.1)$$

among which six modes are Raman-active, two A_g (including A_g^1 and A_g^2), one B_{1g}, one B_{2g}, and two B_{3g}. However, only A_g^1 (out-of-plane mode), B_{2g} (in-plane mode along zigzag), and A_g^2 (in-plane mode along armchair) modes can be detected by Raman with back-scattering geometry according to symmetry selection rule (Figure 6.2a). The Raman spectra of S1-S4 samples, measured with the same laser power of $\sim$150 µW at room temperature, are shown in Figure 6.2. Three typical Raman peaks corresponding to A_g^1, B_{2g}, and A_g^2 are observed with their peak positions at $\sim$362, $\sim$439, and $\sim$467 cm^{-1}, respectively. These peaks are fitted with a Lorentzian function to extract the linewidth. According to the intensity of silicon peak at 520 cm^{-1}, we can determine the thickness order of the four samples: S1 > S2 > S3 > S4. Using the intensities of Si peak, we are able to estimate the thickness of S3 to be $\sim$6 nm and S4 $\sim$3 nm. The peak position of A_g^2 mode shows a blueshift in frequency with decreasing thickness, while that of A_g^1 mode a redshift, and B_{2g} mode almost no change. This thickness dependence of Raman frequency in BP is similar to that of TMDs where in-plane mode shows a blueshift and out-of-plane mode redshift, which is attributed to the changes in interlayer interaction with thickness [109, 111]. Interestingly, their Raman intensities do not vary monotonically with thickness, with S2 exhibiting the strongest Raman intensity. This anomalous thickness-dependent behavior can be explained by optical interference with the model used in graphene and MoS$_2$ [145–147]. The simulated results show that the film of $\sim$20 layers exhibits the strongest Raman signal over a thickness range of 1-100 layers, which is in reasonably good agreement with experimental results (Figure 6.2b).
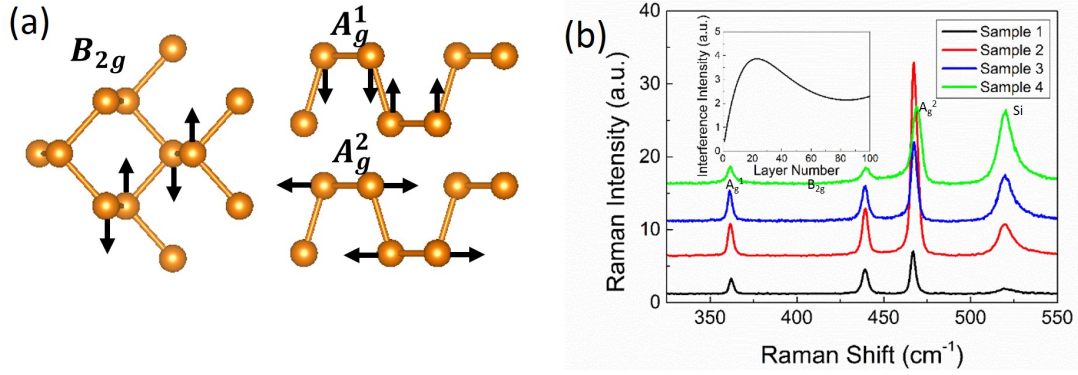
Figure 6.2: Raman spectra of all the BP samples. (a) Three major Raman modes of BP. (b) Raman spectra of all the four BP samples. The inset is a simulation of interference effect as a function of BP thickness.

6.1.2 Anisotropic Effect of Raman Spectroscopy

Due to the puckered honeycomb structure of BP, BP exhibits anisotropy between the two in-plane primary axes x and z, which in turns will lead to its in-plane multitudinous properties. Angle-resolved polarized Raman spectroscopy is a convenient and nondestructive method to identify the crystalline orientation of BP. According to the symmetry selection rule, only A_g^1, B_{2g}, and A_g^2 modes can be detected when the incident laser perpendicular to the sample surface. The Raman tensors of these three modes are listed as following [144]:

$$\mathcal{R}(A_g) = \begin{pmatrix} a & 0 & 0 \\ 0 & b & 0 \\ 0 & 0 & c \end{pmatrix}, \quad \mathcal{R}(B_{2g}) = \begin{pmatrix} 0 & 0 & e \\ 0 & 0 & 0 \\ e & 0 & 0 \end{pmatrix}, \tag{6.2}$$

A_g^1 and A_g^2 modes have the same expression of Raman tensor but with different values of a, b and c. As shown in Figure 6.3a, x and z are the crystal orientation with x in the zigzag direction, and z armchair direction, and e_i and e_s are the polarization vectors of incident laser and scattered light, respectively, which are parallel with each other in our experiment setup. The angle θ that is between the laser polarization

vector (e_i) and the armchair direction (z) can be tuned by rotating the sample. The laser is incident along y direction and its polarization is in xz plane. Thus, in the parallel polarization configuration, the vectors e_i and e_s can be written as:

$$e_i = \begin{pmatrix} \sin\theta & 0 & \cos\theta \end{pmatrix}, \quad e_s = \begin{pmatrix} \sin\theta \\ 0 \\ \cos\theta \end{pmatrix}. \tag{6.3}$$

According to Eq.(2.9) the intensity of a given Raman mode, I, is proportional to $|e_i \cdot \mathcal{R} \cdot e_s|^2$; therefore, the Raman intensity of Ag (including A_g^1 and A_g^2) and B_{2g} modes under parallel polarization configuration can be written as:

$$I(A_g) \propto \left(a\sin^2\theta + c\cos^2\theta \right)^2,$$
$$I(B_{2g}) \propto \left(e\sin^2 2\theta \right)^2. \tag{6.4}$$

Apparently, when the laser polarization direction is parallel ($\theta = 0°$) or perpendicular ($\theta = 90°$) to the armchair direction, A_g mode shows local maximum intensities (c^2 or a^2), while B_{2g} mode is forbidden. When $\theta = 45°$, B_{2g} mode reaches its maximum, and over 360° there are four maxima of the same intensity with a period of 90°.

Figure 6.3b shows the polarized Raman spectra of BP samples S6 at different angles of θ from 0° to 180° under parallel polarization configuration. To reveal this behavior, the polar plots of the fitted peak intensities of all the three Raman modes as a function of sample rotation angle θ are shown in Figure 6.3c-e, where the $\theta = 0°$ direction is appoximately aligned with the z axis, based on the assumption that $c > a$ for A_g^2 mode [55]. It can be clearly seen that different Raman modes show different periodic variation of their intensities over 360° rotation. The results qualitatively match the predicted angular dependences of Eq.(6.4) quite well. For B_{2g} mode, as expected there are four maxima with same intensity. It is worth noting that, for A_g^2
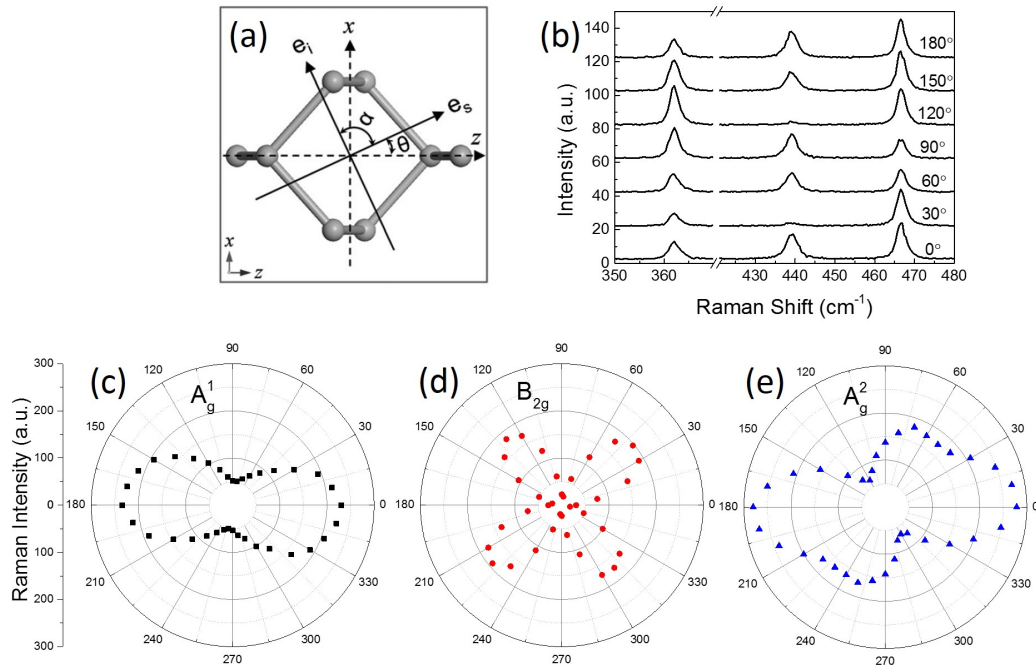
Figure 6.3: Anisotropic nature in Raman spectroscopy of BP. (a) The configuration in the polarized Raman measurements. (b) Representative Raman spectra of BP film with different polarization angle. (c)-(e) Polar plots of the Raman intensities for the three Raman modes of sample S6: (c) A_g^1, (d) B_{2g}, and (e) A_g^2). Panel a reproduced from J. Wu et al. [55].

mode, there are two different local maxima, which is attributed to the different values of a and c in the Raman tensor. The value of a has been shown to be greater than that of c [55], thus the A_g^2 mode reaches a relative smaller local maximum intensity when the laser is polarized in the x (zigzag) direction. When the sample is rotated 90°, where the z direction (armchair) is parallel to the laser polarization direction, a relatively larger local maximum intensity of A_g^2 mode can be obtained. Therefore, with the results of angle-resolved Raman spectroscopy, the optical anisotropic nature of BP has been demonstrated, and most importantly, the crystalline orientation of the sample can be identified rapidly and nondestructively. Even though B_{2g} and A_g^2 are found to follow the predicted angular dependences, A_g^1 (Figure 6.3) seems to not obey the predicted dependence. The reason is unclear at this time. We note that the

angular dependence could be affected by the interference effect of the substrate to a degree depending on the magnitude of the anisotropy between a and c.

6.2   Temperature Dependence of Raman in BP

Temperature dependent Raman measurements were carried out on all the six samples for temperature up to $325\,°\mathrm{C}$. With increasing temperature, all Raman modes are expected to show a significant redshift, as shown in Figure 6.4 with representative spectra of S2 and S4 at different temperatures, respectively. The temperature dependence of A_g^1, B_{2g} and A_g^2 Raman frequencies are plotted in Figure 6.4a-c, and fitted to Eq.(3.1). As discussed earlier, the change of Raman frequency with temperature can be caused by various anharmonic effects described by Eq.(4.2).
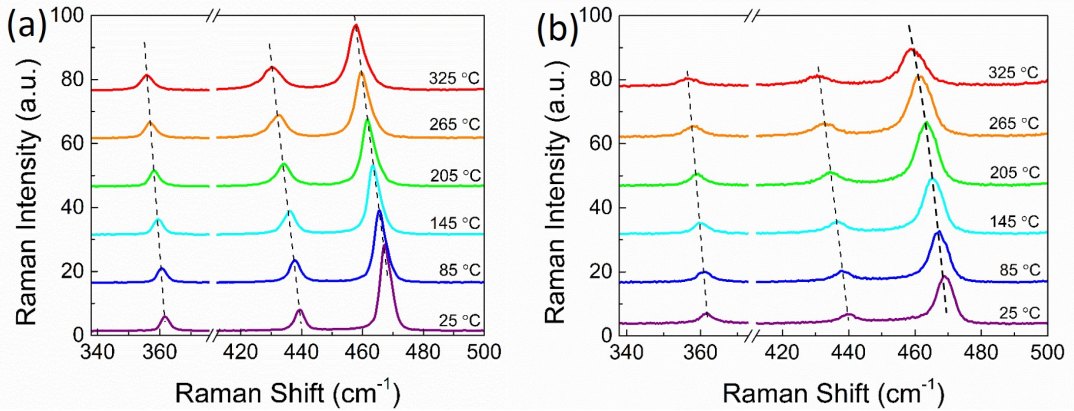
Figure 6.4: Representative Raman spectra for (a) S2 and (b) S4 at different temperatures.

The temperature coefficients of all the six samples are listed in Table 6.1. Comparing the temperature coefficients of samples S1-S4, the temperature coefficients of all the three modes in general decrease with decreasing thickness. As the thickness decreases, the BP film is more sensitive to its environment, such as substrate, which could lead to modifications of its intrinsic properties. All the four BP samples are held by SiO_2/Si substrate with relatively weak bonding, and the TEC of SiO_2 ($\sim 0.5 \times 10^{-6}/°\mathrm{C}$) is much smaller than that of BP. The TEC's of exfoliated BP flakes along armchair and zigzag directions are $93.2 \times 10^{-6}/°\mathrm{C}$ and $90.3 \times 10^{-6}/°\mathrm{C}$ [148],
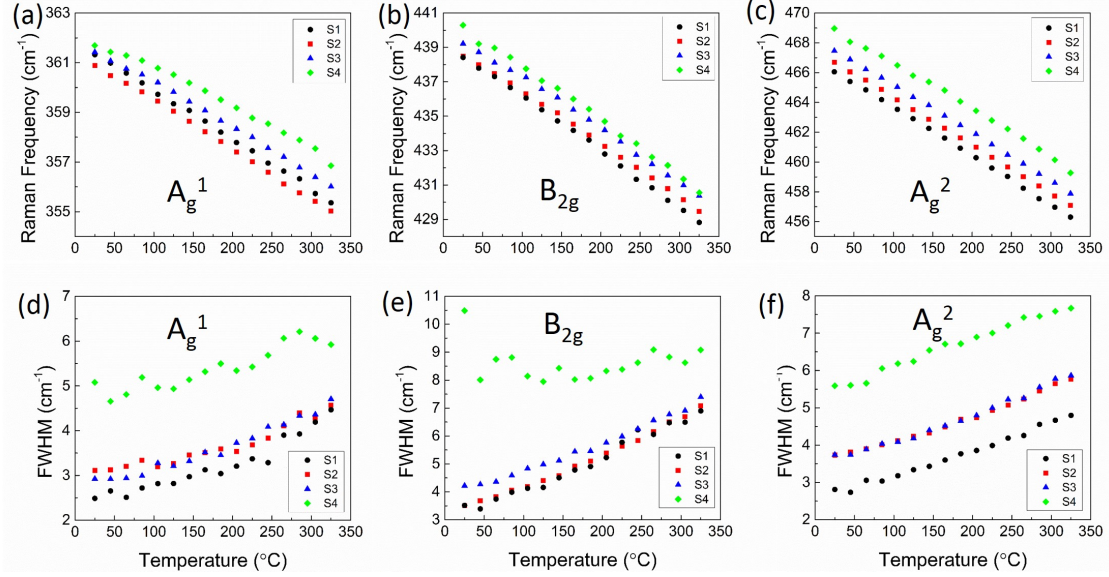
Figure 6.5: Temperature-dependent Raman spectroscopy of all the four BP samples (S1-S4). (a)-(c) Temperature dependences of Raman frequencies of (a) A_g^1, (b) B_{2g} and (c) A_g^2 modes over a temperature range from RT to $325\,°C$ in samples S1-S4. (d)-(f) Temperature dependences of FWHMs of (d) A_g^1, (e) B_{2g} and (f) A_g^2 modes in all the four samples.

respectively. With increasing temperature, the difference in TEC between the film and the substrate will introduce compressive strain to the film, which effectively reduce the intrinsic thermal expansion of lattice hence the redshift of Raman frequency. With increasing thickness, this effect tends to become weaker. Thus, the thicker film like S1 is less susceptible to the substrate effect, leading to larger temperature coefficients than other thinner samples. Additionally, it is quite possible that ripples were introduced to BP films during the transfer process, showing a non-planar morphology especially when the film becomes thinner. The morphologic variation of the film, in particular for very thin film, is the main origin of the strain. The non-uniform morphology of the film can affect the temperature dependence significantly on both in-plane and out-of-plane vibrational modes, showing nonlinear temperature dependence. Among the four BP samples, all the three modes of the thinnest sample S4 clearly exhibit stronger nonlinear temperature dependence than the other three samples. The nonlinear temperature dependence of S4 originates from the rearrangement

of the film morphology as the strain due to the TEC difference between the film and the substrate changes with increasing temperature. For thicker films, the morphology is expected to be more planar than other samples; thus, the temperature dependence is more linear.

The FWHM of all the three modes increases with increasing temperature as shown in Figure 6.5d-f. At RT, the FWHM increases with decreasing thickness of BP film. For S4, the FWHM is almost double of other three samples. For instance, the FWHMs of S1 and S4 for A_g^1 mode are 2.5 and 5.1 cm^{-1}, respectively. This behavior can be explained by the effect related to variation in film morphology as discussed above. On increasing the thickness of the films, the effect of substrate is getting weaker and film morphology more uniform, hence smaller FWHM. For each individual sample, with increasing temperature the FWHM increases. The broadening of Raman peaks typically involves the decay of an optical phonon into two acoustic phonons with the conservations of both momentum and energy. However, the strain induced by the TEC mismatch coupled with the morphology inhomogeneity may also contribute to the broadening of Raman linewidth. It is worth noting that the decomposition of BP films is observed to occur at ~350 °C in N$_2$ environment, manifested as a major reduction in Raman intensity and the sublimation of BP under visual observation. This decomposition temperature is lower than reported value of 400 °C under vacuum probed by other techniques [148].

Table 6.1: Temperature coefficients of A_g^1, B_{2g} and A_g^2 modes of samples S1-S4, suspended and supported BP flakes.

	A_g^1(cm^{-1}/K)	B_{2g}(cm^{-1}/K)	A_g^2(cm^{-1}/K)
Sample 1 (25 nm)	−0.0198	−0.0323	−0.0327
Sample 2 (10 nm)	−0.0198	−0.0304	−0.0324
Sample 3 (6 nm)	−0.0182	−0.0300	−0.0320
Sample 4 (3 nm)	−0.0158	−0.0315	−0.0312
Suspended (70 nm)	−0.0220	−0.0344	−0.0349
Supported (70 nm)	−0.0191	−0.0312	−0.0318

6.3   Thermal Conductivity of Black Phosphorus (BP)

In order to investigate the influence of substrate effect on temperature dependence, the temperature dependent Raman of S5, which is suspended, is compared to that of S6 that is supported. Figure 6.6a shows Raman spectra collected from the suspended (center of the hole) and supported regions at RT. Two noticeable differences are observed: (1) all the three modes in the suspended region are redshifted compared to supported region, due to heating as a result of lower effective thermal conductivity; (2) the Raman intensity of suspended region is smaller than that of the supported region, due to lacking of the enhancement of the optical interference effect [147]. The temperature dependence of the three Raman modes is shown in Figure 6.6b-d, and the temperature coefficients are listed in Table 6.1. The temperature coefficients of all the three modes in suspended region are greater in magnitude than those in supported region by $\sim$0.003 cm^{-1}/K ($\sim$10–15%). The difference cannot be explained by the residual laser heating effect, because the additional redshift induced by laser heating will not increase (but likely reduce) with increasing temperature. However, with increasing temperature the supported BP film experiences compressive strain due to the TEC difference, leading to a blueshift which reduces the redshift caused by heating. For the suspended film, the potential strain caused by the larger thermal expansion of BP could be released through sagging of the film around the edge of the hole, resulting in a nearly strain-free state in the suspended region.

Even though the laser power used is as low as possible not to damage the BP films, it will heat up the sample to cause a temperature rise. Laser power dependent Raman studies are utilized to estimate this temperature rise. The changes in the Raman spectra of suspended BP with different laser powers are shown in Figure 6.7a. With increasing power, the peak positions of all the three modes redshift, indicating the local temperature rises. The frequency shifts are shown in Figure 6.7b-d, exhibiting that the slopes of the suspended region for all the three modes are
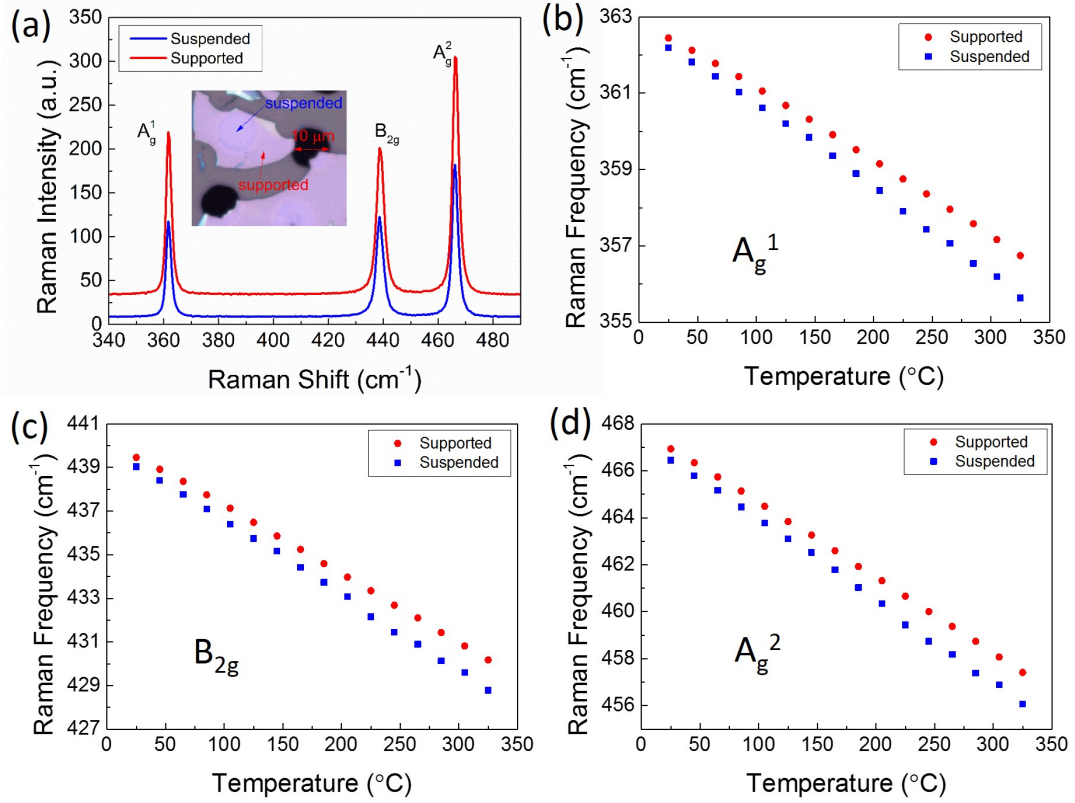
Figure 6.6: Temperature-dependent of Raman spectroscopy of the BP flake in Figure 6.1d. (a) Raman spectra collected from suspended (blue) and supported (red) regions; inset: optical image of suspended BP flake. (b)-(d) Temperature dependences of Raman frequencies of (b) A_g^1, (c) B_{2g} and (d) A_g^2 modes in suspended and supported regions.

larger than those of supported region by a factor of ~ 2.2 and the slope $\partial\omega/\partial P$ of A_g^1 mode is much smaller than those of the other two modes. The power used in the temperature-dependent Raman measurements was ~ 0.5 mW, so we can calculated the temperature increase ΔT by the expression: $\Delta T = \Delta P \cdot (\partial\omega/\partial P)/(\partial\omega/\partial T)$, where ΔP is the highest laser power used and $\partial\omega/\partial T$) the temperature coefficient. The temperature increases in suspended and supported regions are estimated to be ~ 22 and $\sim 12\,°C$ at $P = 0.5$ mW, respectively.

Finally, using the temperature and power dependent results obtained above, we can estimate the average thermal conductivity of BP. Because of the anisotropic nature of BP, the thermal conductivities are expected to be different between the
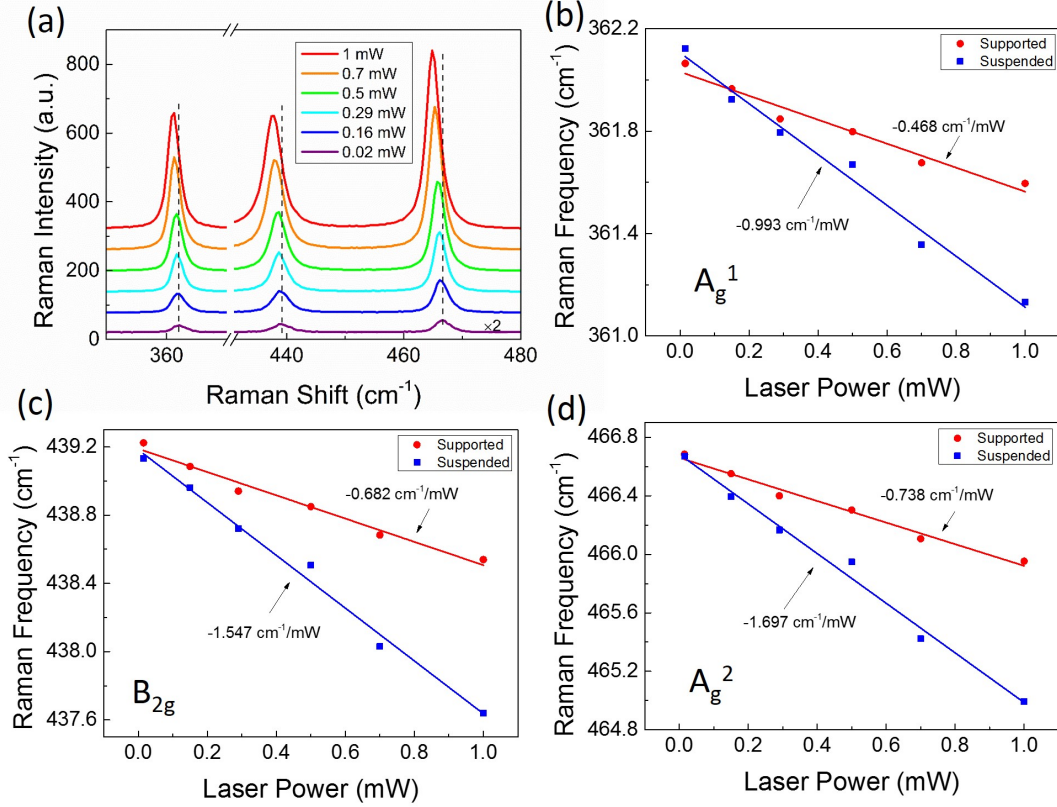
Figure 6.7: Laser power dependence of Raman spectroscopy for the BP flake in Figure 6.1d. (a) Raman spectra collected with different laser powers in suspended region. (b)-(d) Laser power dependences of Raman frequencies of (b) A_g^1, (c) B_{2g} and (d) A_g^2 modes in suspended (blue) and supported (red) regions, including linear fits of experimental data.

zigzag armchair direction as k_{zig} and k_{arm}, and the average thermal conductivity can be viewed as $k = \sqrt{(k_{zig}k_{arm})}$. Considering the thermal diffusion through an enclosed cylindrical surface in the suspended region, the average thermal conductivity can be evaluated approximately using the formula below that has been developed for 2D materials [149, 150]:

$$k = f\chi \frac{1}{2\pi h} \left(\frac{\partial \omega}{\partial P} \right)^{-1}, \tag{6.5}$$

where χ is the Raman temperature coefficient, h the thickness of the film, and f a reduction factor due to incomplete absorption of laser power. To the first order approximation, $f = g(1 - R)[1 - \exp(-\alpha h)]$, where g, R, and α are interference

enhancement factor, reflectance of the BP top surface, and absorption coefficient of BP, respectively, which are all polarization dependent due to anisotropy. The crystalline orientation was determined by analyzing polarized Raman data [55], and the angle between the laser polarization and the zigzag direction was found to be $\sim 30°$. The absorption coefficients and reflectance values were estimated for 532 nm with polarization in zigzag and armchair directions to be $\sim 5.5 \times 10^4$ cm^{-1} and $\sim 1.6 \times 10^5$ cm^{-1}, $\sim 43.5\%$ and $\sim 44.4\%$, respectively [151, 152]. Thus, the f's are estimated to be 0.23 and 0.21 for suspended and supported BP, respectively. Therefore, for the suspended region, the estimated average thermal conductivities are 16.1, 16.2, and 15.0 W/mK, using the parameters of A_g^1, B_{2g} and A_g^2, respectively. These values, averaged to $k_{susp} = 15.8$ W/mK, are in reasonable agreement with $k_{arm} \sim 20$ W/mK, $k_{zig} \sim 40$ W/mK reported for BP thicker than 15 nm [151]. For the supported region, strictly speaking, Eq.(6.5) is not applicable. However, we may treat the substrate effect as a surface modification to the film, and still use the equation to get an effective thermal conductivity. The results are 27.6 (A_g^1), 30.9 (B_{2g}), and 29.1 W/mK (A_g^2), respectively, and the average $k_{supp} = 29.2$ W/mK. Although the thermal conductivity of SiO$_2$, ~ 1.4 W/mK [153], is much larger than N$_2 \sim 0.025$ W/mK [154], it is still much smaller than that of BP. The significant enhancement in thermal conductivity seems to suggest that the supporting substrate plays a more subtle role than merely as a medium with a different thermal conductivity, for instance, the interface charges might significantly affect the thermal conductivity. This higher thermal conductivity at supported region can also explain the smaller temperature rise under high laser power in the supported region compared to suspended region. The obtained thermal conductivities for BP films are comparable to those for TMDs [119, 150], but significantly smaller than graphene [149]. The observed substrate effect is also applicable to other 2D materials.

6.4   Conclusions

Angle-resolved Raman spectroscopy reflects the anisotropic nature of BP, which can be used as a non-destructive technique to determine the crystalline orientation. Temperature-dependent Raman scattering has been carried out to investigate the temperature effects in thin black phosphorus films with varying thickness prepared by mechanical exfoliation on SiO_2/Si substrate. It has been found that the temperature dependence of the BP thin film is sensitive to the film thickness, showing a decreasing temperature coefficient with decreasing thickness. This behavior is attributed to the interaction of the film with substrate as well as the morphology distortion of the film. By studying a suspended film of 70 nm, an average thermal conductivity is estimated to be 15.8 W/mK for BP. Furthermore, substrates can significantly affect the heat dissipation of the BP film, which yields a much larger effective thermal conductivity 29.2 W/mK. This work indicates that substrate can significantly impact the properties of the BP film, and the extent depends on the specific material property of interest for a given thickness.

CHAPTER 7: CONCLUSIONS

At a first glance, all the 2D materials exhibit very different properties in comparison to their bulk forms, and they are promising candidates for a variety of applications, such as ultra-thin flexible devices. However, for most applications if not all, these 2D materials are required to be supported by substrates. Since their thicknesses are of atomic dimension, their properties are extremely sensitive to the substrates. For example, the PL of supported WS_2 monolayer quenches drastically comparing to that of suspended one, which is attributed to the charge transfer between the film and the substrate. Besides, the films are susceptible to have the morphologic variation laterally, resulting in the non-uniform film morphology, i.e. the difference in their optical and electric properties from spot to spot. Practically, there are two popular ways to fabricate 2D materials, which are mechanical exfoliation with scotch tape and chemical vapor deposition. For the transferred films, the polymeric residues from the production processes are typically attached to the films, which in most cases degrades the performance of the films. Even though annealing is used to remove the residues, there are still residual hydrocarbons left behind that can significantly change the properties of the films.

The primary theme of this dissertation is to understand the vibrational properties of these 2D materials and how the interaction of the 2D materials with their supporting substrates. In order to investigate these properties, Raman and PL spectroscopies at and above room temperature are applied to the 2D films. Four layered materials, graphene, MoS_2, WS_2 and black phosphorus, were studied with temperature-dependent Raman spectroscopy. With the temperature dependence of their major Raman modes, we were able to look into the vibrational properties of these 2D ma-

terials, and further to examine their temperature effect on the morphology of the films supported by different substrates. Furthermore, temperature-dependent PL spectroscopy reveals the change of band gap with temperature as well the intensity quench due to the doping effect and/or defects in the 2D materials.

(A) Graphene

The main focus of graphene is to investigate how the polymeric residues affects the vibrational properties of D, G and $2D$ vibrational bands of graphene in a temperature range from RT to $400\,°C$. We have found that the annealing of graphene could not remove the polymeric residues but leave behind hydrocarbons on the top of graphene. The Raman spectrum of graphene after annealing exhibited a broadening of both D and G bands, whose features are very similar to those of amorphous carbon. The amorphous carbon originated from those polymeric residues at elevated temperature. Additionally, the nonlinear temperature dependence observed in both ME and CVD-grown graphene samples indicates the possible slippage of graphene relative to the substrate as well as the change of the film morphology.

(B) MoS_2

MoS_2 samples prepared by both CVD and ME on different substrates were investigated with temperature-dependent Raman spectroscopy. The main observations of Raman response of these samples at elevated temperature were that the temperature coefficients of in-plane E_{2g}^1 mode for CVD-grown monolayer MoS_2 were smaller than ME samples, while the out-of-plane A_{1g} mode showed stronger nonlinearity of its temperature dependence. With respect to the difference between the two sample fabrication techniques, the CVD-grown MoS_2 are bound to the substrates stronger than ME or transferred ones, while the ME or transferred MoS_2 has non-planar morphology due to the interaction with the substrate. Therefore, the E_{2g}^1 mode of monolayer MoS_2 is more sensitive to the chemical bonding with the substrate while A_{1g} mode the film morphology. Furthermore, transferred monolayer MoS_2 on SiO_2/Si was an-

nealed up to 300 °C twice to study the annealing effect on the change of vibrational properties. The results showed that the temperature dependence of A_{1g} mode in the second-cycle annealing was more linear than that of first-cycle, while that of E_{2g}^1 mode in both cycles was quite linear. The reason of this change was due to the morphologic change of the film. The Raman and PL mapping results of the film revealed that the film became more planar and uniform. This further confirmed that A_{1g} mode was sensitive to the morphology of the film.

(C) WS$_2$

The crystalline structure of WS$_2$ is the same as that of MoS$_2$; thus, the temperature dependence of WS$_2$ is quite similar. The Raman and PL mapping on CVD-grown monolayer WS$_2$ triangles revealed that the strain distribution over the triangle is not uniform, as well as the doping/defect concentration. Using DFT calculated deformation potentials, the maximum difference of strain over a single triangle was estimated to be ∼0.5%. With the temperature-dependent Raman measurements of CVD-grown monolayer WS$_2$ samples and transferred CVD monolayers, temperature dependence similar to MoS$_2$ was observed. Though both modes showed nonlinear temperature dependences, the dependence of E_{2g}^1 mode was more linear. However, the main discover for WS$_2$ samples was the strain effect originating from the difference in TEC between the film and the substrate. The TEC of WS$_2$ is higher than those of substrates, both sapphire and SiO$_2$; thus, the WS$_2$ monolayer undergoes tensile strain after fast cooling down during the growth process. The tensile strain causes the redshifts of Raman frequencies of both modes. In the temperature-dependent Raman measurements, the tensile strain was released gradually, leading to the nonlinear temperature dependence of both modes. As the CVD-grown monolayer WS$_2$ was transferred to SiO$_2$/Si substrate, the non-planar morphology gave rise to the nonlinear temperature dependence of A_{1g} mode, which was similar to MoS$_2$. Moreover, temperature-dependent PL spectroscopy revealed the thermal quenching processes of CVD-grown monolayer

WS$_2$ on SiO$_2$/Si and sapphire substrates, and the activation energies were estimated to be 0.40 eV for the SiO$_2$ sample, and 0.20 eV and 1.51 eV for the sapphire sample.

(D) Black phosphorus

Black phosphorus has the unique anisotropic nature due to its puckered honeycomb structure, which was revealed by the angle-resolved Raman spectroscopy. Based on the angle-resolved Raman measurements, the crystalline orientation of BP thin films could be determined. The temperature dependent Raman spectroscopy of BP films with different thicknesses exhibited that the temperature dependence was sensitive to film thickness, showing a decreasing trend in temperature coefficient with decreasing thickness, which was attributed to the interaction of the film with substrate as well as the morphology distortion of the film. Furthermore, the average thermal conductivity of BP with a thickness of ~70 nm was extracted from the results of both laser power and temperature dependent Raman spectroscopy, which was 15.8 W/mK. Whereas, the effective thermal conductivity of BP supported by the SiO$_2$/Si substrate was calculated to be 29.2 W/mK, indicating that ther substrate could significantly impact the properties of BP films.

In general, the work highlighted in this dissertation not only characterizes the vibrational and optical properties of four 2D materials at elevated temperatures, but also emphasizes the importance of understanding the correlation of the properties of 2D materials with strain, film morphology and doping, which are all related to the substrate. Most previous studies were focusing on the electrical and optical properties of 2D materials themselves, the interaction with substrates were seldom investigated. In this dissertation, I have shown that the substrate effect can significantly affect the properties of 2D materials in different ways. For instance, the strain originated from the interaction between the film and the substrate changes the band structure which will further affect their performance in optoelectronic applications. Therefore, this work suggests the importance to fully understand the influence of the supporting

substrates to the 2D materials before they can be effectively used as devices, and the discoveries of this dissertation has laid the foundation for further investigation into the substrate effect on 2D materials.

REFERENCES

[1] R. P. Feynman, "There's plenty of room at the bottom," *Engineering and science*, vol. 23, no. 5, pp. 22–36, 1960.

[2] G. K. Bennig, "Atomic force microscope and method for imaging surfaces with atomic resolution," 1988. US Patent 4,724,318.

[3] E. Ruska, "Die elektronenmikroskopische abbildung elektronenbestrahlter oberflächen," *Zeitschrift für Physik*, vol. 83, no. 7-8, pp. 492–497, 1933.

[4] M. Von Ardenne and D. Beischer, "Untersuchung von metalloxyd-rauchen mit dem universal-elektronenmikroskop," *Zeitschrift für Elektrochemie und angewandte physikalische Chemie*, vol. 46, no. 4, pp. 270–277, 1940.

[5] H. W. Kroto, J. R. Heath, S. C. O'Brien, R. F. Curl, and R. E. Smalley, "C60: Buckminsterfullerene," *Nature*, vol. 318, no. 6042, pp. 162–163, 1985.

[6] C. G. Smith, "Low-dimensional quantum devices," *Reports on Progress in Physics*, vol. 59, no. 2, p. 235, 1996.

[7] L. Esaki and R. Tsu, "Superlattice and negative differential conductivity in semiconductors," *IBM Journal of Research and Development*, vol. 14, no. 1, pp. 61–65, 1970.

[8] J. S. Koehler, "Attempt to design a strong solid," *Physical Review B*, vol. 2, no. 2, pp. 547–551, 1970.

[9] P. R. Wallace, "The band theory of graphite," *Physical Review*, vol. 71, no. 9, pp. 622–634, 1947.

[10] K. S. Novoselov, A. K. Geim, S. V. Morozov, D. Jiang, Y. Zhang, S. V. Dubonos, I. V. Grigorieva, and A. A. Firsov, "Electric field effect in atomically thin carbon films," *Science*, vol. 306, no. 5696, pp. 666–669, 2004.

[11] K. S. Novoselov, A. K. Geim, S. V. Morozov, D. Jiang, M. I. Katsnelson, I. V. Grigorieva, S. V. Dubonos, and A. A. Firsov, "Two-dimensional gas of massless dirac fermions in graphene," *Nature*, vol. 438, no. 7065, pp. 197–200, 2005.

[12] R. Arenal, O. Stephan, M. Kociak, D. Taverna, A. Loiseau, and C. Colliex, "Electron energy loss spectroscopy measurement of the optical gaps on individual boron nitride single-walled and multiwalled nanotubes," *Physical Review Letters*, vol. 95, no. 12, p. 127601, 2005.

[13] L. Ci, L. Song, C. Jin, D. Jariwala, D. Wu, Y. Li, A. Srivastava, Z. F. Wang, K. Storr, L. Balicas, F. Liu, and P. M. Ajayan, "Atomic layers of hybridized boron nitride and graphene domains," *Nat Mater*, vol. 9, no. 5, pp. 430–435, 2010.

[14] H. S. S. Ramakrishna Matte, A. Gomathi, A. K. Manna, D. J. Late, R. Datta, S. K. Pati, and C. Rao, "MoS$_2$ and WS$_2$ analogues of graphene," *Angewandte Chemie*, vol. 122, no. 24, pp. 4153–4156, 2010.

[15] K. F. Mak, C. Lee, J. Hone, J. Shan, and T. F. Heinz, "Atomically thin MoS$_2$: A new direct-gap semiconductor," *Physical Review Letters*, vol. 105, no. 13, p. 136805, 2010.

[16] M. Chhowalla, H. S. Shin, G. Eda, L.-J. Li, K. P. Loh, and H. Zhang, "The chemistry of two-dimensional layered transition metal dichalcogenide nanosheets," *Nat Chem*, vol. 5, no. 4, pp. 263–275, 2013.

[17] H. Liu, A. T. Neal, Z. Zhu, Z. Luo, X. Xu, D. Tomanek, and P. D. Ye, "Phosphorene: An unexplored 2D semiconductor with a high hole mobility," *ACS Nano*, vol. 8, no. 4, pp. 4033–4041, 2014.

[18] L. Li, Y. Yu, G. J. Ye, Q. Ge, X. Ou, H. Wu, D. Feng, X. H. Chen, and Y. Zhang, "Black phosphorus field-effect transistors," *Nat Nano*, vol. 9, no. 5, pp. 372–377, 2014.

[19] A. H. Castro Neto, F. Guinea, N. M. R. Peres, K. S. Novoselov, and A. K. Geim, "The electronic properties of graphene," *Reviews of Modern Physics*, vol. 81, no. 1, pp. 109–162, 2009.

[20] F. Molitor, J. Guttinger, C. Stampfer, S. Drscher, A. Jacobsen, T. Ihn, and K. Ensslin, "Electronic properties of graphene nanostructures," *Journal of Physics: Condensed Matter*, vol. 23, no. 24, p. 243201, 2011.

[21] P. Sutter, M. S. Hybertsen, J. T. Sadowski, and E. Sutter, "Electronic structure of few-layer epitaxial graphene on Ru(0001)," *Nano Letters*, vol. 9, no. 7, pp. 2654–2660, 2009.

[22] D. Yoon, Y.-W. Son, and H. Cheong, "Negative thermal expansion coefficient of graphene measured by Raman spectroscopy," *Nano Letters*, vol. 11, no. 8, pp. 3227–3231, 2011.

[23] V. P. Gusynin and S. G. Sharapov, "Unconventional integer quantum hall effect in graphene," *Physical Review Letters*, vol. 95, no. 14, p. 146801, 2005.

[24] K. I. Bolotin, K. J. Sikes, Z. Jiang, M. Klima, G. Fudenberg, J. Hone, P. Kim, and H. L. Stormer, "Ultrahigh electron mobility in suspended graphene," *Solid State Communications*, vol. 146, no. 9, pp. 351–355, 2008.

[25] E. McCann, K. Kechedzhi, V. I. Fal'ko, H. Suzuura, T. Ando, and B. L. Altshuler, "Weak-localization magnetoresistance and valley symmetry in graphene," *Physical Review Letters*, vol. 97, no. 14, p. 146805, 2006.

[26] Y.-W. Son, M. L. Cohen, and S. G. Louie, "Energy gaps in graphene nanoribbons," *Phys. Rev. Lett.*, vol. 97, p. 216803, 2006.

[27] G. Giovannetti, P. A. Khomyakov, G. Brocks, P. J. Kelly, and J. van den Brink, "Substrate-induced band gap in graphene on hexagonal boron nitride: *Ab initio* density functional calculations," *Phys. Rev. B*, vol. 76, p. 073103, 2007.

[28] Y. Zhang, T.-T. Tang, C. Girit, Z. Hao, M. C. Martin, A. Zettl, M. F. Crommie, Y. R. Shen, and F. Wang, "Direct observation of a widely tunable bandgap in bilayer graphene," *Nature*, vol. 459, no. 7248, pp. 820–823, 2009.

[29] W. Choi, I. Lahiri, R. Seelaboyina, and Y. S. Kang, "Synthesis of graphene and its applications: A review," *Critical Reviews in Solid State and Materials Sciences*, vol. 35, no. 1, pp. 52–71, 2010.

[30] K. S. Novoselov, V. Fal, L. Colombo, P. Gellert, M. Schwab, K. Kim, *et al.*, "A roadmap for graphene," *Nature*, vol. 490, no. 7419, pp. 192–200, 2012.

[31] Y. Kubota, K. Watanabe, O. Tsuda, and T. Taniguchi, "Deep ultraviolet light-emitting hexagonal boron nitride synthesized at atmospheric pressure," *Science*, vol. 317, no. 5840, pp. 932–934, 2007.

[32] B. Radisavljevic, A. Radenovic, J. Brivio, V. Giacometti, and A. Kis, "Single-layer MoS_2 transistors," *Nature Nanotechnology*, vol. 6, no. 3, pp. 147–150, 2011.

[33] S. Jo, N. Ubrig, H. Berger, A. B. Kuzmenko, and A. F. Morpurgo, "Mono- and bilayer WS_2 light-emitting transistors," *Nano Letters*, vol. 14, no. 4, pp. 2019–2025, 2014.

[34] S. Das, H.-Y. Chen, A. V. Penumatcha, and J. Appenzeller, "High performance multilayer MoS_2 transistors with scandium contacts," *Nano letters*, vol. 13, no. 1, pp. 100–105, 2012.

[35] B. Chamlagain, Q. Li, N. J. Ghimire, H.-J. Chuang, M. M. Perera, H. Tu, Y. Xu, M. Pan, D. Xaio, J. Yan, *et al.*, "Mobility improvement and temperature dependence in $MoSe_2$ field-effect transistors on parylene-c substrate," *ACS nano*, vol. 8, no. 5, pp. 5079–5088, 2014.

[36] H.-J. Chuang, X. Tan, N. J. Ghimire, M. M. Perera, B. Chamlagain, M. M.-C. Cheng, J. Yan, D. Mandrus, D. Tománek, and Z. Zhou, "High mobility WSe_2 p-and n-type field-effect transistors contacted by highly doped graphene for low-resistance contacts," *Nano letters*, vol. 14, no. 6, pp. 3594–3601, 2014.

[37] R. Ganatra and Q. Zhang, "Few-layer MoS_2: A promising layered semiconductor," *ACS Nano*, vol. 8, no. 5, pp. 4074–4099, 2014.

[38] B. Schonfeld, J. J. Huang, and S. C. Moss, "Anisotropic mean-square displacements (MSD) in single-crystals of 2H- and 3R-MoS_2," *Acta Crystallographica Section B*, vol. 39, no. 4, pp. 404–407, 1983.

[39] H. Zeng, J. Dai, W. Yao, D. Xiao, and X. Cui, "Valley polarization in MoS$_2$ monolayers by optical pumping," *Nature Nanotechnology*, vol. 7, no. 8, pp. 490–493, 2012.

[40] G. Eda, H. Yamaguchi, D. Voiry, T. Fujita, M. Chen, and M. Chhowalla, "Photoluminescence from chemically exfoliated MoS$_2$," *Nano Letters*, vol. 11, no. 12, pp. 5111–5116, 2011.

[41] J. K. Ellis, M. J. Lucero, and G. E. Scuseria, "The indirect to direct band gap transition in multilayered MoS$_2$ as predicted by screened hybrid density functional theory," *Applied Physics Letters*, vol. 99, no. 26, p. 261908, 2011.

[42] A. Kuc, N. Zibouche, and T. Heine, "Influence of quantum confinement on the electronic structure of the transition metal sulfide TS$_2$," *Phys. Rev. B*, vol. 83, p. 245213, 2011.

[43] E. S. Kadantsev and P. Hawrylak, "Electronic structure of a single MoS$_2$ monolayer," *Solid State Communications*, vol. 152, no. 10, pp. 909–913, 2012.

[44] A. Splendiani, L. Sun, Y. Zhang, T. Li, J. Kim, C.-Y. Chim, G. Galli, and F. Wang, "Emerging photoluminescence in monolayer MoS$_2$," *Nano Letters*, vol. 10, no. 4, pp. 1271–1275, 2010.

[45] O. Lopez-Sanchez, D. Lembke, M. Kayci, A. Radenovic, and A. Kis, "Ultrasensitive photodetectors based on monolayer MoS$_2$," *Nat Nano*, vol. 8, no. 7, pp. 497–501, 2013.

[46] A. Molina-Sánchez and L. Wirtz, "Phonons in single-layer and few-layer MoS$_2$ and WS$_2$," *Phys. Rev. B*, vol. 84, p. 155413, 2011.

[47] Z. Y. Zhu, Y. C. Cheng, and U. Schwingenschlögl, "Giant spin-orbit-induced spin splitting in two-dimensional transition-metal dichalcogenide semiconductors," *Physical Review B*, vol. 84, no. 15, p. 153402, 2011.

[48] R. Coehoorn, C. Haas, J. Dijkstra, C. J. F. Flipse, R. A. de Groot, and A. Wold, "Electronic structure of MoSe$_2$, MoS$_2$, and WSe$_2$. i. band-structure calculations and photoelectron spectroscopy," *Physical Review B*, vol. 35, no. 12, pp. 6195–6202, 1987.

[49] R. Coehoorn, C. Haas, and R. A. de Groot, "Electronic structure of mose$_2$, mos$_2$, and wse$_2$. ii. the nature of the optical band gaps," *Physical Review B*, vol. 35, no. 12, pp. 6203–6206, 1987.

[50] C. Cong, J. Shang, X. Wu, B. Cao, N. Peimyoo, C. Qiu, L. Sun, and T. Yu, "Synthesis and optical properties of large-area single-crystalline 2D semiconductor WS$_2$ monolayer from chemical vapor deposition," *Advanced Optical Materials*, vol. 2, no. 2, pp. 131–136, 2014.

[51] S. Bertolazzi, J. Brivio, and A. Kis, "Stretching and breaking of ultrathin MoS$_2$," *ACS Nano*, vol. 5, no. 12, pp. 9703–9709, 2011.

[52] J.-U. Lee, D. Yoon, and H. Cheong, "Estimation of young's modulus of graphene by Raman spectroscopy," *Nano Letters*, vol. 12, no. 9, pp. 4444–4448, 2012.

[53] L. Leitao, S. Bala Kumar, O. Yijian, and J. Guo, "Performance limits of monolayer transition metal dichalcogenide transistors," *Electron Devices, IEEE Transactions on*, vol. 58, no. 9, pp. 3042–3047, 2011.

[54] D. Ovchinnikov, A. Allain, Y. S. Huang, D. Dumcenco, and A. Kis, "Electrical transport properties of single-layer WS$_2$," *ACS Nano*, vol. 8, no. 8, pp. 8174–81, 2014.

[55] J. Wu, N. Mao, L. Xie, H. Xu, and J. Zhang, "Identifying the crystalline orientation of black phosphorus using angle-resolved polarized Raman spectroscopy," *Angewandte Chemie International Edition*, vol. 54, no. 8, pp. 2366–2369, 2015.

[56] S. Zhang, J. Yang, R. Xu, F. Wang, W. Li, M. Ghufran, Y.-W. Zhang, Z. Yu, G. Zhang, Q. Qin, and Y. Lu, "Extraordinary photoluminescence and strong temperature/angle-dependent Raman responses in few-layer phosphorene," *ACS Nano*, vol. 8, no. 9, pp. 9590–9596, 2014.

[57] M. Buscema, D. J. Groenendijk, S. I. Blanter, G. A. Steele, H. S. van der Zant, and A. Castellanos-Gomez, "Fast and broadband photoresponse of few-layer black phosphorus field-effect transistors," *Nano Lett*, vol. 14, no. 6, pp. 3347–52, 2014.

[58] Y. Deng, Z. Luo, N. J. Conrad, H. Liu, Y. Gong, S. Najmaei, P. M. Ajayan, J. Lou, X. Xu, and P. D. Ye, "Black phosphorus-monolayer MoS$_2$ van der waals heterojunction p-n diode," *ACS Nano*, vol. 8, no. 8, pp. 8292–8299, 2014.

[59] M. Buscema, D. J. Groenendijk, G. A. Steele, H. S. van der Zant, and A. Castellanos-Gomez, "Photovoltaic effect in few-layer black phosphorus pn junctions defined by local electrostatic gating," *Nature Communications*, vol. 5, 2014.

[60] T. Hong, B. Chamlagain, W. Lin, H.-J. Chuang, M. Pan, Z. Zhou, and Y.-Q. Xu, "Polarized photocurrent response in black phosphorus field-effect transistors," *Nanoscale*, vol. 6, no. 15, pp. 8978–8983, 2014.

[61] C.-G. Andres, V. Leonardo, P. Elsa, O. I. Joshua, K. L. Narasimha-Acharya, I. B. Sofya, J. G. Dirk, B. Michele, A. S. Gary, J. V. Alvarez, W. Z. Henny, J. J. Palacios, and S. J. v. d. Z. Herre, "Isolation and characterization of few-layer black phosphorus," *2D Materials*, vol. 1, no. 2, p. 025001, 2014.

[62] M. Razeghi, *Fundamentals of Solid State Engineering*. Kluwer Academic Publishers, 2002.

[63] T. Steiner, *Semiconductor Nanostructures for Optoelectronic Applications*. Artech House, 2004.

[64] H. Hiura, T. W. Ebbesen, J. Fujita, K. Tanigaki, and T. Takada, "Role of sp^3 defect structures in graphite and carbon nanotubes," *Nature*, vol. 367, no. 6459, pp. 148–151, 1994.

[65] T. W. Ebbesen and H. Hiura, "Graphene in 3-dimensions: Towards graphite origami," *Advanced Materials*, vol. 7, no. 6, pp. 582–586, 1995.

[66] H. V. Roy, C. Kallinger, and K. Sattler, "Study of single and multiple foldings of graphitic sheets," *Surface Science*, vol. 407, no. 1, pp. 1–6, 1998.

[67] L. Xuekun, Y. Minfeng, H. Hui, and S. R. Rodney, "Tailoring graphite with the goal of achieving single sheets," *Nanotechnology*, vol. 10, no. 3, p. 269, 1999.

[68] Y. Zhang, L. Zhang, and C. Zhou, "Review of chemical vapor deposition of graphene and related applications," *Accounts of Chemical Research*, vol. 46, no. 10, pp. 2329–2339, 2013.

[69] M. Yi and Z. Shen, "A review on mechanical exfoliation for the scalable production of graphene," *Journal of Materials Chemistry A*, vol. 3, no. 22, pp. 11700–11715, 2015.

[70] K.-K. Liu, W. Zhang, Y.-H. Lee, Y.-C. Lin, M.-T. Chang, C.-Y. Su, C.-S. Chang, H. Li, Y. Shi, H. Zhang, C.-S. Lai, and L.-J. Li, "Growth of large-area and highly crystalline MoS$_2$ thin layers on insulating substrates," *Nano Letters*, vol. 12, no. 3, pp. 1538–1544, 2012.

[71] Y. Zhan, Z. Liu, S. Najmaei, P. M. Ajayan, and J. Lou, "Large-area vapor-phase growth and characterization of MoS$_2$ atomic layers on a SiO$_2$ substrate," *Small*, vol. 8, no. 7, pp. 966–971, 2012.

[72] M. R. Laskar, L. Ma, S. Kannappan, P. Sung Park, S. Krishnamoorthy, D. N. Nath, W. Lu, Y. Wu, and S. Rajan, "Large area single crystal (0001) oriented MoS$_2$," *Applied Physics Letters*, vol. 102, no. 25, p. 252108, 2013.

[73] Y.-H. Lee, X.-Q. Zhang, W. Zhang, M.-T. Chang, C.-T. Lin, K.-D. Chang, Y.-C. Yu, J. T.-W. Wang, C.-S. Chang, L.-J. Li, and T.-W. Lin, "Synthesis of large-area MoS$_2$ atomic layers with chemical vapor deposition," *Advanced Materials*, vol. 24, no. 17, pp. 2320–2325, 2012.

[74] Y.-C. Lin, W. Zhang, J.-K. Huang, K.-K. Liu, Y.-H. Lee, C.-T. Liang, C.-W. Chu, and L.-J. Li, "Wafer-scale MoS$_2$ thin layers prepared by MoO$_3$ sulfurization," *Nanoscale*, vol. 4, no. 20, pp. 6637–6641, 2012.

[75] C. V. Raman and K. S. Krishnan, "A new type of secondary radiation," *Nature*, vol. 121, no. 3048, pp. 501–502, 1928.

[76] G. Landsberg and L. Mandelstam, "Über die lichtzerstreuung in kristallen," *Zeitschrift für Physik*, vol. 50, no. 11-12, pp. 769–780, 1928.

[77] C. Kittel, *Introduction to solid state physics*. Wiley, 1971.

[78] Y. Peter and M. Cardona, *Fundamentals of semiconductors: physics and materials properties*. Springer Science & Business Media, 2010.

[79] C. Postmus, J. R. Ferraro, and S. S. Mitra, "Pressure dependence of infrared eigenfrequencies of KCl and KBr," *Phys. Rev.*, vol. 174, pp. 983–987, 1968.

[80] J. Menéndez and M. Cardona, "Temperature dependence of the first-order Raman scattering by phonons in Si, Ge, and $\alpha-$Sn: Anharmonic effects," *Physical Review B*, vol. 29, no. 4, pp. 2051–2059, 1984.

[81] W. J. Borer, S. S. Mitra, and K. V. Namjoshi, "Line shape and temperature dependence of the first order Raman spectrum of diamond," *Solid State Communications*, vol. 9, no. 16, pp. 1377–1381, 1971.

[82] M. Balkanski, R. F. Wallis, and E. Haro, "Anharmonic effects in light scattering due to optical phonons in silicon," *Physical Review B*, vol. 28, no. 4, pp. 1928–1934, 1983.

[83] P. G. Klemens, "Anharmonic decay of optical phonons," *Physical Review*, vol. 148, no. 2, pp. 845–848, 1966.

[84] Y. Varshni, "Temperature dependence of the energy gap in semiconductors," *Physica*, vol. 34, no. 1, pp. 149–154, 1967.

[85] M. Sturge, E. Cohen, and K. Rodgers, "Thermal quenching processes in the low temperature photoluminescence of excitons bound to nitrogen pairs in gap," *Physical Review B*, vol. 15, no. 6, p. 3169, 1977.

[86] Y. Zhang, M. Sturge, K. Kash, B. Van der Gaag, A. Gozdz, L. Florez, and J. Harbison, "Temperature dependence of luminescence efficiency, exciton transfer, and exciton localization in $GaAs/Al_xGa_{1-x}$ as quantum wires and quantum dots," *Physical Review B*, vol. 51, no. 19, p. 13303, 1995.

[87] D. Bimberg, M. Sondergeld, and E. Grobe, "Thermal dissociation of excitons bounds to neutral acceptors in high-purity gaas," *Physical Review B*, vol. 4, no. 10, p. 3451, 1971.

[88] A. Nwaneshiudu, C. Kuschal, F. H. Sakamoto, R. R. Anderson, K. Schwarzenberger, and R. C. Young, "Introduction to confocal microscopy," *J Invest Dermatol*, vol. 132, no. 12, p. e3, 2012.

[89] M. Minsky, "Memoir on inventing the confocal scanning microscope," *Scanning*, vol. 10, no. 4, pp. 128–138, 1988.

[90] M. Minsky, "Microscopy apparatus," 1961. US Patent 3,013,467.

[91] K. S. Novoselov, D. Jiang, F. Schedin, T. J. Booth, V. V. Khotkevich, S. V. Morozov, and A. K. Geim, "Two-dimensional atomic crystals," *Proceedings of the National Academy of Sciences of the United States of America*, vol. 102, no. 30, pp. 10451–10453, 2005.

[92] A. C. Ferrari, J. C. Meyer, V. Scardaci, C. Casiraghi, M. Lazzeri, F. Mauri, S. Piscanec, D. Jiang, K. S. Novoselov, S. Roth, and A. K. Geim, "Raman spectrum of graphene and graphene layers," *Physical Review Letters*, vol. 97, no. 18, p. 187401, 2006.

[93] P. Tan, Y. Deng, and Q. Zhao, "Temperature-dependent Raman spectra and anomalous Raman phenomenon of highly oriented pyrolytic graphite," *Physical Review B*, vol. 58, no. 9, pp. 5435–5439, 1998.

[94] S. Reich and C. Thomsen, "Raman spectroscopy of graphite," *Philosophical Transactions of the Royal Society of London A: Mathematical, Physical and Engineering Sciences*, vol. 362, no. 1824, pp. 2271–2288, 2004.

[95] R. Kostić, M. Mirić, T. Radić, M. Radović, R. Gajić, and Z. Popović, "Optical characterization of graphene and highly oriented pyrolytic graphite," *Acta Physica Polonica A*, vol. 116, no. 4, pp. 718–721, 2009.

[96] A. Gupta, G. Chen, P. Joshi, S. Tadigadapa, and Eklund, "Raman scattering from high-frequency phonons in supported n-graphene layer films," *Nano Letters*, vol. 6, no. 12, pp. 2667–2673, 2006.

[97] C. Thomsen and S. Reich, "Double resonant Raman scattering in graphite," *Physical Review Letters*, vol. 85, no. 24, pp. 5214–5217, 2000.

[98] A. Eckmann, A. Felten, A. Mishchenko, L. Britnell, R. Krupke, K. S. Novoselov, and C. Casiraghi, "Probing the nature of defects in graphene by Raman spectroscopy," *Nano letters*, vol. 12, no. 8, pp. 3925–3930, 2012.

[99] D. M. Basko, "Theory of resonant multiphonon Raman scattering in graphene," *Physical Review B*, vol. 78, no. 12, p. 125418, 2008.

[100] P. Venezuela, M. Lazzeri, and F. Mauri, "Theory of double-resonant Raman spectra in graphene: Intensity and line shape of defect-induced and two-phonon bands," *Physical Review B*, vol. 84, no. 3, p. 035433, 2011.

[101] M. Bruna, A. K. Ott, M. Ijäs, D. Yoon, U. Sassi, and A. C. Ferrari, "Doping dependence of the Raman spectrum of defected graphene," *ACS Nano*, vol. 8, no. 7, pp. 7432–7441, 2014.

[102] Z. Cheng, Q. Zhou, C. Wang, Q. Li, C. Wang, and Y. Fang, "Toward intrinsic graphene surfaces: A systematic study on thermal annealing and wet-chemical treatment of SiO_2-supported graphene devices," *Nano Letters*, vol. 11, no. 2, pp. 767–771, 2011.

[103] I. Calizo, A. A. Balandin, W. Bao, F. Miao, and C. N. Lau, "Temperature dependence of the Raman spectra of graphene and graphene multilayers," *Nano Letters*, vol. 7, no. 9, pp. 2645–2649, 2007.

[104] Z. Haiqing, Q. Caiyu, Y. Fang, Y. Huaichao, C. Minjiang, H. Lijun, G. Yanjun, and S. Lianfeng, "Raman scattering of monolayer graphene: the temperature and oxygen doping effects," *Journal of Physics D: Applied Physics*, vol. 44, no. 18, p. 185404, 2011.

[105] M. Huang, H. Yan, T. F. Heinz, and J. Hone, "Probing strain-induced electronic structure change in graphene by Raman spectroscopy," *Nano Letters*, vol. 10, no. 10, pp. 4074–4079, 2010.

[106] Y. Yu, C. Li, Y. Liu, L. Su, Y. Zhang, and L. Cao, "Controlled scalable synthesis of uniform, high-quality monolayer and few-layer MoS_2 films," *Scientific reports*, vol. 3, 2013.

[107] X. Zhang, W. P. Han, J. B. Wu, S. Milana, Y. Lu, Q. Q. Li, A. C. Ferrari, and P. H. Tan, "Raman spectroscopy of shear and layer breathing modes in multilayer MoS_2," *Phys. Rev. B*, vol. 87, p. 115413, 2013.

[108] M. Ghorbani-Asl, N. Zibouche, M. Wahiduzzaman, A. F. Oliveira, A. Kuc, and T. Heine, "Electromechanics in MoS_2 and WS_2: nanotubes vs. monolayers," *Scientific Reports*, vol. 3, 2013.

[109] H. Li, Q. Zhang, C. C. R. Yap, B. K. Tay, T. H. T. Edwin, A. Olivier, and D. Baillargeat, "From bulk to monolayer MoS_2: Evolution of Raman scattering," *Advanced Functional Materials*, vol. 22, no. 7, pp. 1385–1390, 2012.

[110] C. Lee, H. Yan, L. E. Brus, T. F. Heinz, J. Hone, and S. Ryu, "Anomalous lattice vibrations of single- and few-layer MoS_2," *ACS Nano*, vol. 4, no. 5, pp. 2695–2700, 2010.

[111] A. Bagnall, W. Liang, E. Marseglia, and B. Welber, "Raman studies of MoS_2 at high pressure," *Physica B+C*, vol. 99, no. 1, pp. 343–346, 1980.

[112] T. Li and G. Galli, "Electronic properties of MoS_2 nanoparticles," *The Journal of Physical Chemistry C*, vol. 111, no. 44, pp. 16192–16196, 2007.

[113] T. Cao, G. Wang, W. Han, H. Ye, C. Zhu, J. Shi, Q. Niu, P. Tan, E. Wang, B. Liu, *et al.*, "Valley-selective circular dichroism of monolayer molybdenum disulphide," *Nature communications*, vol. 3, p. 887, 2012.

[114] N. Scheuschner, O. Ochedowski, A.-M. Kaulitz, R. Gillen, M. Schleberger, and J. Maultzsch, "Photoluminescence of freestanding single- and few-layer MoS_2," *Phys. Rev. B*, vol. 89, p. 125406, 2014.

[115] K. F. Mak, K. He, C. Lee, G. H. Lee, J. Hone, T. F. Heinz, and J. Shan, "Tightly bound trions in monolayer MoS$_2$," *Nature Materials*, vol. 12, no. 3, pp. 207–211, 2013.

[116] N. Mounet and N. Marzari, "First-principles determination of the structural, vibrational and thermodynamic properties of diamond, graphite, and derivatives," *Phys. Rev. B*, vol. 71, p. 205214, 2005.

[117] T. Livneh and E. Sterer, "Resonant Raman scattering at exciton states tuned by pressure and temperature in 2H-MoS$_2$," *Phys. Rev. B*, vol. 81, p. 195209, 2010.

[118] S. Najmaei, P. M. Ajayan, and J. Lou, "Quantitative analysis of the temperature dependency in Raman active vibrational modes of molybdenum disulfide atomic layers," *Nanoscale*, vol. 5, no. 20, pp. 9758–9763, 2013.

[119] S. Sahoo, A. P. Gaur, M. Ahmadi, M. J.-F. Guinel, and R. S. Katiyar, "Temperature-dependent Raman studies and thermal conductivity of few-layer MoS$_2$," *The Journal of Physical Chemistry C*, vol. 117, no. 17, pp. 9042–9047, 2013.

[120] Z. H. Ni, H. M. Wang, Z. Q. Luo, Y. Y. Wang, T. Yu, Y. H. Wu, and Z. X. Shen, "The effect of vacuum annealing on graphene," *Journal of Raman Spectroscopy*, vol. 41, no. 5, pp. 479–483, 2010.

[121] S. Sugai and T. Ueda, "High-pressure Raman spectroscopy in the layered materials 2H-MoS$_2$, 2H-MoSe$_2$, and 2H-MoTe$_2$," *Physical Review B*, vol. 26, no. 12, p. 6554, 1982.

[122] S. H. El-Mahalawy and B. L. Evans, "The thermal expansion of 2H-MoS$_2$, 2H-MoSe$_2$ and 2H-WSe$_2$ between 20 and 800 °C," *Journal of Applied Crystallography*, vol. 9, no. 5, pp. 403–406, 1976.

[123] B. Chakraborty, A. Bera, D. Muthu, S. Bhowmick, U. V. Waghmare, and A. Sood, "Symmetry-dependent phonon renormalization in monolayer MoS$_2$ transistor," *Physical Review B*, vol. 85, no. 16, p. 161403, 2012.

[124] W. Zhou, X. Zou, S. Najmaei, Z. Liu, Y. Shi, J. Kong, J. Lou, P. M. Ajayan, B. I. Yakobson, and J.-C. Idrobo, "Intrinsic structural defects in monolayer molybdenum disulfide," *Nano letters*, vol. 13, no. 6, pp. 2615–2622, 2013.

[125] A. Gurarslan, Y. Yu, L. Su, Y. Yu, F. Suarez, S. Yao, Y. Zhu, M. Ozturk, Y. Zhang, and L. Cao, "Surface-energy-assisted perfect transfer of centimeter-scale monolayer and few-layer MoS$_2$ films onto arbitrary substrates," *ACS nano*, vol. 8, no. 11, pp. 11522–11528, 2014.

[126] J. Feng, X. Qian, C.-W. Huang, and J. Li, "Strain-engineered artificial atom as a broad-spectrum solar energy funnel," *Nature Photonics*, vol. 6, no. 12, pp. 866–872, 2012.

[127] A. Berkdemir, H. R. Gutiérrez, A. R. Botello-Méndez, N. Perea-López, A. L. Elías, C.-I. Chia, B. Wang, V. H. Crespi, F. López-Urías, J.-C. Charlier, *et al.*, "Identification of individual and few layers of WS$_2$ using Raman spectroscopy," *Scientific Reports*, vol. 3, 2013.

[128] H. R. Gutiérrez, N. Perea-López, A. L. Elías, A. Berkdemir, B. Wang, R. Lv, F. López-Urías, V. H. Crespi, H. Terrones, and M. Terrones, "Extraordinary room-temperature photoluminescence in triangular WS$_2$ monolayers," *Nano letters*, vol. 13, no. 8, pp. 3447–3454, 2012.

[129] C. Ballif, M. Regula, P. Schmid, M. Remškar, R. Sanjines, and F. Levy, "Preparation and characterization of highly oriented, photoconducting WS$_2$ thin films," *Applied Physics A*, vol. 62, no. 6, pp. 543–546, 1996.

[130] X. Ling, L. Moura, M. A. Pimenta, and J. Zhang, "Charge-transfer mechanism in graphene-enhanced Raman scattering," *The Journal of Physical Chemistry C*, vol. 116, no. 47, pp. 25112–25118, 2012.

[131] D. J. Late, "Temperature dependent phonon shifts in single-layer WS$_2$," *ACS applied materials & interfaces*, vol. 6, no. 2, pp. 1158–1163, 2014.

[132] S. D. Namgung, S. Yang, K. Park, A.-J. Cho, H. Kim, and J.-Y. Kwon, "Influence of post-annealing on the off current of MoS$_2$ field-effect transistors," *Nanoscale research letters*, vol. 10, no. 1, pp. 1–6, 2015.

[133] F. Withers, T. H. Bointon, D. C. Hudson, M. F. Craciun, and S. Russo, "Electron transport of WS$_2$ transistors in a hexagonal boron nitride dielectric environment," *Scientific reports*, vol. 4, 2014.

[134] L. Su, Y. Zhang, Y. Yu, and L. Cao, "Dependence of coupling of quasi 2-D MoS$_2$ with substrates on substrate types, probed by temperature dependent Raman scattering," *Nanoscale*, vol. 6, no. 9, pp. 4920–4927, 2014.

[135] L. Su, Y. Yu, L. Cao, and Y. Zhang, "Effects of substrate type and material-substrate bonding on high-temperature behavior of monolayer WS$_2$," *Nano Research*, vol. 8, no. 8, pp. 2686–2697, 2015.

[136] N. Peimyoo, W. Yang, J. Shang, X. Shen, Y. Wang, and T. Yu, "Chemically driven tunable light emission of charged and neutral excitons in monolayer WS$_2$," *ACS nano*, vol. 8, no. 11, pp. 11320–11329, 2014.

[137] Y. Wang, C. Cong, W. Yang, J. Shang, N. Peimyoo, Y. Chen, J. Kang, J. Wang, W. Huang, and T. Yu, "Strain-induced direct–indirect bandgap transition and phonon modulation in monolayer WS$_2$," *Nano Research*, pp. 1–11, 2015.

[138] J. Kang, S. Tongay, J. Zhou, J. Li, and J. Wu, "Band offsets and heterostructures of two-dimensional semiconductors," *Applied Physics Letters*, vol. 102, no. 1, p. 012111, 2013.

[139] S. Najmaei, Z. Liu, W. Zhou, X. Zou, G. Shi, S. Lei, B. I. Yakobson, J.-C. Idrobo, P. M. Ajayan, and J. Lou, "Vapour phase growth and grain boundary structure of molybdenum disulphide atomic layers," *Nature materials*, vol. 12, no. 8, pp. 754–759, 2013.

[140] A. L. Elías, N. Perea-López, A. Castro-Beltrán, A. Berkdemir, R. Lv, S. Feng, A. D. Long, T. Hayashi, Y. A. Kim, M. Endo, *et al.*, "Controlled synthesis and transfer of large-area WS_2 sheets: From single layer to few layers," *ACS nano*, vol. 7, no. 6, pp. 5235–5242, 2013.

[141] J.-w. Wei, Z.-w. Ma, H. Zeng, Z.-y. Wang, Q. Wei, and P. Peng, "Electronic and optical properties of vacancy-doped WS_2 monolayers," *AIP Advances*, vol. 2, no. 4, p. 042141, 2012.

[142] F. Allen and G. Gobeli, "Work function, photoelectric threshold, and surface states of atomically clean silicon," *Physical Review*, vol. 127, no. 1, p. 150, 1962.

[143] Y. Guo, X. Wei, J. Shu, B. Liu, J. Yin, C. Guan, Y. Han, S. Gao, and Q. Chen, "Charge trapping at the MoS_2-SiO_2 interface and its effects on the characteristics of MoS_2 metal-oxide-semiconductor field effect transistors," *Applied Physics Letters*, vol. 106, no. 10, p. 103109, 2015.

[144] S. Sugai, T. Ueda, and K. Murase, "Pressure dependence of the lattice vibration in the orthorhombic and rhombohedral structures of black phosphorus," *Journal of the Physical Society of Japan*, vol. 50, no. 10, pp. 3356–3361, 1981.

[145] C. Casiraghi, A. Hartschuh, E. Lidorikis, H. Qian, H. Harutyunyan, T. Gokus, K. Novoselov, and A. Ferrari, "Rayleigh imaging of graphene and graphene layers," *Nano letters*, vol. 7, no. 9, pp. 2711–2717, 2007.

[146] S.-L. Li, H. Miyazaki, H. Song, H. Kuramochi, S. Nakaharai, and K. Tsukagoshi, "Quantitative Raman spectrum and reliable thickness identification for atomic layers on insulating substrates," *ACS nano*, vol. 6, no. 8, pp. 7381–7388, 2012.

[147] M. Buscema, G. A. Steele, H. S. van der Zant, and A. Castellanos-Gomez, "The effect of the substrate on the Raman and photoluminescence emission of single-layer MoS_2," *Nano Research*, vol. 7, no. 4, pp. 561–571, 2014.

[148] X. Liu, J. D. Wood, K.-S. Chen, E. Cho, and M. C. Hersam, "In situ thermal decomposition of exfoliated two-dimensional black phosphorus," *The Journal of Physical Chemistry Letters*, vol. 6, no. 5, pp. 773–778, 2015.

[149] A. A. Balandin, S. Ghosh, W. Bao, I. Calizo, D. Teweldebrhan, F. Miao, and C. N. Lau, "Superior thermal conductivity of single-layer graphene," *Nano letters*, vol. 8, no. 3, pp. 902–907, 2008.

[150] N. Peimyoo, J. Shang, W. Yang, Y. Wang, C. Cong, and T. Yu, "Thermal conductivity determination of suspended mono-and bilayer WS_2 by Raman spectroscopy," *Nano Research*, vol. 8, no. 4, pp. 1210–1221, 2014.

[151] Z. Luo, J. Maassen, Y. Deng, Y. Du, M. S. Lundstrom, P. D. Ye, and X. Xu, "Anisotropic in-plane thermal conductivity observed in few-layer black phosphorus," *arXiv preprint arXiv:1503.06167*, 2015.

[152] H. Asahina and A. Morita, "Band structure and optical properties of black phosphorus," *Journal of Physics C: Solid State Physics*, vol. 17, no. 11, p. 1839, 1984.

[153] H. Schafft, J. S. Suehle, P. G. Mirel, *et al.*, "Thermal conductivity measurements of thin-film silicon dioxide," in *Microelectronic Test Structures, 1989. ICMTS 1989. Proceedings of the 1989 International Conference on*, pp. 121–125, IEEE, 1989.

[154] E. Lemmon and R. Jacobsen, "Viscosity and thermal conductivity equations for nitrogen, oxygen, argon, and air," *International journal of thermophysics*, vol. 25, no. 1, pp. 21–69, 2004.